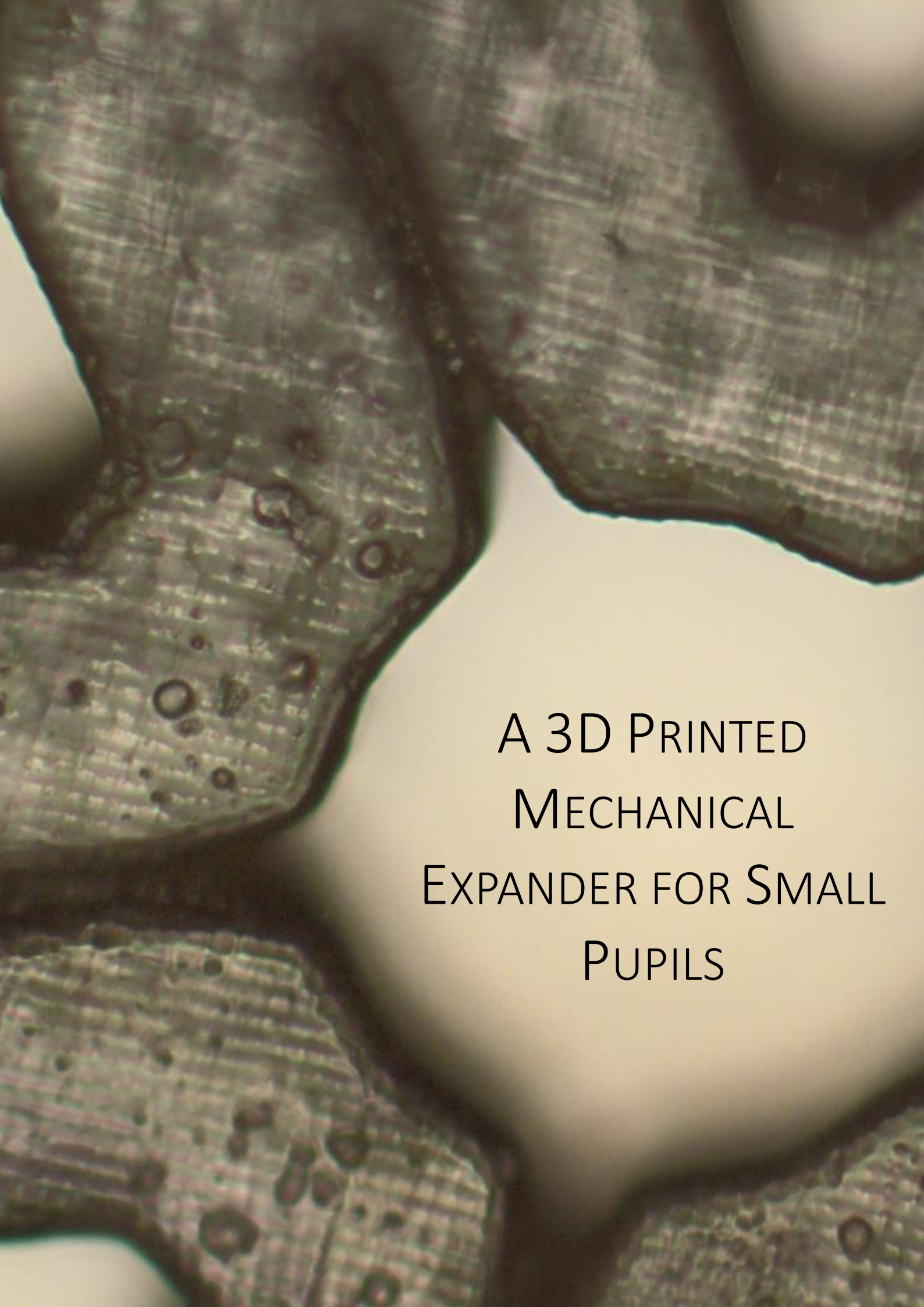

A 3D Printed Mechanical Expander for Small Pupils

A 3D Printed Mechanical Expander for Small Pupils

by

Oualid Zoumhani

in partial fulfillment of the requirements for the degree of

Master of Science in Biomedical Engineering

August 31st, 2022

Supervisor	Dr. C. Boutry	TU Delft
Thesis committee	Prof. dr. J. Dankelman	TU Delft
	Prof. dr. P.M. Sarro	TU Delft
	Dr. C. Boutry	TU Delft

TU Delft Delft University of Technology

Acknowledgments

First and foremost, I would like to express my deepest gratitude to my supervisor Dr. Clémentine Boutry for allowing me the opportunity to work on this wonderful project. Her vast knowledge, experience, admirable work ethic, and emphatic personality were an inspiration throughout the past nine months.

The EKL staff is thanked for their continuous work in keeping the laboratories running and their concern for our safety. In particular, I would like to thank Dr. Hitham Amin Hassan for allowing us to introduce new chemicals into the cleanroom and for providing insights on specific chemistry-related topics. I am also thankful to Filip Simjanoski for ordering the chemicals used throughout this project.

I am extremely grateful to Luutzen Wymega, who introduced me to the Materials lab at the Industrial design faculty, where he patiently provided instructions on the DMA test bench. I would be remiss in not mentioning Dr. Bjorn de Wagenaar for providing his expertise on 3D printing and for always asking the most beneficial questions. Special thanks to Dr. Reece Lewis, who aided with the GPC measurements and allowed the “exotic polymers”, as he called them, to be tested at the Applied Sciences faculty.

I had the pleasure of collaborating, on specific elements of the project, with my fellow student Zhengwei Liao who provided a sense of companionship throughout the thesis and with whom I was able to have profound conversations. I wish him all the luck in the world in his future endeavors.

Finally, I am forever indebted to my family, particularly my parents, to whom I owe any and every achievement in this life. Their support and words of encouragement are and will forever be invaluable.

Abstract

Cataract surgery is one of the most widely performed procedures in the world, preventing dramatic vision loss in millions of people. The condition of small pupils, which is the inability to dilate the iris by pharmacological means before cataract surgery, affects up to 11% of patients. It requires mechanical retractors currently made of hard materials, which often cause irreversibly damage to iris tissue. This thesis used Digital Light Processing (DLP) 3D printing to develop a new generation of soft pupil expansion devices. DLP is an additive manufacturing technique that allows for high fabrication throughput and precision to enable fast and accurate scaffolds and devices. In this project, poly (glycerol sebacate) acrylate (PGSA) was synthesized, and PGSA ink was developed for DLP printing with an Asiga Max X 3D printer. This material was selected for its suitable mechanical properties regarding flexibility and elasticity, and its established biocompatibility. Its biodegradable property made it also interesting in the context of a future single-use medical device. DLP 3D printing allowed for fast and precise fabrication of different prototypes of pupil expansion rings made of soft elastomeric materials and controlled with fluidic or magnetic actuation. Inks with different densities, viscosities, and polymerization kinetics were developed to investigate the achievability of a new generation of soft actuation pupil expansion devices to mitigate adverse patient outcomes of current commercially available devices. PGSA biodegradable soft elastomers were characterized mechanically and chemically. In addition, for the first time, carbonyl iron powder (CIP) was mixed with PGSA to achieve an elastomer composite material compatible with DLP 3D printing. Feature sizes below 100 µm, outperforming the requirements for the present application, were achieved in a reproducible manner. Fluidic and magnetic actuation were demonstrated with prototypes made of PGSA and CIP-PGSA composites, respectively.

List of Figures

List of Tables

Contents

1 Introduction

Over the last couple of decades, engineers have shown increasing interest in soft robotics, for which soft polymers are often used as a compliant material. In contrast, conventional robotics is a field in which rigid systems are used to perform an exact movement. Nature, however, is void of such organisms. Although vertebrates have an essentially rigid frame, they show remarkable resilience to large deformations because of the soft tissue surrounding this rigid structure. Moreover, while Ismael al Jazari is considered the father of robotics based on his principles for biology-inspired engineering, soft robotics has progressed tremendously since then. With soft robotics, the advantage of predictable movements is lost, and new challenges arise in soft actuation and sensing. This holds even more true when these soft robots have to operate on a small scale. As a biomedical engineer, the main focus is to advance technology in the world of medicine to improve human wellbeing. By this definition, tackling the most prevalent issues in the world of human health is the best way of fulfilling this task. There are several ways of retrieving which field it would be that indeed benefits the most from this technology. When looking at it from the perspective of most interventions performed worldwide, Cesarean sections, cataract surgery, biopsies, and appendectomy are mentioned.[1] Looking further into these surgeries, not all would directly benefit from the advancements in softer approaches, but cataract surgeries could benefit greatly. Cataract surgery is one of, if not the most, performed surgeries worldwide. [2,3] Although complications are not frequent, the sheer number of surgeries reveals a complication many patients suffer from, small pupils. Considering the capabilities of soft actuation methods and studies showing room for improvement for patients with this condition, a newly developed pupil expansion device should be considered.

Cataracts are the leading cause of blindness worldwide, afflicting almost 100 million people.[4] Phacoemulsification cataract surgery is currently the state-of-art for extracting cataractous lenses. During this surgery, it is crucial that the pupil stays sufficiently dilated. However, many patients suffer from small pupils, increasing intra- and post-operative complications. Pupil expansion devices provide mechanical dilation and can prove helpful in these cases. However, their use is associated with excessive deformation and tissue damage. Therefore, the aim is to work towards a softer pupil expander that uniformly expands to achieve controlled pupil dilation.

This thesis strives toward the design and fabrication of a mechanical pupil expansion device that features soft actuation utilizing fluidic or magnetic actuation. The intended material is PGSA, which will be 3D printed to fabricate the device. Since PGS and PGSA display an extensive range of material properties dependent on the synthesis parameters, the synthesis will be initiated from scratch for this particular application. To achieve a PGSA resin compatible with 3D printing, PGSA will have to be chemically modified. The final product will not only be able to compete with the current state-of-the-art concerning safety and visual equity post-surgery but also regarding cost-effectiveness and operative times owing to the chosen material and actuation methods. Findings, considerations, discussions, and inspirations from the literature review will be utilized fully during the process.

2 Literature Review

2.1 Phacoemulsification Cataract Surgery

2.1.1 The Crystalline Lens

Located posterior to the cornea and iris of the human eye is the inner lens, suspended by zonular fibers, fixing its position anteriorly of the vitreous humor.[5] The lens consists of a capsule, epithelium, cortex, and nucleus.[5,6] From that position, the lens has two functions: refracting any light that enters the eye and focusing it on the retina to create an image for the brain. The second is to provide accommodation for the incoming light by changing its morphology to maintain a focused image on the retina.[6–8] The cornea, the most anterior part of the eye, also acts as a lens that provides accommodation to distinguish between the two. The inner lens is often referred to as the inner, posterior, or crystalline lens. For the remainder of this work, the word lens refers to the crystalline lens.

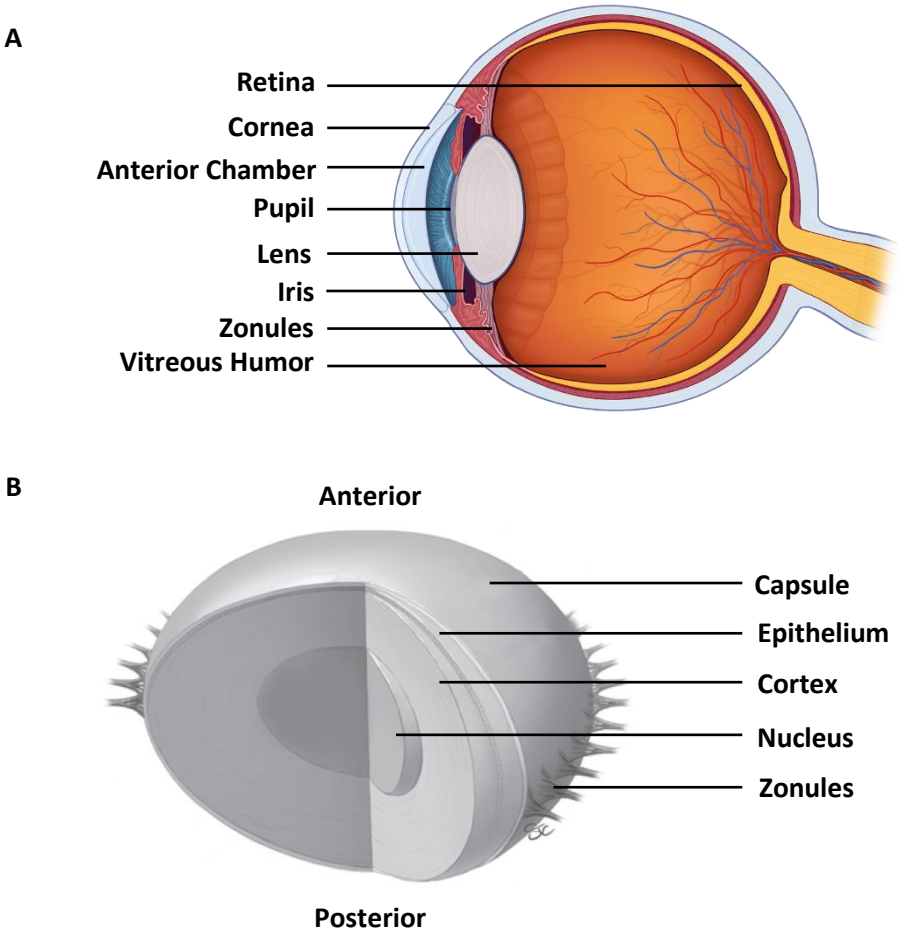

Figure 2.1 | Overview of relevant anatomical features of the eye. (**A**) Cross section of the eye highlighting relevant structures.[9] (**B**) The layered structure of the crystalline lens.[6]

The lens starts to develop in the 5th to 6th week of gestation. It stems from the ectoderm layer and is aneural, avascular, and alymphatic in the adult human body.[10] Moreover, the lens is a biconvex, transparent structure comprised of fibers produced in the lens epithelium that later move towards the nucleus in the center.[11,12] The epithelium is the most metabolically active part of the lens undergoing oxidation and crosslinking.[12] Because of the aforementioned migration of new lens fibers from the epithelium to the nucleus, the nucleus contains older lens fibers, and newly formed fibers are found in the lens cortex. These fiber cells contain very high concentrations of α, β, and γ-crystallin proteins allowing the lens to maintain its transparency and refractive index for the duration of a

lifetime.[8] This class of proteins falls under the category of Extremely Long-Lived Proteins (ELLP), unlike most other proteins in the human body that have considerably less long life spans. Other ELLPs are the proteins that provide structural support in the extracellular matrix, collagen, and elastin.[8] There are two classes of crystallin proteins, taxon-specific and ubiquitous crystallins. α, β, and γ-crystallins belong to the latter, while taxon-specific crystallins are found in certain animal species such as reptiles and birds.[10] Because crystallins are synthesized in the fiber cells of the lens, and due to the fact that these fiber cells lose their organelles and eventually also their nucleus, there is no possibility for renewal. Fiber cells lose their organelles because of extreme elongation during the early stages of development, but the unique ELLP characteristics are achieved because of this.[8] However, new fiber cells will always be supplied from the epithelium, meaning that the lens has concentric layers of lens fibers with varying crystallin concentrations.[13] The concentration of crystallins in the cortex is approximately 15% and increases with each adjacent layer moving to the center to about 70%.[14]

2.1.2 Cataracts

Light must pass through several structures of the eye and reach the retina unobstructed for the human brain to create a sharp image (see fig. 2.2). However, due to oxidative stress, the lens crystallins can be altered, causing protein aggregation, which can lead to cataracts.[8] These oxidative stresses are caused by an imbalance of anti-and pro-oxidants, causing abnormal metabolism, disease, and loss of physiological function, in this case, that of the eye.[15] The aggregation of proteins causes an increase in the refractive index of the lens that in turn leads to opaqueness of the lens. This opacification or clouding of the lens is the prime cause of cataracts and is mainly related to aging. As of 2020, cataracts remain the leading cause of blindness in the world, with around 94 million cases worldwide, according to the World Health Organization.[4]

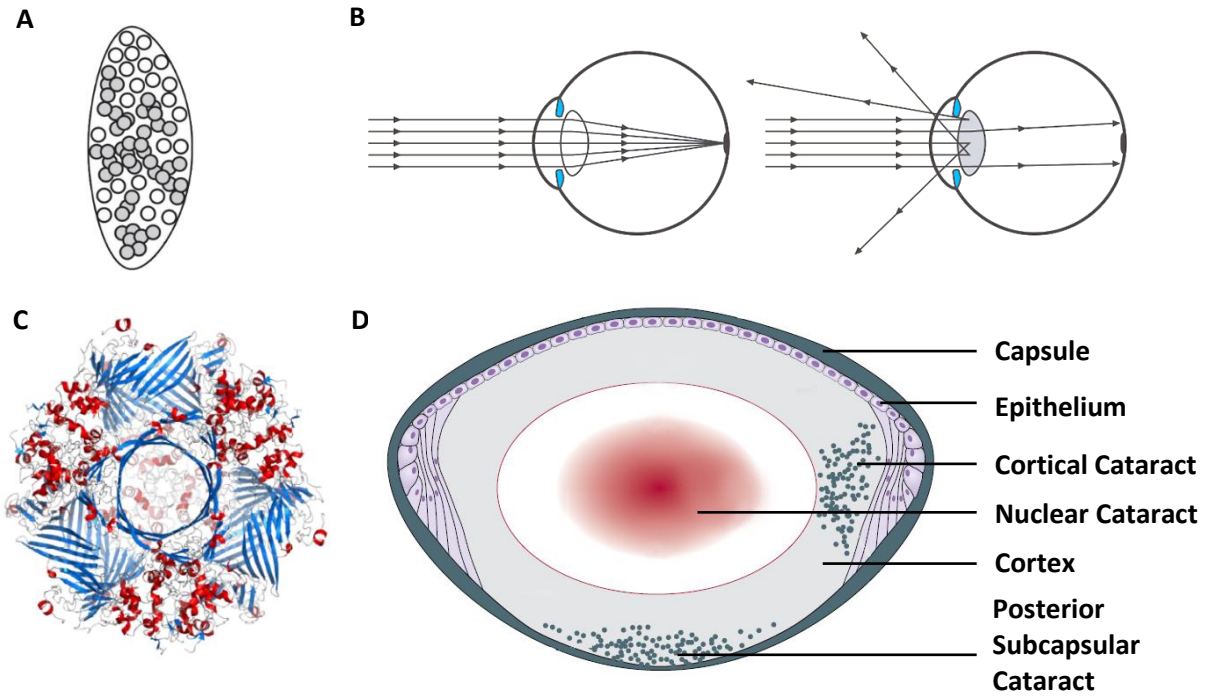

Figure 2.2 | Detailed overview of lens structures. (**A**) A crystalline lens with insoluble aggregates in grey.[8] (**B**) Two situations are displayed. On the left, incoming light rays pass through a clear lens and focus on the retina, providing clear sight. On the right, a cataracted lens obstructs incoming light rays, therefore preventing clear sight and creating a blurry image.[8] (**C**) Representative structures of the ubiquitous crystallin types in the human lens.[8] (**D**) Schematic overview of lens structures and their corresponding types of cataracts.[12]

There are two main types of cataracts. The first, and most prevalent type of cataract, is age-related cataracts, and the onset is between the ages of 45 and 50 and is more common in females. This type of cataract can be divided into three location-based sub-groups: nuclear, cortical, and posterior subcapsular cataracts (see fig. 2 D). The second is pediatric cataracts that are either congenital or develop during the early years of an infant. Cataracts can be hereditary, causing children to be afflicted from birth, but like adults, they can develop due to other factors. These other factors are exposure to ionizing, infrared or ultraviolet radiation, certain drugs and medications, and chemical or mechanical trauma to the eye.[12,16,17].

2.1.3 Cataract Surgery

Because the causes of aggregation of lens fiber are not something contemporary only, people have always suffered from its symptoms. Once cataractogenesis sets in, it is impossible to reverse its effects. Therapeutic treatment is preferred for improving visual capacity, and a better understanding of the molecular intricacies of the α, β, and γ-crystallins might hold the answer in the future.[1810] However, all solutions up till now remain surgical. Although its origins are not agreed upon, Sushruta Samhita is credited by most for performing the first cataract removal in approximately 800 B.C.[19,20] Two procedures are described in ancient literature, the first is couching, where a sharp-pointed needle is inserted perpendicular to the eye, behind the limbus. The surgeon manually dislodges the lens from the visual axis by breaking the zonules. Afterward, it remains inside of the vitreous humor. The second procedure is an early example of modern extracapsular cataract extraction (ECCE) described clearly in "Sushruta Samhita, Uttar Tantra." A similar procedure is followed. However, here the lens is extracted by having the patient perform Valsalva, which is forceful exhalation while closing both the mouth and the nostrils.[20] Both procedures are pretty disturbing and very painful. However, it did solve the issue temporarily.[21] Although vision is restored, with the inability to focus vision, lack of aseptic techniques caused blindness in most patients shortly after the procedure. [6] This ancient method is unfortunately still practiced today, mainly in African countries without anesthetics and with significant health risks.[21]

Extracapsular refers to the fact that during the procedure, the lens is removed while leaving the lens capsule in place. In 1747**,** Frenchman Jacques Daviel performed the first recorded modern extracapsular cataract extraction (ECCE).[6] This cataract surgery involved using curettage to extract the lens from the lens capsule through an incision of at least 10 mm in the cornea. This procedure also had complications but was the preferred solution for cataract removal until the early 20th century. Some complications were lens remnants inside the vitreous humor, infections, and, most importantly, posterior capsular opacification. Posterior capsular opacification stems from remaining lens epithelial cells where new lens fiber is synthesized. The remaining lens capsule then undergoes opacification by the exact pathophysiology described earlier.

Because of this phenomenon, intracapsular cataract extraction (ICCE) became the preferred procedure for removing cataracts. Intracapsular, in this case, refers to removing the lens, including the lens capsule, preventing secondary vision loss from posterior capsular opacification. This method was first used in 1753 by Samuel Sharp. It required a large incision and involved manually fracturing the zonules to remove the capsule in its entirety. Because new techniques and tools were developed in the early 1900s, intracapsular cataract extraction became more popular for a limited time. [19] ICCE had other disadvantageous effects on the patients. The main drawback of this method is the risk of the vitreous humor collapsing, causing retinal detachment because of the lack of support from the lens capsule.[6] The lens capsule functions as a supportive structure between the anterior and posterior chamber.[22]

Due to this glaring health risk, infections, and poor wound healing due to the large incision, by the 1970s, extracapsular cataract extraction became the standard once again. Surgical improvements such as topical anesthetics, intraocular lenses (1949), ophthalmic viscosurgical devices (OVD) (1972), and YAG (yttrium aluminum garnet) laser (1980) substantially improved the procedure.[6,17,23] Manual small incision cataract surgery (MSICS) is currently the standard for removing cataractous lenses in developing and underdeveloped countries.[23] It is more affordable, efficient, safe, accessible, and offers better refractive outcomes because of the intraocular lens (IOL).[24] MSICS requires a scleral incision of 6-7 mm, 2mm from the limbus, after which viscoexpression is used to detach the lens from the lens capsule to remove the lens, as a whole or in fragments, through the sclerocorneal tunnel.[12,23,25] During this procedure, the anterior chamber is filled with a viscoelastic substance to maintain a dome shape, allowing the surgeon to move the cataractous lens to the anterior chamber to proceed with lens delivery.[23,25] Through the same sclerocorneal tunnel, an IOL is implanted that attaches to the remaining lens capsule, allowing better refractive outcomes.[12] Should any posterior capsular opacification occur with the new IOL, YAG laser capsulotomy is provided, which is capable of removing any opacification entirely without requiring a second visit to the hospital.[19]

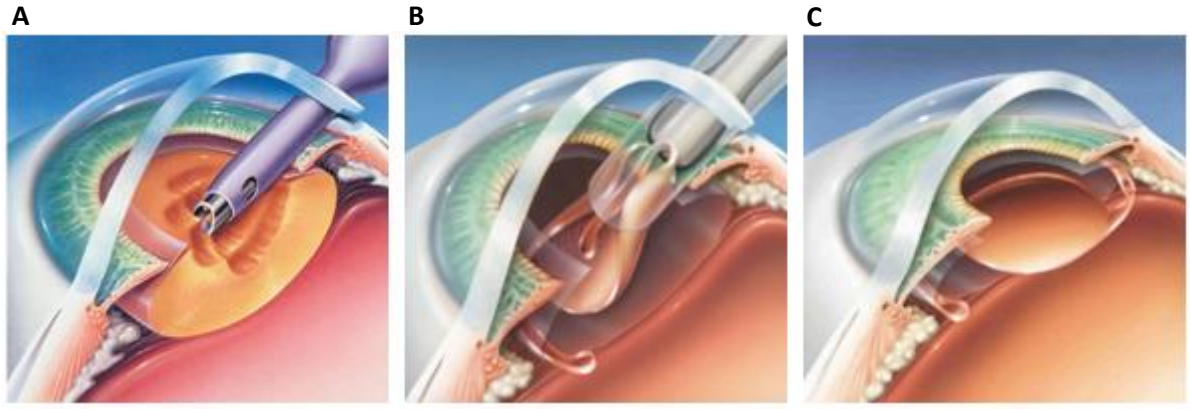

Figure 2.3 | Phacoemulsification cataract surgery procedure. (**A**) A phacoemulsification probe is inserted through the main cataract incision to break down crystalline lens tissue. (**B**) Through the same incision, an IOL is implanted into the lens capsule. (**C**) The new situation with the IOL haptics attached to the lens capsule.

The current state of the art in removing cataracts is phacoemulsification cataract surgery. Phacoemulsification was introduced in 1967 and allowed for an even smaller incision, leading to better patient recovery.[19,26] It is the safest and most preferred cataract extraction procedure in developing countries.[12] Before the surgery, the patient is given topical medications and anesthetics to achieve sufficient pupil dilation and locally numb the patient. Lateral to the sclera, a small incision is made directly into the anterior chamber to provide OVD. Then in a multiplanar fashion, the main incision is made through which capsulorhexis is performed to promote self-healing. Capsulorhexis is a circular opening that detaches in the anterior part of the lens capsule to detach the cataractous lens so it can be removed. A phacoemulsification probe is inserted through the main incision of about 1.8-3.2 mm to provide ultrasound waves to fragment the lens (see fig. 2.3 A).[6,12] Lens fragments are then aspirated through the same phacoemulsification probe. After removal, a new foldable IOL can be implanted through the same incision (see fig. 3 B). The IOL usually has two haptics to attach to the remaining lens capsular bag (see fig. 2.3 C). Femtosecond Laser-Assisted Cataract Surgery (FLACS) has been used since its FDA approval in 2010 in complex cases to increase precision and automate some of the steps, but due to high costs, it is not yet widely used. [12,26] Cataract surgery is considered the most performed and most successful surgical procedure in the world, with 20-30 million cases each year.[27–29]

2.1.4 Small Pupils

Topical medications are administered to achieve and maintain sufficient pupil dilation for cataract extraction, either by regular ECCE or phacoemulsification. A sufficiently dilated pupil is necessary for the surgery to take place. Some patients, however, cannot have their pupils achieve and maintain this state of mydriasis. Patients who suffer from this condition have a greater risk of intra- and post-operative complications.[30] These include incomplete cataract removal, suboptimal IOL placement, capsular damage, iris prolapse, pupillary sphincter dysfunction, cystoid macular edema, and retinal detachment.[16,29–32] Risk factors for small pupils include diabetes mellitus, Intraoperative Floppy Iris Syndrome (IFIS), Pseudoexfoliation syndrome (PXF), previous trauma or surgery of the eye, and uveitis (inflammation inside of the eye). [29,32,33] Tamsulosin, a drug described for benign prostatic hyperplasia, an enlargement of the prostate gland, is the most common cause of IFIS. Tamsulosin works as an α1-adrenergic antagonist. Therefore, muscles with α1 receptors tend to relax.[34] α1 receptors are found in the smooth muscle cells of the prostate and bladder muscles, thereby improving bladder emptying. However, these α1 receptors are also present in the iris dilator muscles, causing poor pupil dilation because of muscle atrophy and increasing the complication rate of patients with IFIS up to 12.5%.[16,33,35] PXF is the deposition of fibrous tissue from the lens onto structures in the anterior chamber of the eye, causing mechanical blocking of the iris when trying to dilute.[31,36] There is no clear indication of the number of patients suffering from this condition. However, most reported values range between 1-11% of all cataract extraction procedures.[37–39] There is also no consensus about what is considered to be a small pupil. Some literature suggests that a diameter smaller than 6 mm is small, but a more experienced surgeon may consider 4 mm the threshold.[16,32,33,37] Pupil size is regulated by the pupillary sphincter and dilator muscles of the iris and constricts in the case of light and viewing of a near object (see fig. 2.4).[40,41]

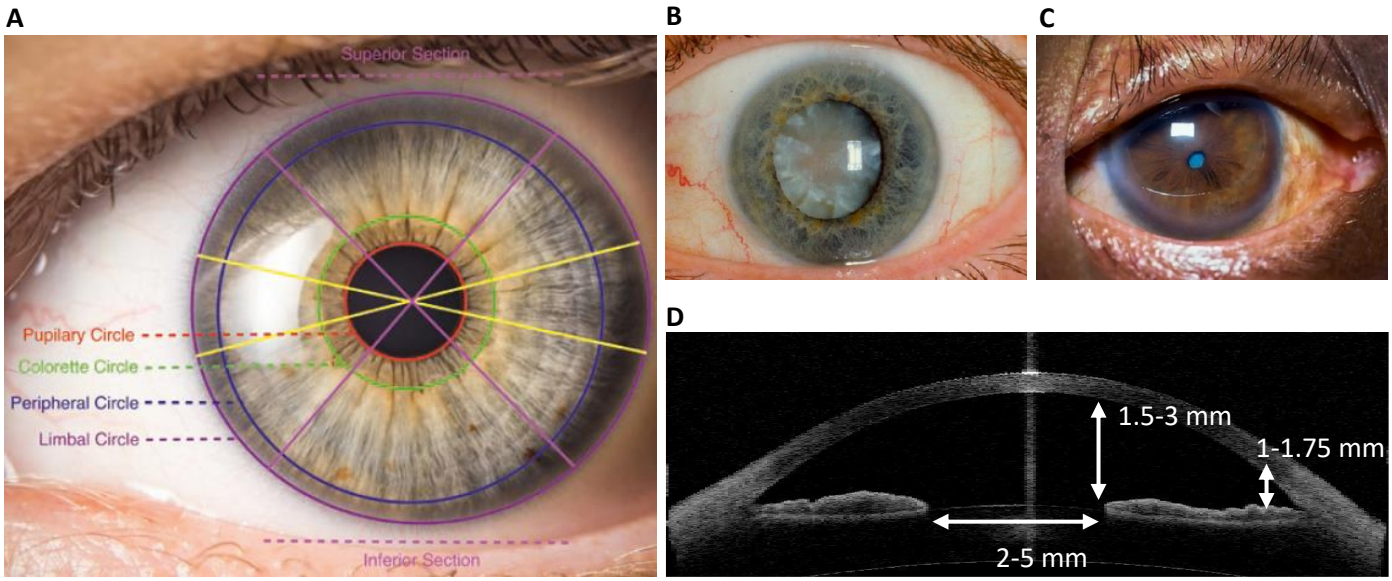

Figure 2.4 | Overview of the iris. (**A**) Iris demarcations show the border between different iris structures. The average total iris diameter varies between 12 and 13 mm. The thickness ranges from approximately 0.2 mm at the periphery and 0.8 at its thickest at the collarette. The average distance between the collarette and the pupil is 1.2 to 1.5 mm.[41] The sphincter muscle is located concentrically within the pupillary circle, while the dilator muscle is arranged radially and is confined between the pupillary and limbal circles.[40] (**B**) A hyper-mature nuclear cataract in a dilated pupil with active dilator muscles.[6] (**C**) A small cataracted pupil in an older person with active sphincter muscles.[42] (**D**) An optical coherence tomography scan of the anterior chamber of the eye displaying a range of iris diameters in case of small pupils prior to surgery.[43,44]

2.1.5 Managing Small Pupils

Small pupils are a common challenge for cataract surgeons. Surgeons have a stepwise approach when dealing with small pupils that focuses mainly on the wellbeing of the patient and successful surgery.[33] The surgeon starts by preoperatively administering mydriatic pharmacological agents and Nonsteroidal Anti Inflammatory Drugs (NSAIDs) to ensure pupillary dilation and prevent intraoperative miosis. Intracameral administration of pharmaceuticals has proven especially effective for achieving rapid mydriasis.[16,31] Irrigation fluids can potentially diminish the effects of the intracameral mydriatic drops. Therefore, fluid irrigation can be infused with NSAIDs to prevent pain post-surgery. To maintain anterior chamber pressure, fluid irrigation with OVD is necessary for modern phacoemulsification cataract surgery. Also, a high viscosity OVD could be used to further mydriasis.[31,45]

In some cases, adjustments in the method of application of the pharmaceutical are sufficient to prevent pupil miosis. However, other methods remain in the repertoire of the surgeon. Depending on the achieved mydriasis, mechanical stretching of the pupillary region of the iris tissue can be applied to reach the lens. It is recommended that the surgeon increases anesthesia since the aim of pupillary stretching is to create small sphincter tears (micro sphincterotomies) in the fibrotic iris tissue to dilate the pupil, potentially causing pain, iris bleeding, and pupil atony.[16,17,45]

If mydriasis is still insufficient, the surgeon may opt, as a last resort, to use pupil expansion devices. Among these devices are the iris hooks or iris retractors that require at least four additional 1 mm incisions on the cornea to introduce the hooks that latch on to the edge of the iris. Each hook has an adjustable sleeve that allows the surgeon to expand the pupil to the necessary size while trying to avoid damaging the pupillary margin of the iris.[16] Although it is challenging to avoid micro sphincterotomies, iris hooks paved the way for further innovation of pupil expansion devices.[33] Over the years, many pupil expansion devices were marketed, usually ring-shaped. Table 2.1 shows an overview of all commercially available devices and their main properties.

Malyugin ring	i-ring pupil expander	Graether 2000 pupil expander system	Canabrava ring	B-Hex pupil expander	Assia pupil expander
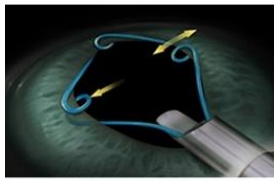	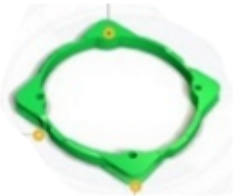			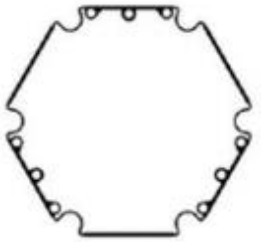	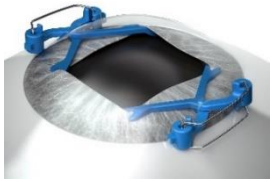
Polypropylene	Polyurethane	Silicone	PMMA*	Polyimide	Nylon
6.25- or 7-mm variation Trapezoidal	6.3 mm	6.3 mm	6.3 mm	5.5 mm	6 x 6 mm. Square opening
2 mm. Dedicated injector	No requirement stated	No requirement stated	2mm. McPherson forceps can be used.	0.9 mm. Dedicated b-hex forceps are required.	1.1 mm. Without injector. Requires two incisions.
2007/2016 (V1/V2)	2016	1992 (Original release)	2018	2014	2015

Name	Xpand NT iris	Oasis iris expander	Morcher pupil expander	Milvella Perfect pupil
			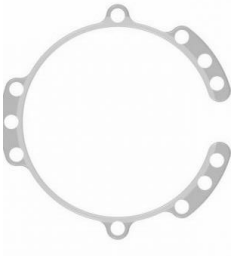	
Material	Titanium-Nickel Alloy	Polypropylene	PMMA*	Polyurethane
Provided diameter (mm)	6.7 mm	6.25- or 7-mm variation Square shaped	5-6 mm	7 mm
Required incision (mm)	2.5 mm	No requirement stated	2.5 mm with an injector. Manually or injector	No requirement stated injector or manual.
Introduction	2014	2016	2006	2005

Table 2.1 | Overview of commercially available pupil expansion devices.[29,46] *Poly (methyl methacrylate)

Studies regarding Intraoperative mechanical pupil expansion have been conducted to compare surgical outcomes achieved with different devices. In general, pupil expansion devices successfully achieve visual equity in patients with small pupils.[47,48] Iris hooks do not increase intraoperative complications compared to other pupil expansion devices. However, they cause a more significant increase in operating times.[48] Also, achieved visual acuity is equal for both the Malyugin ring and the iris hooks.[48] Using any pupil expansion technique intraoperatively caused an increase in pupil diameter post-surgery. However, this increase was most when using solely micro sphincterotomies

to achieve adequate pupil diameter.[47] Not only are pupil expansion devices better in this regard, but they also maintain better dilation than other manual iris stretching methods.[47] Some of the older pupil expansion devices such as the Graether pupil expander, Milvella perfect pupil, and Morcher pupil expander have been replaced by newer and more easy-to-use devices such as the I-ring, Malyugin ring, OASIS iris expander.[16,47] Compared with manual stretching and iris hooks, pupil expansion devices have a clear advantage regarding operative time and ease of surgery.[47,49] However, they are still associated with having a higher risk of inflammations and corneal edema rates.[48] There are also differences between the different pupil expansion devices themselves. The circular I-ring, for example, causes less pupil distortion than the diamond-shaped Malyugin ring.[50] Also, the Polyurethane I-ring is softer than the Polypropylene Malyugin ring, which may have also aided in minimizing pupil distortion post-surgery.

Numerical analysis regarding pupil expansion devices is limited. However, finite element modeling was used to estimate the stresses on the iris from three pupil expansion mechanisms. Iris hooks, the APX-dilator, and the Malyugin ring were modeled and compared with a hypothetical uniform radial expansion of the iris tissue (see fig. 2.5).[51] This uniform and circular expansion case is believed to be the optimal iris shape to limit damage to the iris. Compared with only the necessary force to expand the iris, all pupil expansion devices exerted significantly higher forces on the iris tissue (Table 2.2).[51] Only one paper describes the use of pupil expansion devices considering IFIS. IFIS was mathematically modeled, and computer simulations were able to determine that the Malyugin ring is able to prevent abnormal movements of the iris in such cases.[52]

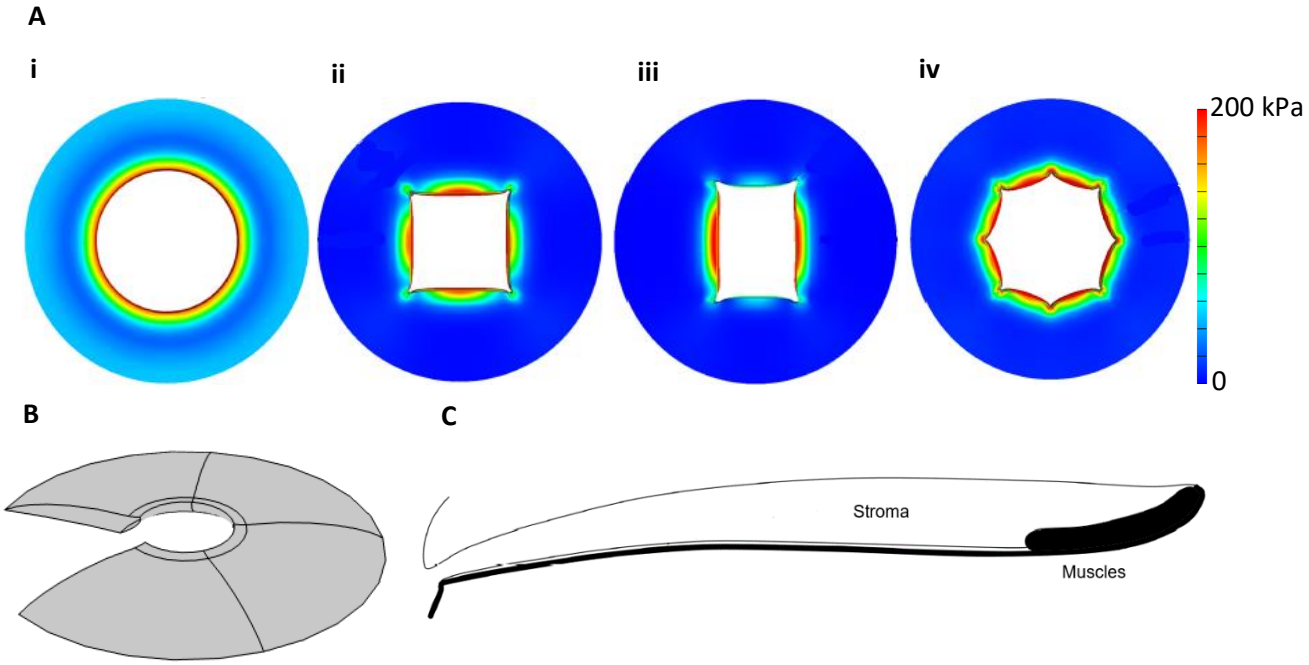

Figure 2.5 | Pupil expansion simulations using finite element analysis. (**A**) Different deformation patterns and the stresses applied on the iris. i, Uniform radial expansion. ii, Iris hooks. iii, APX Dilator iv, Malyugin ring.[51] (**B**) COMSOL model of the iris based on the work of Tan et al. (**C**) The iris was split into two separate bodies for this study. The stroma and anterior boundary (in white), and the muscles and posterior epithelium (in black).[51]

	Iris Hooks	APX Dilator	Malyugin Ring
Max Stroma Stress	+ 59%	+ 177%	+ 425%
Average Stroma Stress	+ 49%	+ 127%	+ 192%
Max Muscle Stress	+ 1283%	+ 1384%	+ 393%
Average Muscle Stress	+ 1207%	+ 1255%	+ 317%
Area of Pupil	- 43%	- 43,8%	- 24,9%

Table 2.2 | Applied forces on the iris relative to uniform radial expansion. Applied stresses from the different mechanical pupil expansion devices cause significant forces on the iris tissue, damaging it in the process. The iris hooks (+1207%) and APX dilator (+1255%) cause elevated stresses on the iris sphincter muscles since the force is focused on a small surface area. The Malyugin ring causes increased stress on the iris body (+192%) and muscles (+317%). The circular shape of the Malyugin ring distributes the forces over the entire surface area of the concentric sphincter muscle. Concurrently the available surface area of the pupil for all three devices is smaller compared to uniform expansion, with the Malyugin ring providing the largest available area of the three analyzed devices. (+ greater than, - smaller than).[51]

While small pupils remain a challenge for cataract surgery, different approaches are available to reduce the risk factors that come with it. When pharmacological treatment is insufficient, mechanical pupil expansion devices are considered to manage small pupils. However, the options available are still associated with exerting forces significantly higher than required, causing lasting deformation of the iris, inflammatory responses, and corneal edema. From the literature, it is clear that a softer approach has to be considered in the case of small pupils during the cataract extraction procedure. Therefore, a new mechanical pupil expansion device should be soft, biocompatible, minimally influencing operating times, and cost-effective. Additionally, the device should also be biodegradable. Should any remnants of the device be left inside of the patient, whether it is during implantation, use, or retrieval of the device, it should not cause the patient any harm while at the same time preventing rehospitalization.

2.2 Soft Actuation

2.2.1 Types of Soft Actuation

Although the current keyword “soft-robot” was introduced in 2008, publications featuring soft actuators date back to 1990 and have garnered widespread attention among researchers over the past decade.[53,54] However, this research is mainly exploratory in nature, and few real-life applications have been achieved compared to soft ones simply because they can be soft.[53] Here, the intended purpose is to utilize soft robotics to comply with the need for a pupil expansion device that safely maintains mydriasis, to improve cataract surgery outcomes. Soft robotics was defined in 2014 as the study of: “robots with…bioinspired capabilities that permit adaptive, flexible interactions with unpredictable environments.”[55] A soft mechanical pupil expander is inspired by the dilator muscles of the iris to interact with the unpredictable iris tissue safely. Since several types of soft actuation exist, the current state-of-the-art is reviewed to decide on the most suitable method for the intended purpose. This choice should be based on the following criteria found in table 2.3.

Criteria	Elaboration
Patient safety	Is the safety of the patient and the surgeon preserved?
Compliance	Does the actuation allow for fully compliant materials that adapt to the iris tissue?
Miniaturization	Is the actuation achievable on a micrometer scale inside the anterior chamber of the eye?
Controllability	To what extent is the actuation controlled by the surgeon?
Range of motion	Does the actuation allow for sufficient dilation of the pupil?
Force	Is mydriasis achieved with the appropriate force necessary?
Speed	Does actuation happen promptly without impairing the current operative times?
Material compatibility	What materials are used for actuation, and do they comply with the biocompatibility and degradability requirements?
Repeatability	Is it possible to perform the same movements consecutively?

Table 2.3 | Criteria for soft actuation. The selected criteria should be considered when choosing the most beneficial type of soft robotic actuation for mechanically expanding the pupil during cataract surgery.

The criteria listed in table 2.3 will be used to evaluate the soft actuation types found in the literature. Figure 2.6 lists the primary, often used types of soft robotic actuation in no particular order. The following chapter explains these actuation types to better understand their working principles.

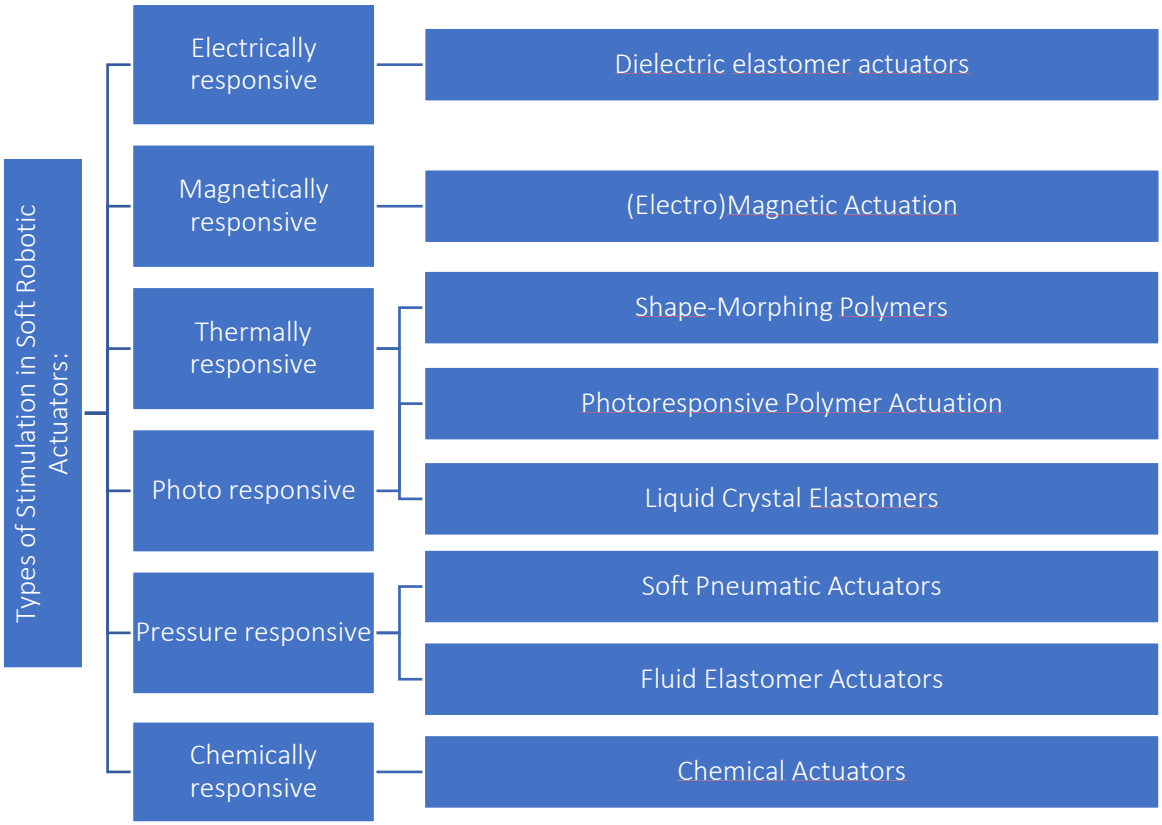

Figure 2.6 | Overview of soft robotic actuation types studied in recent literature.[56–59]

2.2.2 Electrically Responsive Actuation

Some materials can transform electrical energy into mechanical energy, enabling fast and simple movements.[56] Only dielectric elastomer actuation is covered in this review because of the increased voltages required for piezoelectric actuation.[56] Different elastomers, silicones, and polyurethanes have been researched as materials for dielectric actuators.[60] A dielectric membrane is sandwiched between two layers of compliant electrodes. [61] A voltage is provided to these electrodes, allowing the dielectric membrane to generate an electric field.[60] The created stresses cause the membrane to expand, converting the electric energy into locomotion.

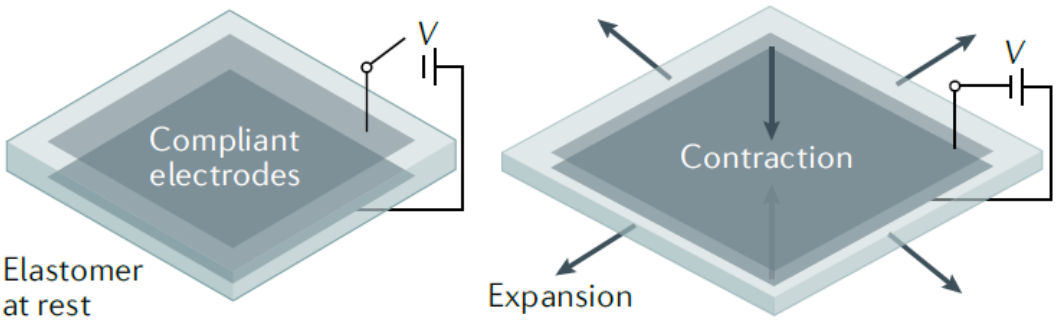

Figure 2.7 | Working principle of dielectric elastomer actuation.[62]

In the search for the most efficient compliant electrode, carbon-based metals are used, such as carbon grease and nanotubes.[60] However, these are not biodegradable. Examples of a fully biodegradable dielectric actuator were not found in the literature. Even though DEA allows for safer application compared to piezoelectric actuation, a high voltage, on the order of 10^3 V, is still necessary to achieve locomotion.[61] The generated current can be relatively small, on the order of 10^{-6} A, but lowering the current results in slower actuation speeds.[61,62] However, this still requires that the high voltage parts be insulated. While the speed of actuation might not be an immediate issue for using this type of soft actuation, the lack of examples of a fully biodegradable electrically stimulated actuator inherently makes it incompatible for the intended purpose. Other than that, depending on the applied current, DEA allows for sufficient speed and good accuracy of control and movement.[59,61,63]

2.2.3 Magnetically Responsive Actuation

Soft magnetic actuation is one of four types of tetherless locomotion in soft robotics.[64] Magnetic, light, acoustic and chemical stimuli are able to achieve mechanical micromanipulation without being in direct contact with any equipment apart from the device itself.[62,64] By controlling the magnitude and direction of a magnetic field, actuation is achieved quickly and accurately.[56] What makes it even more interesting is that magnetic actuation can occur as long as a medium can have magnetic particulates incorporated inside or on its surface.[56] Based on the alignment of the magnetic particles inside of the medium and the direction of the generated field, movements such as bending, elongation, contraction, and torsion can be achieved.[56,65] Complex motions such as multiple independent movements are possible when field and gradient are created independently. Achievable speeds of 100Hz have been reported making this type of actuation one of the fastest possible. [56,66] One main disadvantage is the bulky magnetic coils that generate the magnetic field. While they allow for application in enclosed areas, the surrounding setup is generally large and requires much power.[56] This being the main disadvantage, provides a near-optimal solution when choosing a suitable soft actuation type. In a modern hospital setting, the required power and space should not pose any issues.

A magnetic field can be generated through permanent magnets or electromagnets to actuate a magnetically responsive device from outside of the workspace.[67] Permanent magnets generate strong magnetic fields that depend on the size and shape of the magnet and can be approximated by a point-dipole model.[67] The magnetic field is nonuniform and decreases in strength with increasing distance between the dipole source and the object that is to be controlled.[67] The dipole moment is always perpendicular to the rotation axis.[68] To achieve an electromagnetic field, coils are used to generate nearly uniform magnetic fields that are current-dependent and very predictable.[67,68] These specialized coils are usually Helmholtz coils containing two coaxial circular coils that are separated by a distance equal to their radius and produce a field when equivalent currents pass through in the same direction.[67,68]

Polyethylene glycol (PEG) was used as an elastomeric matrix for 5 µm sized magnetic microparticles to fabricate a reconfigurable magnetic composite in the work of Song et al. (see fig. 2.8).[69] Static and rotatable ferromagnetic states were achieved by increasing and decreasing the temperature of the composite around the threshold of 58 °C. Being able to rotate the microparticles inside of the elastomer matrix is advantageous as it allows the same composite to respond differently to the same magnetic field. Origami structures were also fabricated that allowed for reconfigurable transformations with a continuous magnetization pattern.

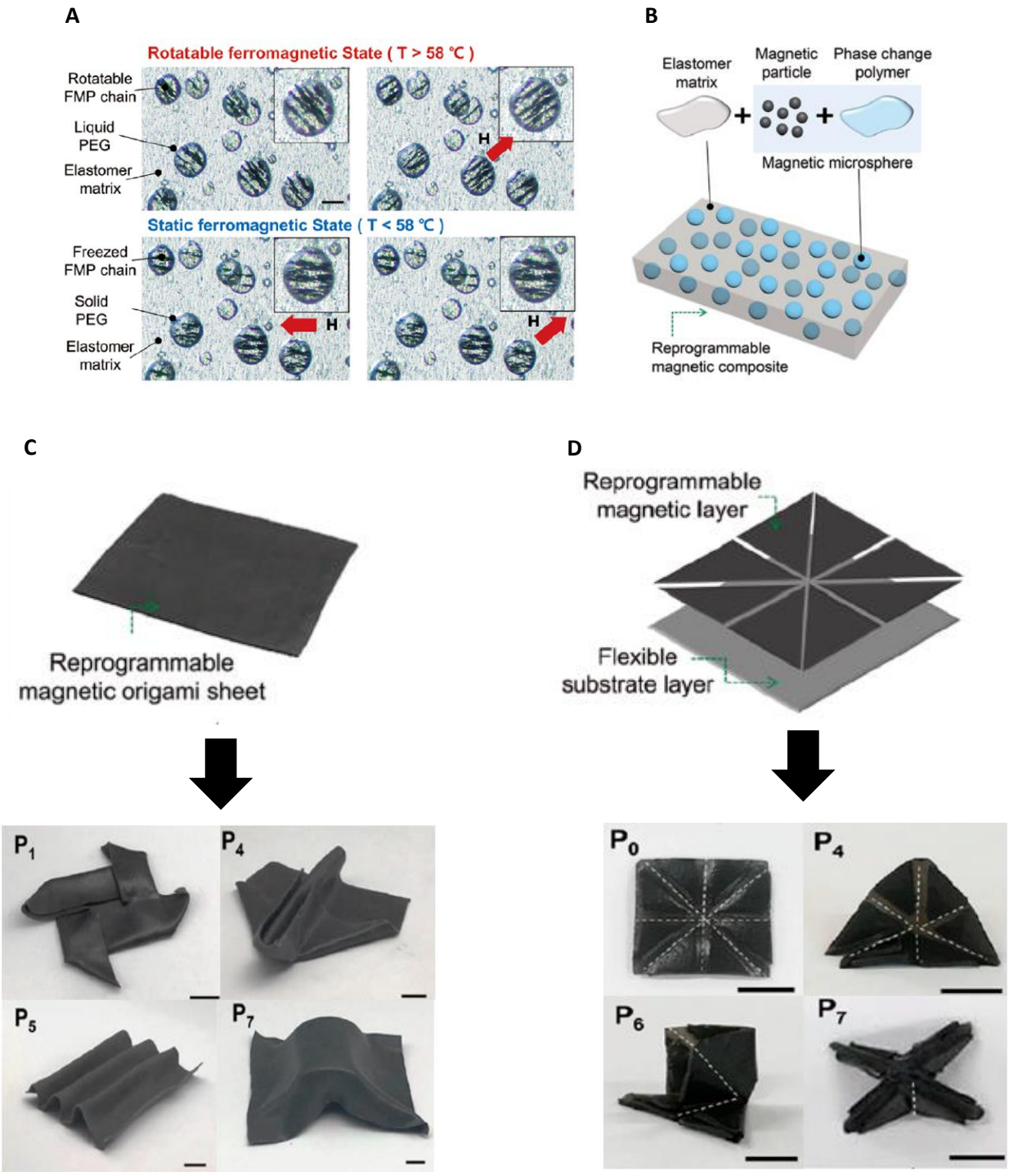

Figure 2.8 | Soft magnetic actuation achieved using permanent magnets. (**A**) Magnetization of the magnetic composite by creating a field when the microparticles are able to rotate at a temperature of approximately 67 °C. (**B**) Schematic overview of magnetic microspheres inside the elastomer matrix. (**C**) A continuous magnetic membrane is used as an origami sheet to transform into several shapes with a magnetic field of 100mT. (**D**) a similar programmable magnetic origami sheet with eight parts attached to a polyvinyl chloride substrate. The magnetic field is 100 mT and is perpendicular to the magnetic layer (scale bars are 10 mm).[69]

2.2.4 Thermally Responsive Actuation

Actuation is achieved by using stimuli such as heat and radiation to achieve locomotion in thermally responsive materials. [56]. While thermal-driven actuation provides a safe stimulation for biomedical applications, the main disadvantage is the slow rate and low efficiency compared to other actuation modes.[66] Various movements can be achieved and are reversible depending on the chemical properties of the soft material.[56,66] Not only can this type of actuation be completely wireless, but it also remains lightweight and fully compliant. Thermally driven actuation relies on the coefficient of thermal expansion of materials.[66] To achieve this actuation with soft materials, conductive materials are added to soft ones to create composites. Actuation can be based on Shape-Memory Materials (SMMs), Liquid-Crystal Elastomers (LCEs), and Shape Morphing Polymers (SMPs).[56,57,62,66]

Shape morphing polymer is a general term for soft, responsive materials that can achieve actuation through external stimuli such as heat. These intrinsically soft materials allow for large deformations, which are often reversible. [57,70] Shape morphing principles can be used in a wide range of polymers, hydrogels, LCEs, composites, and alloys.[57,71] LCEs are highlighted in the following sections regarding their unique properties.

LCEs are a type of thermoplastic elastomer that is soft and allows for large reversible deformations in response to external stimuli such as temperature and light. It possesses both isotropic elastic and crystalline anisotropic material properties and exhibits one more than the other depending on the temperature. Mesogens, the rigid molecules in liquid crystals, tend to self-organize in a fluid-like manner while in the nematic phase, which is the most common phase (see fig. 9).[66,72] This orientation remains mainly orientational and does not influence the position of the mesogens. In the smectic phase, on the other hand, mesogens are both orientationally and positionally oriented in a layer-like structure, causing a more solid structure.[73] By increasing the temperature above a certain threshold, the nematic state is reached, and this process can be reversible. [72] During the synthesis of the LCEs, the alignment of the liquid crystal molecules can be arranged into different orientations, causing different programmable motions when actuated.[72,74]

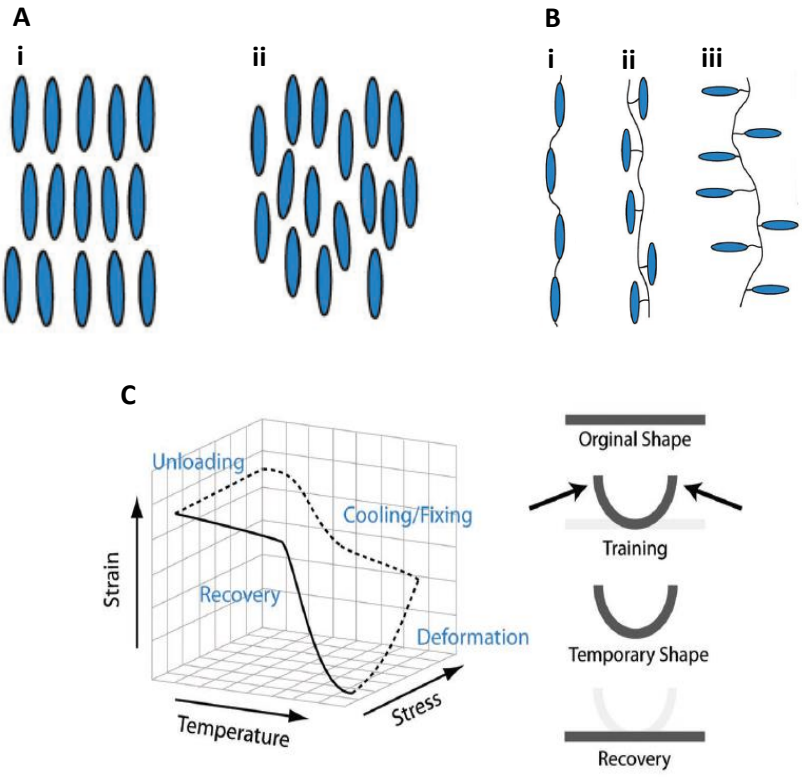

Figure 2.9 | Overview of liquid crystal elastomers and the programming of shape memory polymers. (**A**) Liquid crystal material phases. i, The smectic phase. ii, The nematic phase. (**B**). The attachment geometries for liquid crystal elastomers. i, Main-chain. ii, Side-on side-chain, more likely to be nematic. iii, End-on side-chain, more likely to be smectic (**B**) A thermomechanical cycle for a shape-memory polymer.[66]

Malachowski et al. presented a thermally responsive therapeutic gripper for controlled drug delivery that responds to body temperature (see fig. 2.10). The aptly called theragripper actively grips into tissue and can release drugs from its pores when introduced inside of the body after drug-loading the grippers via different methods. Drug-release parameters can be altered, ranging from a few hours to several days. The gripper is in a closed state at 4 °C before it gets introduced inside the body. Initially, the gripper is closed at a temperature of 4 °C but opens up when the solution temperature increases to 37 °C. However, the gripper closes again at body temperature, completing a full gripping motion in the temperature range between 4 °C and body temperature. When introduced into the esophagus of a pig, the gripper completed an entire cycle in approximately 5 minutes.

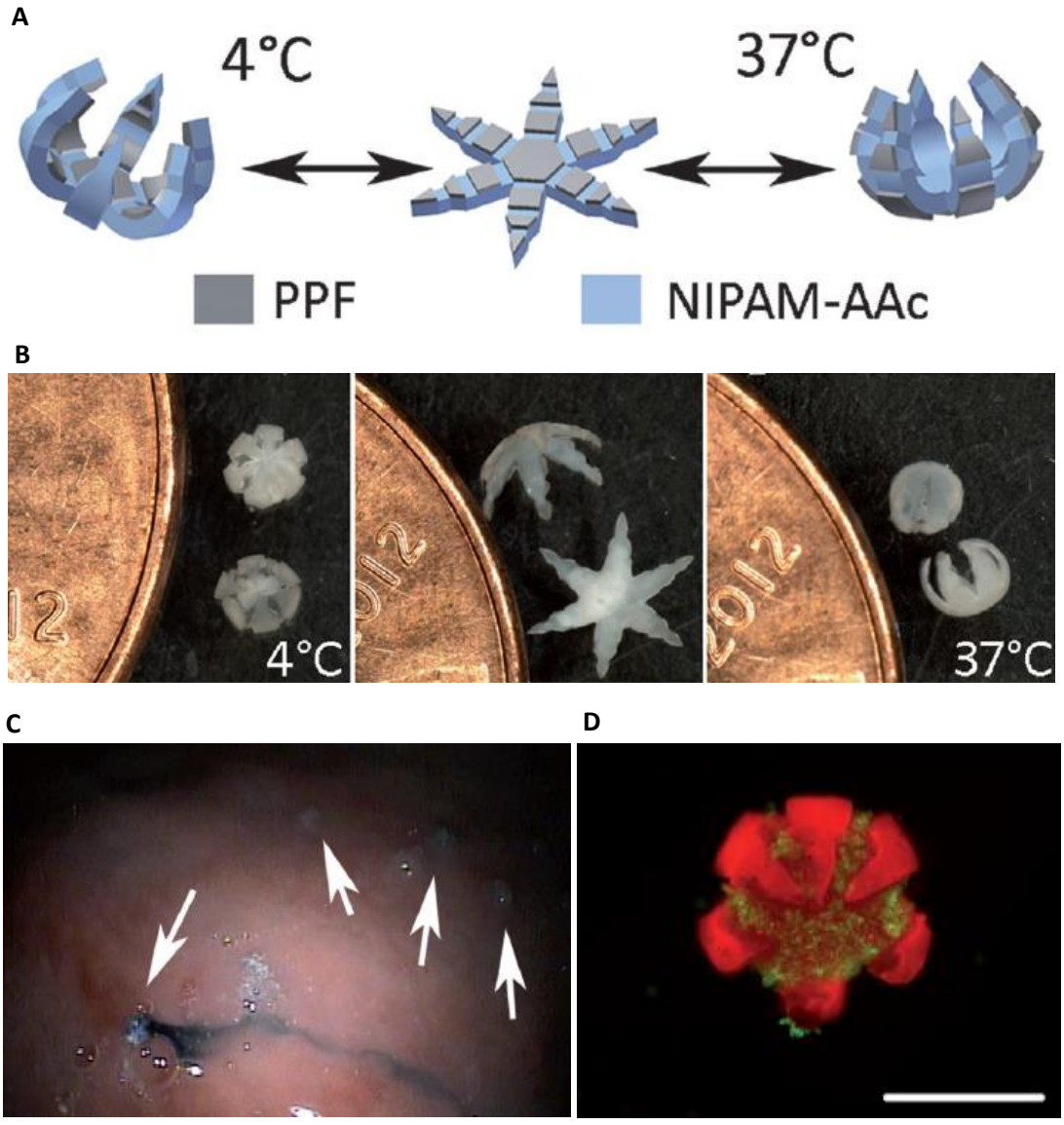

Figure 2.10 | Thermal actuation of the theragripper. (**A**) Graphic representation of the theragripper with poly (propylene fumarate) used for the biodegradable panels and poly (N-isopropylacrylamide-co-acrylic acid) for the hinges. (**B**) The realized structure is fully closed at 4 °C and 37 °C. While the temperature is increasing between the thresholds, the grippers are fully open. (**C**) Endoscopic image of multiple theragrippers in a porcine stomach. (**D**) Fluorescent image of a detached theragripper holding a clump of cells (scale bar is 1 mm).[75]

Even though Malachowski et al. were able to thermally actuate poly (N-isopropylacrylamide-co-acrylic acid) with a temperature that could possibly be safe for the human eye, it is one of the very few applications within this temperature range.[75] Thermally responsive actuation applications often require high-temperature differences to achieve the desired actuation. The human eye has a slightly lower than body temperature at 34.8 °C.[76] To create temperature differences, external heating would have to be applied. Alternatively, one could think of introducing a device previously held at a lower temperature and allowed to be heated, similar to the previously described example. With both of these methods being slow and inefficient, they could, more importantly, cause harm to the human eye.

2.2.5 Photo Responsive Actuation

Although actuation occurs via a different stimulus, materials mentioned under thermally responsive actuation can also be used here. Materials are chemically altered to respond to distinct types of lights. Visible, ultra-violet (UV), or near-infrared (NIR) light is used to actuate soft materials. Light-driven actuation requires materials, usually polymers, to contain photosensitive functional groups.[66] Three possible molecule groups can be added; photoisomerizable molecules, triphenylmethane leuco molecules, and photoreactive molecules.[66] Once a suitable material contains a photochromic molecule, optical signals are used to stimulate it converting them into property modifications.[56] Unfortunately, the same speed limitations present themselves here as well. However, NIR light therapy is becoming more popular for improving and repairing vision.[77] Certain red and NIR light wavelengths can reduce retinal inflammation and improve healing.[77] However, only the outer layer of a potential device would be responsive to irradiation, making the programming of this material quite intricate.[66] Wavelengths ranging between 600 and 1000 nm have been found to be healthy for use on the human eye.[77] Materials that respond to this range of wavelengths could potentially be an option for expanding the iris without causing any damage to vision.

2.2.6 Pressure Responsive Actuation

Soft Pneumatic Actuation

Since the first soft robotic application was the pneumatically driven McKibben artificial muscle from 1958, it is the first pressure-responsive type of actuation to be reviewed.[78] Pressure-driven actuation can be achieved both pneumatically and hydraulically. The geometrical configuration of the device plays a significant role in the efficiency of this mode of actuation.[79] Soft pneumatic actuators are topologically programmable.[57] They are highly scalable and often simple to produce depending on the application.[57,58,80] One of the main advantages is the ability to produce good intensities and forces on small scales, which is very useful for a micromanipulator in the anterior chamber of the eye.[56] However, this still requires a large and bulky device that has to provide pressurized gas for the actuation to occur in a safe and controller manner, similar to the case with magnetic actuation. Pneumatic actuation has the advantage of remaining lightweight, just like thermally and photo-responsive actuation, when a conventional gaseous fluid is used. [56] Depending on the ability of the used material to withstand the necessary pressures involved, pneumatic actuation can be a potential solution for expanding the iris. Examples of soft pneumatic actuation for different applications can be found in figure 2.11.

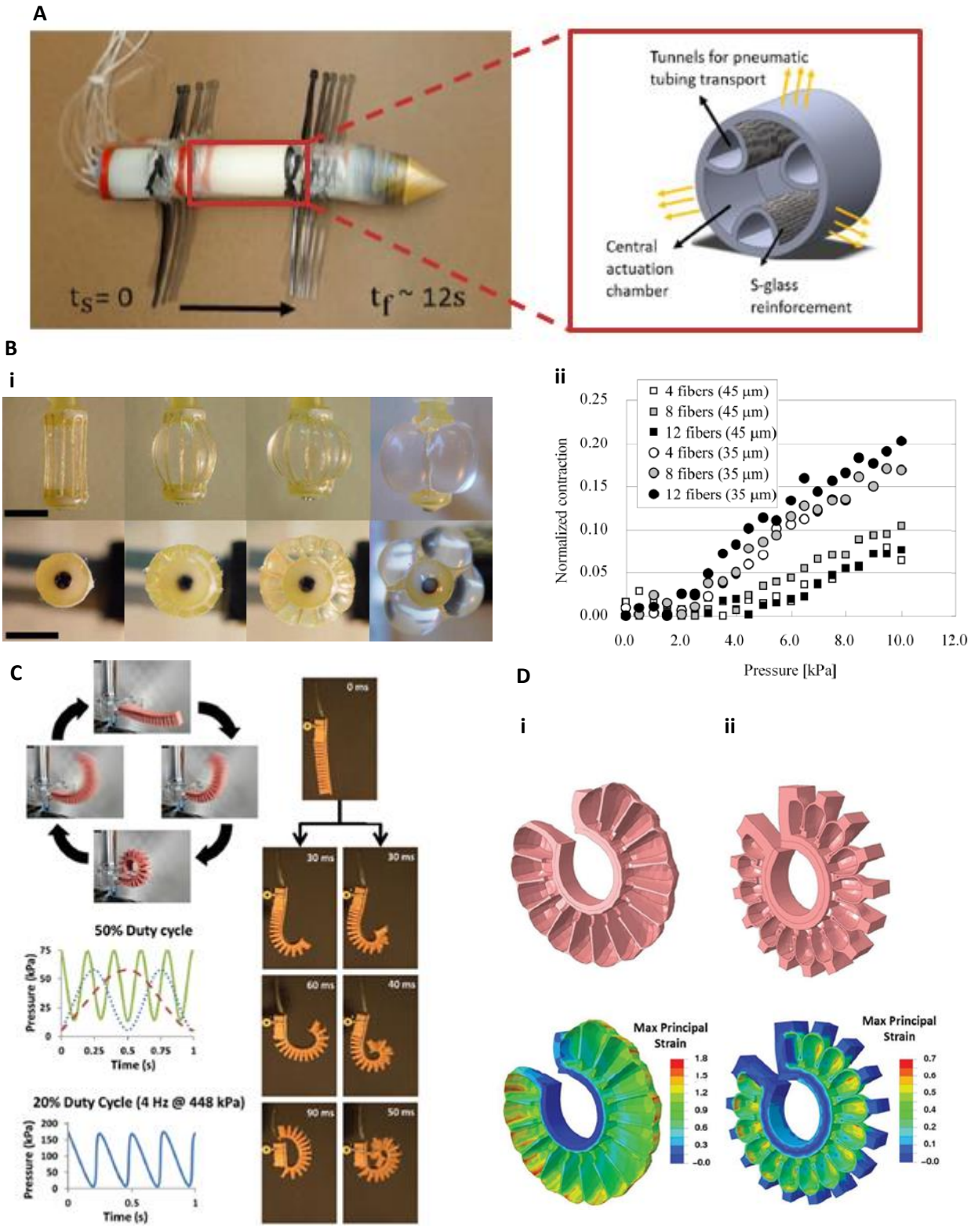

Figure 2.11 | Examples of pneumatically actuated soft materials. (**A**) One of few examples of radial pneumatic expansion. A tube with three reinforced channels is radially actuated to achieve gait in a wormlike, peristaltic robot.[81] (**B**) A silicon rubber tube with fibers running along its sides simulating a muscle. i, Different fibers led to different contractions and deformations in the tubes. Maximally 10 kPa was used to inflate the tubes (scale bar is 5 mm). ii, A decrease in fiber length caused increased contractions inside the tubes.[82] (**C**) Rapidly actuating pneunet. (**D**) Comparison between fast and slow pneunet. i, Schematic representation of a regular "slow" pneunet. ii, The geometrically modified fast pneunet, this pneunet was able to improve actuation speeds by 25 times and has very high repeatability.[80]

Soft Hydraulic Actuation

Closely related to pneumatic actuation is hydraulic actuation, as both can be categorized together as soft fluidic actuators. The main difference is that a liquid is used inside channels and chambers inside a device to achieve locomotion instead of a gaseous fluid. Here, liquids could spill and damage surrounding tissues instead of having the potential danger of a gas abruptly escaping through the soft material. However, the liquid used could be an OVD, which is provided intracamerally during cataract extraction and would therefore not cause any additional damage to the patient. Also, depending on the necessary range of motion, the liquid leads to additional mass.

Patient safety is maintained with both these actuation types, with the only danger being a potential rupture in the material causing either a sudden release of a gas or a liquid. Other than that, this actuation allows the use of intrinsically compliant materials that allow for a controlled and natural interaction between the device and the iris. The applied forces on the iris, range of motion, and actuation speed can all be controlled through geometrical optimization of the topology of the internal structure of the channels and chambers. The ratio between the fluidic chamber size, wall thickness, and distribution of the fluidic chamber will have the most significant influence on the motion of the device.[57] Any material that complies with the necessary stretchability to achieve the desired locomotion can be used in this case. Therefore, it allows the use of any biocompatible material the device requires for its application. Finally, since a pump will be present, the motion can be repeated as long as this pump is connected and running. The repeatability will solely depend on the material properties.

2.2.7 Chemically Responsive Actuation

Chemochemical motion transforms chemical energy into mechanical energy, achieving motion by applying stimuli such as varying the pH, humidity, or adding solvents.[62,66] To expand the iris, this method leads to uncertainties and could potentially be dangerous for the patient, mainly because the eye could be exposed to different chemicals that cause unwanted effects. Also, the actuation speed will vary greatly, and it will be challenging to control because the materials tend to be highly sensitive.[66] One such example is illustrated by Zhao et al. Rapid actuation was achieved by exposing a membrane to acetone vapor to have the flat membrane curl up in a circular motion creating a type of coil.[83] When put back in the air, the membrane regains its initial flat shape (see fig. 2.12). While the motion is very interesting for expanding the iris, it would have to be with different materials and chemical stimuli altogether.

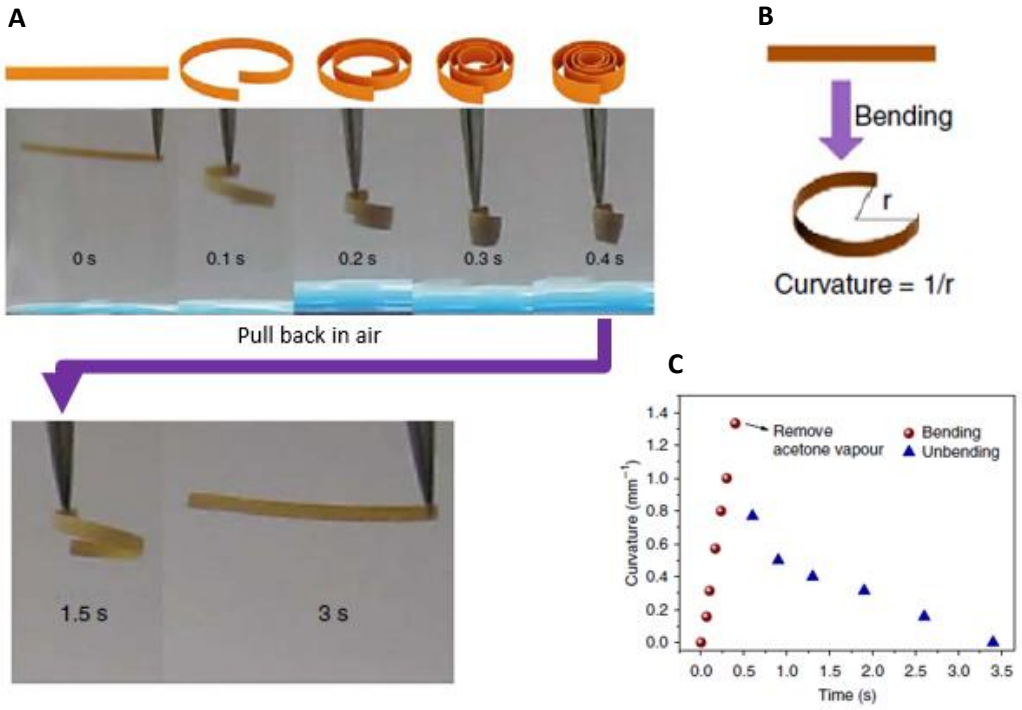

Figure 2.12 | Actuation of a thin membrane (1 mm x 20 mm x 30 µm). (**A**) Movement of a PILTf2N/C membrane when placed in acetone vapor and its return to the original shape when put back in the air. (**B**) Visual depiction of the curvature. (**C**) A plot of the curvature over time in the membrane for the full actuation range.[83]

2.2.8 Conclusions for Soft Actuation

Based on the literature findings regarding the different actuation types, a Pugh matrix is used to gain a clear overview of the best potential actuation types for a micromanipulator to expand the iris (Table 4). Unfortunately, few examples of the required sophisticated locomotion can be found in the literature. Most applications cater to soft actuated grippers that are usually limited to simple, small, unidirectional, and planar movements. At the same time, the technological readiness level for most soft robotic applications is still limited.[53] While describing the available soft actuation types, some were already excluded because of a lack of achievable safety for use inside the anterior chamber, or they could not comply with the device requirements of being biodegradable. Nevertheless, they could still be very viable options for other applications. Based on this table, it can be concluded that magnetic and fluidic actuation are suitable types of actuations for the intended purpose.

Criterion	Patient Safety	Compli-ance	Miniatu-rization	Control	Range of Motion	Force	Speed	Compati-bility	Repeat-ability
Electrical	-	0	0	+	+	+	+	0	++
Magnetic	+	+	+	++	+	+	++	+	++
Thermal	-	++	+	+	+	0	-	+	-
Photo	+	++	+	+	+	0	-	+	0
Pneumatic	+	++	0	++	+	+	++	+	++
Hydraulic	+	+	0	++	+	+	++	+	+
Chemical	-	-	+	-	+	+	+	-	-

Table 2.4 | Pugh Matrix. A rating of the discussed soft actuation techniques based on the literature. Current mechanical pupil expansion devices are taken as a baseline for the evaluation.

2.3 Soft Materials

2.3.1 Degradable Biomaterials

Based on the findings from the previous chapter, the potential types of soft actuation require, primarily, a compliant and stretchable material. In the literature, it is thanks to the chosen material and its properties that these large deformations, while maintaining mechanical resilience, are achieved.[56]

A Biodegradable Pupil Expander

Different materials are described, some of which are not only biocompatible but also degradable. A soft pupil expander is not meant to be implanted for prolonged durations of time but will only be used for short-term surgery. Therefore, biodegradability is not the preponderant criterion in the choice of material. However, it is an asset that helps prevent any avoidable patient health risks in the undesired case of device deterioration, mainly during deployment and retrieval. Potential particles left inside the eye would increase patient health risks exponentially, while cost-effectiveness would decrease owing to the employment of medications or rehospitalization.

Biomedical Applications

Degradable or resorbable biomaterials were mainly intended for biodegradable sutures and tissue engineering.[84,85] However, their use has been expanded to include drug delivery, implantable degradable devices, as well as, regenerative medicine, and biodegradable electronics.[84–87] Research into synthetic degradable polymers was started in the 1960s but has made tremendous progress since the early 2000s.[87] Polymers allow great chemical manipulation by altering processing conditions, changing their physical and mechanical properties in the final material.[84,87] When the degradation time is optimized accordingly, they can be used inside the body without the risks involved with removal surgery, saving lives and costs.[87,88]

Degradable Elastomers

Whereas polymers are any large molecules consisting of monomers, an elastomer is a type of polymer that exhibits elastic material properties. These elastomeric properties are desirable since biomedical devices are implanted in the human body, where the extracellular matrix shares these properties.[89] The stress-strain curve of these viscoelastic materials is non-linear and can recover from large deformations without permanent damage.[85,86,88,89] Since manipulating iris tissue is the final goal, these materials are perfectly compatible. The iris, just like elastomers, is considered to be a hyperelastic material.[51,90] Hyperelastic materials are (nearly) incompressible, with Poisson's ratio being close to 0.5.[91–93] Incompressibility means that their volume does not change under stress, like, for example, water.[93] Figure 13 goes into more detail regarding hyperelastic models. With material properties very similar to the iris, the aim is to prevent damaging it during actuation. Elastomers also have different degradation modes that can be tuned to alter the rate at which this happens before the elastomer breaks down into metabolic compounds safe for the body.[88] There is a range of biodegradable elastomers that are available today, thanks to the collective efforts of researchers from different fields collaborating.[87] For the purposes of mechanically expanding the iris, it is crucial that particles of the device do not cause any harm to the patient in case particulates were to fall inside the eye and into the vitreous humor. However, it is more interesting to look at what material would allow for the most extensive range of mechanical properties while still being accessible and cost-effective in its synthesis.

A

Hyperelastic material models

Neo-Hookean → $W = C_{10}\left(\bar{I}_1 - 3\right) + \frac{1}{D_1}\left(J_{el} - 1\right)^2$

Mooney-Rivlin → $W = C_{10}\left(\bar{I}_1 - 3\right) + C_{01}\left(\bar{I}_2 - 3\right) + \frac{1}{D_1}\left(J_{el} - 1\right)^2$

Yeoh → $W = \sum_{i=1}^{3} C_{i0}\left(\bar{I}_1 - 3\right)^i + \sum_{i=1}^{3} \frac{1}{D_i}\left(J_{el} - 1\right)^{2i}$

Arruda-Boyce → $W = \mu \sum_{i=1}^{5} \frac{C_i}{\lambda_m^{2i-2}}\left(\bar{I}_1^i - 3^i\right) + \frac{1}{D}\left(\frac{J_{el}^2 - 1}{2} - \ln\left(J_{el}\right)\right)$

Ogden → $W = \sum_{i=1}^{N} \frac{2\mu_i}{\alpha_i^2}\left(\bar{\lambda}_1^{\alpha_i} + \bar{\lambda}_2^{\alpha_i} + \bar{\lambda}_3^{\alpha_i} - 3\right) + \sum_{i=1}^{N} \frac{1}{D_i}\left(J_{el} - 1\right)^{2i}$

B

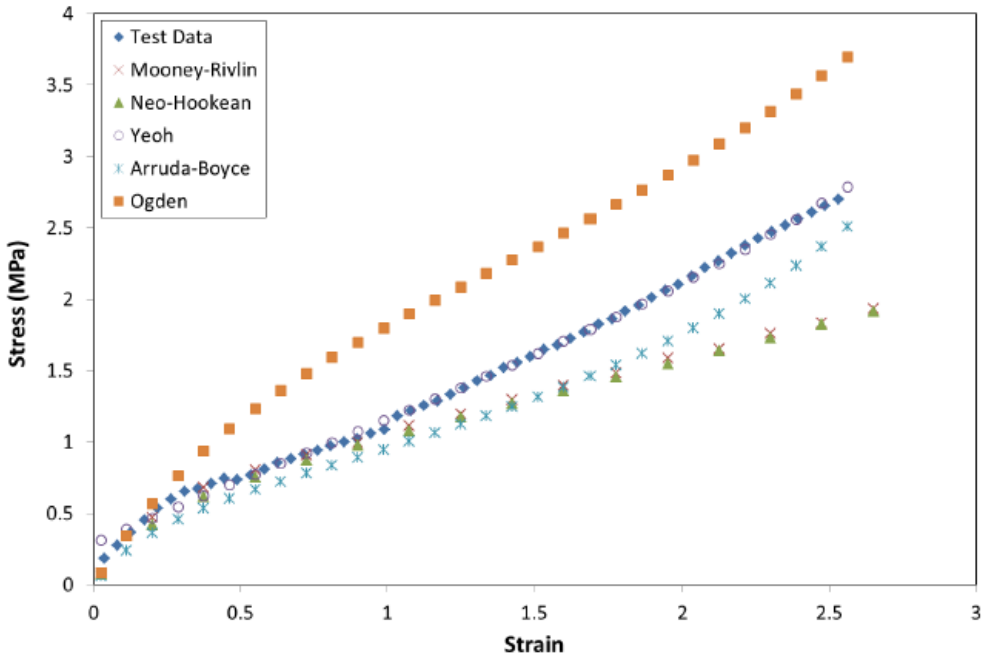

Figure 2.13 | Overview of hyperelastic material models. (**A**) Available hyperelastic material models that approximate elastic behavior and their analytical expressions. Experimental results obtained from uniaxial, biaxial, and planar tests are specified as nominal data to determine the hyperelastic material properties. This nominal data is then fitted against the analytical expressions for each model and material test separately.[94] (**B**) A stress-strain graph of the measured data where the results from a uniaxial material test are curve-fitted against the analytical expressions for the different material models to estimate the hyperelastic material model parameters. Tensile tests were performed on natural rubber using ASTM D638 dumbbells and a Lloyd LR10K extensometer to input the stress-strain data into Abaqus.[95]

2.3.2 Fabrication Methods

In the previous chapter, it was established that for fluidic elastomeric actuation, the geometrical features greatly influence the pattern and efficiency of actuation. For the elastomers listed above, there are different fabrication methods ranging from micropatterning and electrospinning, to different types of coating techniques.[96–98] In recent years, an emerging technique, additive manufacturing (AM) by means of 3-dimensional (3D) printing, has rapidly improved. [99,100] Compared with traditional manufacturing techniques, 3D printing soft elastomers allows complex geometries and high resolution, precision, and throughput.[100] Especially with stereolithography (SLA) and Digital Light Processing (DLP) 3D printing, both a type of photocuring 3D printing, are favorable for fabricating hollow structures.[101] Despite these advantages, it comes with other challenges and requires photocurable materials to even attempt.[100,102] Considering the range of applications, affinity with DLP, other possible fabrication methods, and the costs involved with processing these elastomers, a choice is made to further investigate the elastomer Poly (glycerol sebacate) Acrylate (PGSA).

2.3.3 Poly Glycerol Sebacate

Poly (glycerol sebacate) (PGS) was first introduced in 2002 by Wang et al. where the goal was to create a tough biodegradable elastomer that could withstand the harsh environment inside the human body.[89] It is a tough, hydrophobic, and inexpensive biodegradable elastomer, especially in comparison with most hydrogels.[85,89] Mainly because of this, hydrogels were excluded from this literature review. Additionally, 3D printed hydrogels face even more challenges than elastomers and could be very unpredictable with different liquids used inside of the anterior chamber of the eye during surgery because of their hydrophilic nature. PGS was intended to be a polymer with improved mechanical properties and biocompatibility compared to others.[89] Polycondensation of equimolar amounts of glycerol and sebacic acid yielded a three-dimensional network of randomly crosslinked coils.[89] The polymer has a small number of crosslinks and hydroxyl groups attached to its backbone that prevent it from being rigid and brittle.[89] Both glycerol and sebacic acid are basic building blocks for fatty acids in the human body and are therefore non-toxic and FDA-approved.[89] It features hydrolytic degradation to prevent differences in degradation characteristics caused by enzymes, meaning that ester bonds react with water molecules breaking them up into smaller chains.[86,88,89]

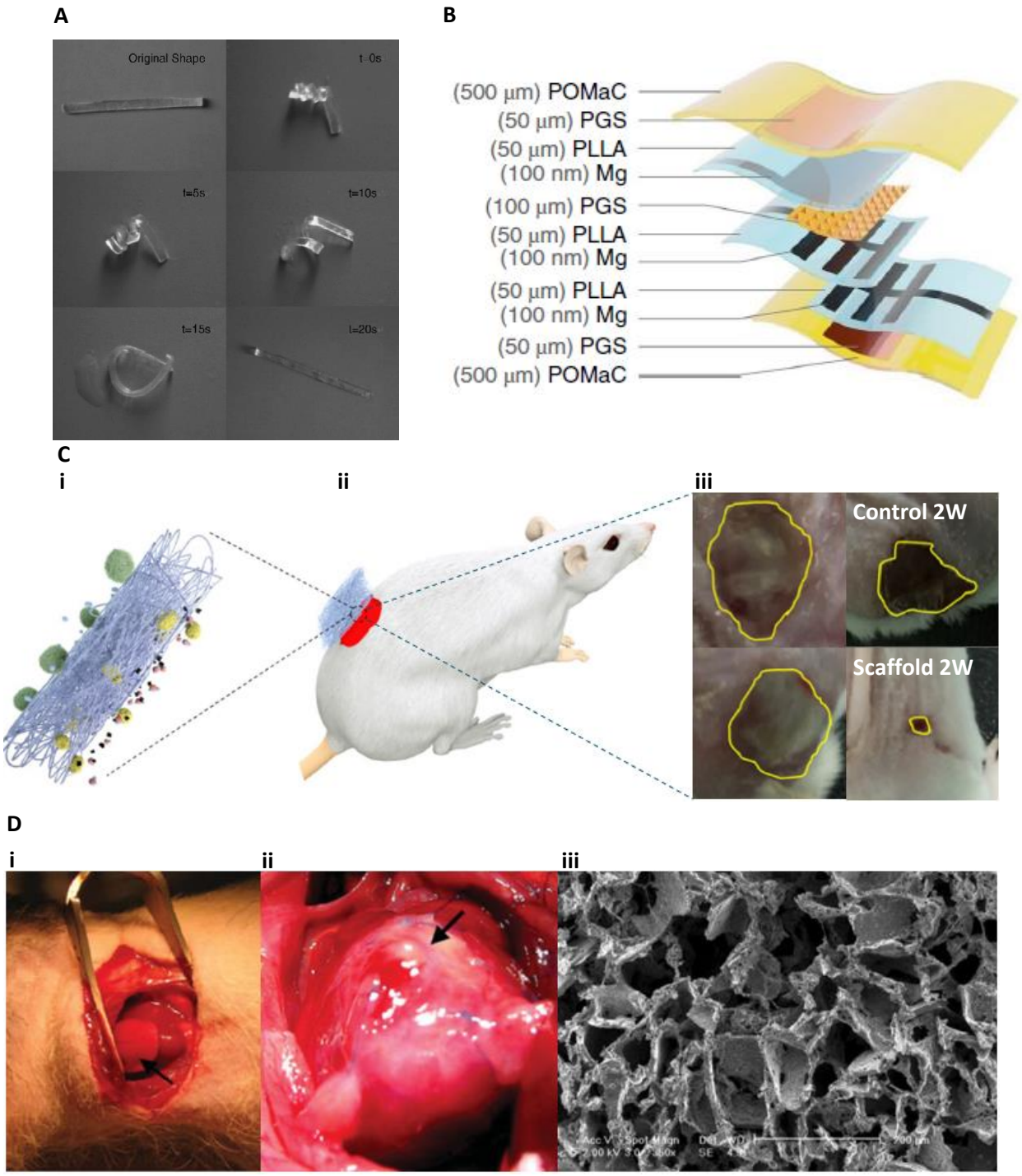

Figure 2.14 | Examples of PGS used for different biomedical applications. (**A**) Temperature-dependent shape memory effect was observed in PGS with a recovery ratio of 99.5%. The response temperature depends on the glass transition temperature, which can be retrieved by performing differential scanning calorimetry measurements.[103] (**B**) A fully biodegradable and stretchable strain and pressure sensor. PGS is used as a dielectric layer and a stretchable non-sticking layer in the pressure sensor and strain sensor, respectively. PGS is used as a non-sticking layer to allow relative sliding of the electrodes.[104] (**C**) Yang et al. electrospun a flexible PGS and poly-L-lactic acid scaffold to investigate the wound healing capacity on the back of a mouse. i, Electrospun scaffold. ii, An E. coli infected skin defect model on the back of a mouse. iii, The skin defect model of 1 cm^2 was able to heal 80% of the wound area after 14 days. When epidermal growth is considered, 95% of the wound healed after 14 days.[105] (**D**) i, A PGS scaffold in the shape of a 1.5 mm thick disk and a diameter of 1 cm was implanted in a nude rat and sutured over an infarct. ii, There was excellent integration between the host and graft, and blood vessel formation was observed two weeks after implantation. iii, SEM image of the PGS scaffold used for cardiac tissue.[106]

Synthesis of PGS

The synthesis procedure for PGS involves two steps and is straightforward, controllable, and relatively inexpensive.[89,96] First, polycondensation of an equimolar amount of glycerol and sebacic acid takes place under nitrogen or argon for 24 h.[89] Then, a second polycondensation step is performed under vacuum for another 48 h.[89] The mechanical and chemical properties of PGS can be altered by changing the synthesis parameters. The duration, temperature, and molar concentrations of the reactants can be adjusted.[89,96,107] Previous research presents several examples of this, one of them being Yeh et al., where the first step in nitrogen was performed for only two hours.[108]

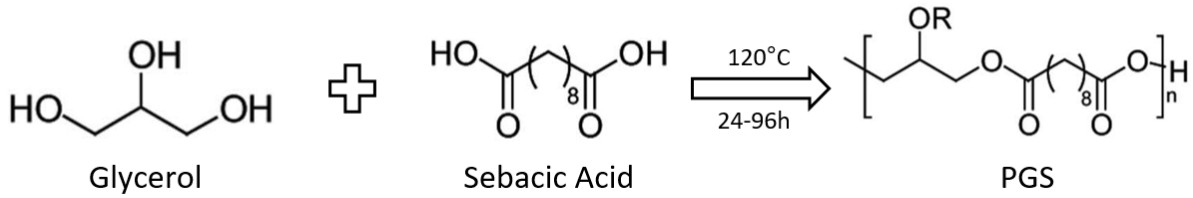

Figure 2.15 | Schematic representation of the chemical synthesis of PGS prepolymer. The synthesis parameters can be altered to influence the final prepolymer.

Because of the temperatures, pressures, and duration of this process, it is considered harsh and difficult to fabricate 3D structures.[96,107] Alternatives have been researched to simplify the fabrication of PGS, among those alternatives is to mix it with other materials.[96] Numerous applications of regular and modified versions of PGS can be found in the literature (see fig. 14). PGS is found in blends with other polymers, as a composite with inorganic materials, and other reactive moieties.[96,107,109–111] Since its inception, PGS has been used in tissue engineering, drug delivery, wound-healing, bioelectronics, soft robotics, and various implantable devices.[96,104,107,112]

2.3.4 Poly Glycerol Sebacate Acrylate

Different reactive moieties were added to PGS to make it photocurable.[96,109,113] Photocurable PGS in the form of poly glycerol sebacate itaconate (PGSI), poly glycerol sebacate methacrylate (PGSM), and PGSA was synthesized.[109,114,115] However, most literature caters to PGSA, primarily researched for DLP 3D printing fabrication techniques and cell cultures in recent years.[98,108,111,116–121] PGSA modifies PGS with acrylates that control the crosslinking process and introduce new processing options. [109] By altering the degree of this acrylation, even more control over the properties of the elastomer can be realized.[122] To acrylate PGS, acryloyl chloride is added in different molar ratios along with other reactants that aid in the acrylation process.[109,121,122]

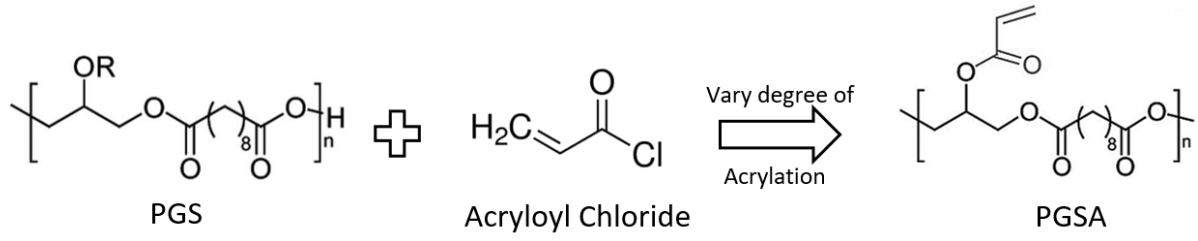

Figure 2.16 | Schematic representation of the chemical synthesis of PGSA prepolymer. The degree of acrylation can be altered to influence the properties of the final prepolymer even further.

In the work of Wu et al., DLP 3D printing was achieved for the first time without adding any other copolymers to PGSA.[121] The work of Chen et al. was the first to successfully use additive manufacturing with DLP by using polycaprolactone diacrylate (PCLDA) and polyethylene glycol diacrylate (PEGDA) as copolymers.[110] Wu et al. achieved features sizes of 80 µm using printed layer thicknesses of 10 µm, allowing for fast printing while maintaining a good resolution for the features (see fig. 2.17).[121] Postprocessing by means of UV-light and thermal curing altered the mechanical and chemical properties even more, rendering PGSA more advantageous than PGS regarding the range of achievable material properties.[121] However, for application in vascular cells, even smaller features were necessary, and other methods of additive manufacturing, for example, two-photon polymerization, can be used to realize this.[121] However, to safely expand the iris, based on the findings from the previous chapters, the realized feature sizes would already allow for micrometer-scale devices. Considering previous examples from the field of soft robotics and the tunable characteristics of this biodegradable elastomer, a soft mechanical iris manipulator is achievable.

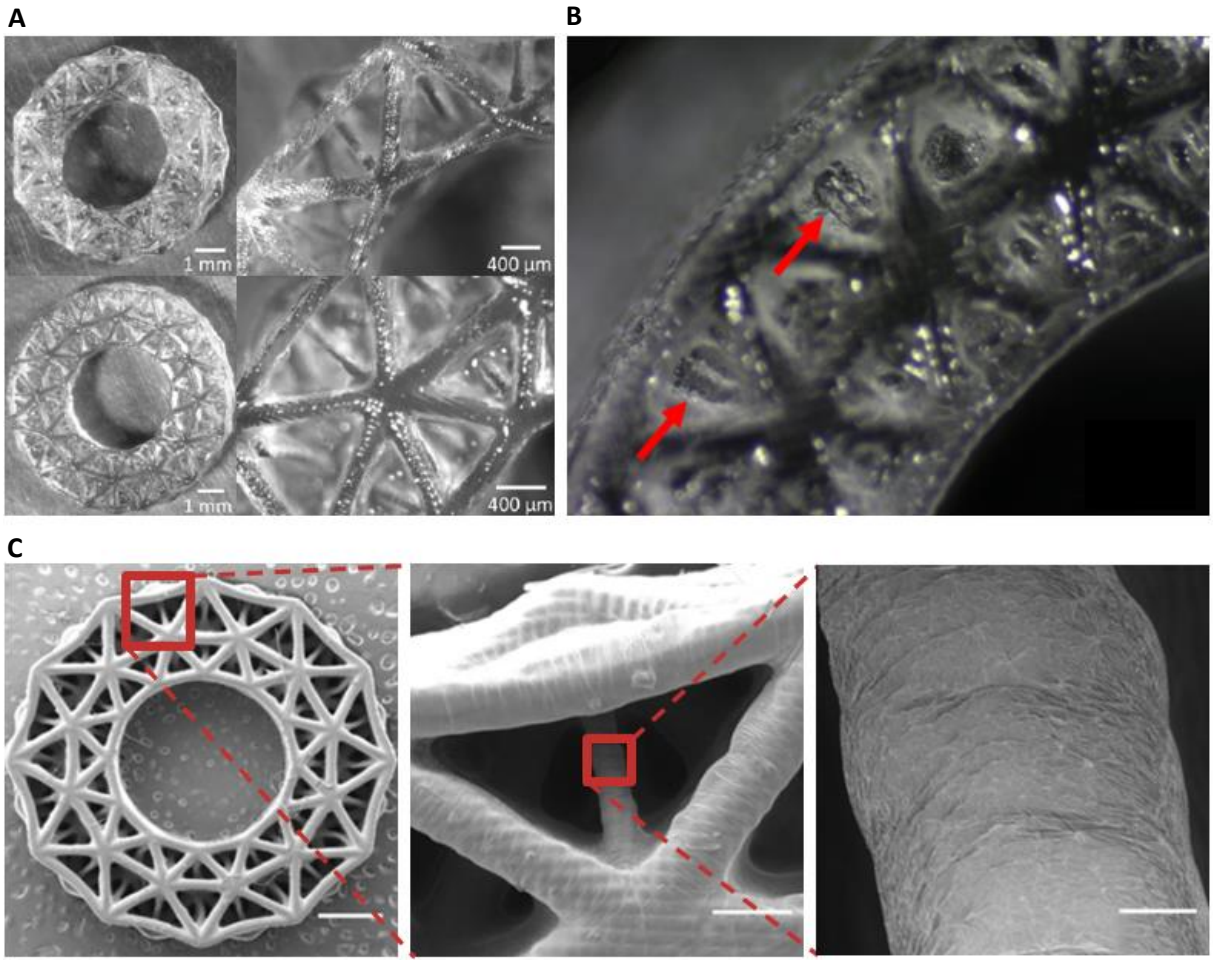

Figure 2.17 | 3D printed PGSA as a scaffold for regenerating elastic tissues. (**A**) Printed scaffolds of different tubular structures. (**B**) Close-up image of PGSA struts underneath the surface (scale bar is 200 µm). (**c**) SEM images of different magnifications highlighting the surface morphology of printed PGSA (scale bars are 1 mm, 200 µm, and 20 µm).

2.4 Conclusions from the Literature Review

A cataract is the opacification of the human crystalline lens caused by the aggregation of the α, β, and γ-crystallin proteins that migrate from the lens epithelium to the nucleus. Primarily due to age, some co-morbidities, and the continuously increasing life expectancy, leading to an increase in the prevalence of people afflicted. Being the number one leading cause of blindness worldwide, it is becoming easier to treat this condition and regain eyesight thanks to the incredible advancements in the healthcare industry. While couching is still present in the developing world, phacoemulsification cataract surgery has made extracting a cataractous lens efficient and affordable in the developed world. Although the success rate of this procedure is ranked number one of all performed surgeries, at the very least, two million patients suffer from small pupils causing surgery to be less cost-effective and, more importantly, entailing increased health risks. However, room for improvement is left for pupil expansion devices that aid cataract extraction in small pupils. A softer approach should be used for such devices to help this remaining group of patients benefit from modern cataract surgery.

To this end, different soft actuation methods were highlighted and evaluated based on current research in the field of soft robotic actuation. These methods were then rated based on the criteria required for a new generation of mechanical pupil expansion. Soft fluidic and magnetic actuation could potentially be good candidates to achieve this, owing to their safety, miniaturization, and compatibility with compliant biomaterials.

Regarding the biomaterials, PGS and its acrylated moiety PGSA have been used for a plethora of biomedical applications over the past two decades, of which only a few are highlighted. Thanks to this popularity, it has been researched extensively, resulting in a continuously growing field of application and different fabrication methods. 3D printing is one of those methods which allows omitting the struggles that come with fabricating complex geometrical structures for fluidic actuation.

3 Thesis Aim and Objectives

This chapter gives a detailed overview of the overarching aim of this project and the research objectives leading toward this goal.

3.1 Thesis Aim

Based on the conclusions from the literature review, a new generation of mechanical pupil expansion devices has to be developed to address small pupils in cataract surgery. Therefore, this thesis aims **to design and fabricate a soft robotic mechanical pupil expansion device controlled by fluidic or magnetic actuation to improve surgical outcomes of cataract extraction surgery in patients suffering from small pupils.** The device should allow the surgeon to fully control the pupil diameter at any given time during the surgery. The final device will not only compete with the current state-of-the-art concerning safety and achieved visual equity but also regarding cost-effectiveness and operative times. The material for this device should exhibit mechanical properties similar to that of the human iris to prevent any risk of iris tissue damage. In addition, the selected material should be biocompatible since it will be in direct contact with the eye. Finally, selecting a biodegradable material would have two advantages: 1) In terms of safety, if the soft actuator were to be improperly or incompletely removed after surgery, or if particulates of the device were to detach, they would degrade naturally without risking long-term inflammation; 2) The use of biodegradable materials would reduce waste since the pupil expansion device will be designed to be a single-use tool that is discarded after use.

3.2 Thesis Objectives

The main objective of this thesis is to provide the necessary groundwork for developing a new generation of soft robotic pupil expansion devices. For this purpose, the main objective was split into smaller sub-objectives that are formulated as follows:

1. **Synthesize the selected soft elastomeric materials based on the conclusions of the literature review:**

Based on the findings of the literature review, the present thesis will focus on the synthesis of PGS and PGSA. These two materials display an extensive range of mechanical properties depending on the synthesis parameters, which will be explored considering the requirements of the application.

2. **DLP 3D print the materials for soft fluidic actuation:**

Both the synthesized material and the DLP printer have not been used for the purposes discussed in this project. Therefore, the material, the chemical properties, and corresponding printer settings will have to be optimized to enable the printing of a soft-actuated device.

3. **Incorporate magnetic particulates into the material for magnetically-controlled actuation:**

Magnetic actuation is a potential approach to control the device studied in this thesis. This type of actuation implies the development of elastomeric composites with both the required magnetic and mechanical properties. For this purpose, magnetic particles will be incorporated into the elastomeric matrix of the materials investigated above.

4. **Characterize the mechanical and chemical properties of the synthesized materials:**

After synthesizing the materials, they must be characterized to extract relevant information for the fabrication process, use in the final application, and provide a basic understanding of their functionality.

5. **Derive hyperelastic material model parameters for simulation purposes:**

In finite element modeling, a hyperelastic material model simulates hyperelastic materials such as PGSA and iris tissue. Providing model parameters will allow basic simulation with the synthesized materials resulting from this thesis.

6. **Fabricate a soft pupil expansion device prototype**

If the previous objectives are reached, a device prototype can be designed and fabricated by means of 3D printing with a biomaterial.

7. **Demonstrate the actuation of the prototypes:**

When all other objectives are achieved, the last objective will be to demonstrate the actuation of the fabricated prototypes based on fluidic and magnetic actuation.

4 Materials and Methods

This chapter goes over the materials and methods used in this thesis. First, the synthesis of the primary materials is described. Then, the fabrication methods to achieve device prototypes are explained, and finally, the various experimental setups are discussed.

4.1 Material Synthesis

All materials discussed in the following section were synthesized using various facilities of the Else Kooi Laboratory (EKL) in Delft. All chemicals were handled safely and within the regulations set by EKL staff members. A detailed protocol for the synthesis of the main biomaterial PGSA is provided in the appendix.

4.1.1 Synthesis of PGS

The synthesis of PGS prepolymer is achieved via a polycondensation reaction. An equimolar amount of the reagents glycerol and sebacic acid were added into a three-neck round bottom flask and heated to 120 °C after purging three times using vacuum and nitrogen atmospheres. A condenser was used to retrieve cooled vapors generated during the reaction. Reagents were allowed to polycondensate for 2 hours under a nitrogen atmosphere. Subsequently, after this first polycondensation step, the mixture was placed inside a vacuum oven at 120 °C and was allowed to cross-link for an additional 24 – 96 hours to attain PGS prepolymer of different levels of cross-linking. PGS prepolymer was kept in a fridge at 4 °C until further use.

4.1.2 Synthesis of PGSA

For the synthesis of PGSA, a mixture of 10% (w/v) PGS prepolymer, 0.01% (w/v) 4-(dimethylamino) pyridine, and 0.005% (w/v) 4-methoxyphenol were dissolved in anhydrous dichloromethane in a round-bottom flask. The mixture was cooled to 0 °C under a nitrogen flow before the acrylating chemicals acryloyl chloride and triethylamine were slowly added in equimolar amounts. The amount of acryloyl chloride is dependent on the desired degree of acrylation.

Different molar ratios of acryloyl chloride: hydroxyl groups in PGS were slowly added to the mixture under the exclusion of light. Different amounts of acryloyl chloride were added, ranging from 0.3 to 0.6 mol acryloyl chloride per mol of hydroxyl groups. Acryloyl chloride reacts with the available hydroxyl group from the glycerol to form functionalized groups. Like previous works on PGSA, it was assumed that two of the three hydroxyl groups in glycerol reacted with sebacic acid during the first polycondensation step. This gives 3.9 mmol of hydroxyl groups per gram of PGS prepolymer.[109] The mixture was left to react for 24 hours at room temperature while being stirred on a magnetic stirrer.

After the reaction, another 0.005% (w/v) 4-methoxyphenol was added to the mixture before a rotary evaporator was used to remove anhydrous dichloromethane at a pressure of 450 mbar. The acquired viscous mixture was then dissolved in an equivalent volume of ethyl acetate. After dissolving, the mixture was vacuum filtered repeatedly until a clear solution was obtained by removing triethylamine salts that formed during the acrylation process. The number of required vacuum filtrations depends on the degree of acrylation since an increased amount of triethylamine increases the concentration of triethylamine salts. A 30 mM hydrochloric acid solution was used to wash the mixture to remove any remaining impurities. Sodium sulfate was used to dry the solution after using a separation funnel to dispose of the acid solution, and the rotary evaporator was used again to remove ethyl acetate. The pressure was decreased further to 99 mbar for the removal of ethyl acetate. PGSA prepolymer was covered from light and kept in a fridge at 4 °C until further use.

4.1.3 Synthesis of PGSA Ink

Before printing PGSA, it was mixed with 1 weight percentage (wt%) diphenyl(2,4,6-trimethylbenzoyl) phosphine oxide (TPO). The photoinitiator is necessary to allow faster printing of the already photocurable PGSA, and is completely miscible in the polymer. TPO can be used for both hydrophobic as well as hydrophilic polymers (amphoteric) and provides a suitable absorbance range for the Asiga Max X, which provides LED wavelengths of 385 nm (see fig. 4.1 A).[116] TPO is a type 1 photoinitiator indicating that the functional groups form radicals through a cleavage reaction (see fig. 4.1 C).[123] After measuring the weights, PGSA, TPO, and a magnetic stir bar were added to a glass vial and were allowed to mix on a magnetic stirrer for at least 1 hour (see fig. 4.1 B). For lower degrees of acrylation, it is recommended to dilute the PGSA ink using dimethyl sulfoxide (DMSO) and 2-butoxyethanol (EGBEA). Inks with high viscosity are more challenging to produce successful 3D prints with DLP. PGSA prepolymer can be dissolved in a 1:1 mixture of DMSO/EGBEA at different wt% depending on the degree of acrylation. A magnetic stir bar remover was used to remove the stir bar while the ink was stored under the same conditions as the PGSA prepolymer.

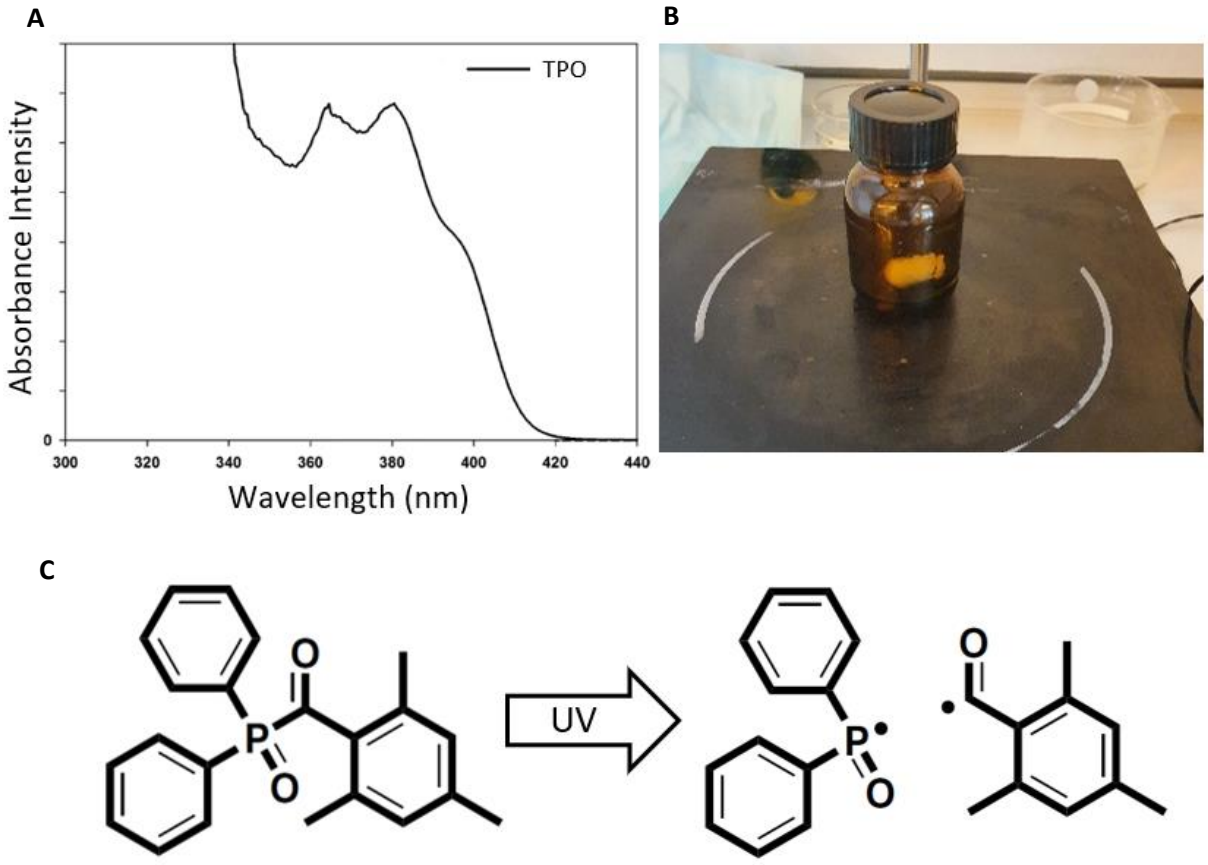

Figure 4.1 | TPO compatibility with the Asiga Max X. (**A**) UV spectrum of TPO showing its compatibility with a wavelength of 385 nm, which makes it a compatible photoinitiator for the Asiga Max X. [116,123] (**B**) PGSA being mixed with TPO with a magnetic stir bar on a magnetic stirrer. (**C**) The cleavage reaction of TPO when irradiated with UV light.[124]

4.1.4 Synthesis of PGSA Composite

Two types of magnetic particles were mixed with the PGSA ink described in the previous section, iron(III) oxide (Sigma-Aldrich, cat. no. 310050) and carbonyl iron (Sigma-Aldrich, cat. no. 44890) powders, which are both well-established biocompatible and biodegradable metal oxides. [125] After adding the iron particles to PGSA ink in a glass vial, the mixture was heated to approximately 80 °C and was stirred for different durations between 3 and 10 minutes with a metal lab spoon to study the possibilities of achieving a biodegradable composite ink. The PGSA composite mixtures were stored under the same conditions as the PGSA prepolymer.

4.2 Device Fabrication

In this section, device fabrication steps are explained. Both molding and 3D printing are discussed.

4.2.1 Soft Actuator Fabrication Based on Molded PGS

3D Fabrication of PDMS molds

3D printed shapes were designed in Solidworks and printed with an Asiga Max X, using Moiin tech clear as resin. A 4-inch silicon wafer, along with the printed shapes, were then bound to the bottom of two separate 4-inch wafer boxes (see fig. 4.2) and silanized in a desiccator under vacuum using approximately ten small droplets of trichloro(1H,1H,2H,2H-perfluorooctyl)silane (Sigma-Aldrich, cat. no. 448931) as a demolding agent (see fig 4.3). Silanization is an essential step that facilitates the detachment of PDMS from any silanized surface. The samples remained inside the desiccator for 1-2 hours until the silane was fully evaporated onto the samples.

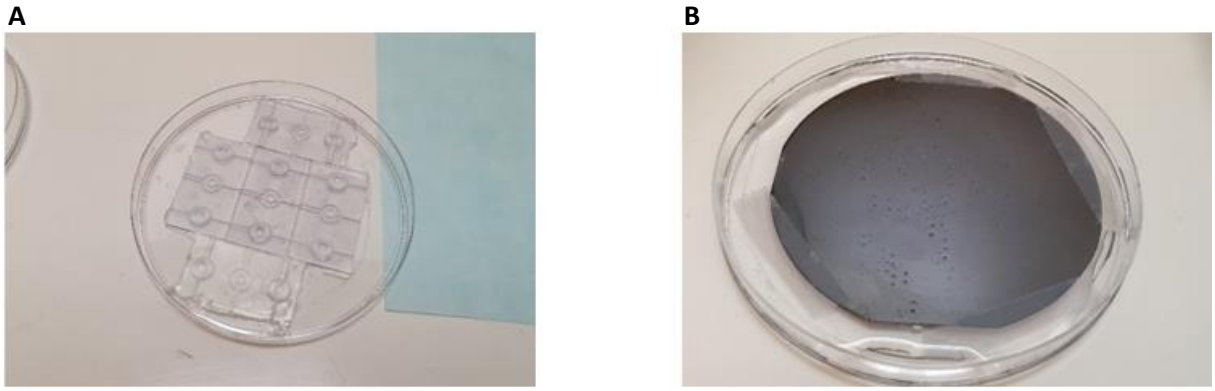

Figure 4.2 | Wafer box with structures attached with double stick tape. (**A**) 3D printed shapes that provide three layers to be stacked together after demolding. (**B**) A silicon wafer is used to provide a fully flat surface that serves as a substrate.

Polydimethylsiloxane (PDMS) was fabricated using the Sylgard 184 silicone elastomer kit in a 15:1 ratio. The PDMS was poured onto the samples and put back inside a desiccator for degassing. After degassing, the wafer boxes were thermally cured in an oven at 80 °C for a duration ranging from 1-2 hours.

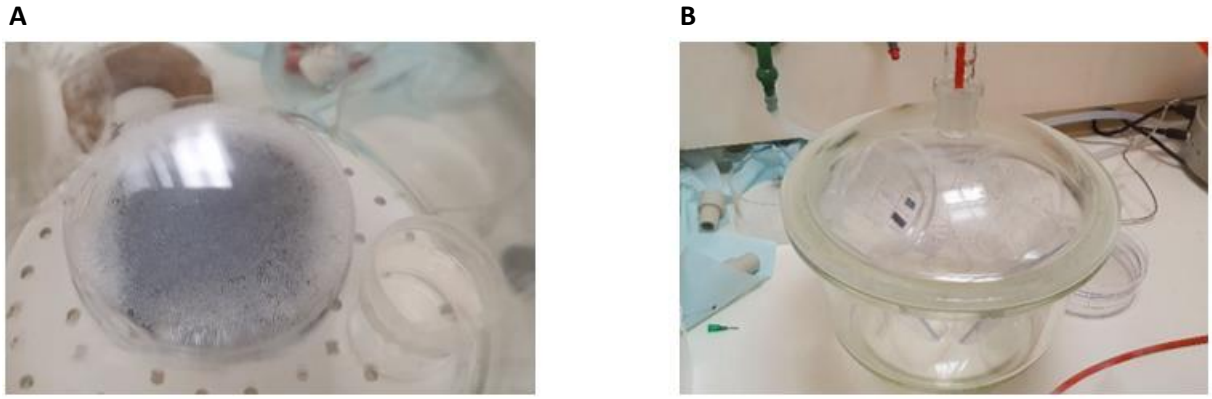

Figure 4.3 | Degassing and silanization in a desiccator. (**A**) Degassing of PDMS that was poured into a wafer box. (**B**) Silanization in a desiccator until the small volume of trichloro(1H,1H,2H,2H-perfluorooctyl)silane is fully evaporated.

Once cured, PDMS molds were retrieved from the wafer boxes by carefully cutting around the edges of the structures. Tape was used to remove any PDMS residues from the samples before silanization of the PDMS molds according to the previously described process. The molds resulting from the 3D printed shapes were then bound to the flat side of the PDMS substrate that was recovered from the wafer box with the silicon wafer.

PGS molding and thermal-curing

PGS was then heated so that it could be injected with a dispensing tip on a syringe. After injecting the bounded samples, thermal curing was provided for different durations and temperatures in glass Petri dishes to prevent any leakage into the oven. Other substrates were prepared simultaneously to study which substrate is best suitable for PGS fabrication via PDMS molds (see fig. 4.4).

Figure 4.4 | Preparation of PDMS molds for injection. Different substrates are used to contain the prepolymer within the PDMS mold. From left to right; Teflon, PDMS, and glass. Scale bar is 20 mm.

PGS molded parts assembly

The aim is to thermally cure the three separately demolded PGS samples into one structure, possessing an internal channel to allow for pneumatic actuation (see fig. 4.5). When the layers are partially cured, they can be aligned, stacked, and thermally cured to achieve a unified structure. Uncured PGS can potentially be added between the layers to help with adhesion while simultaneously acting as a sealant preventing air from escaping while actuation is ongoing.

Figure 4.5 | Three layers of the demolded device. (**A**) Cross-sectional overview of the device with the internal chamber. (**B**) The three layers of the device with the top part slightly lifted to show the internal structure.

4.2.2 Soft Actuator Fabrication Based on Molded PGSA and PGSA Composites

Molding of PGSA and PGSA magnetic composites in PDMS molds

Similar to the process described in the previous section for PGS, PGSA can also be fabricated using PDMS molds. PGSA and its composites can be directly injected into the molds without prior heating and do not have to be cured thermally. A Philips UV lamp with a wavelength ranging between 300 and 500 nm and unknown light intensity was used for different durations to cure PGSA and PGSA composites, which will be designated as PGSAUV and PGSAC, respectively.

PGSA magnetic composite molded with various magnetization conditions

With this method, magnetically active PGSA composite rings were fabricated. The ring shapes are realized by two identical PDMS molds bound together before injection of the PGSAC ink. A circular magnetic ring was made using six permanent magnets on the outside perimeter of a small plastic bottle with a diameter of 25 mm. Before curing the injected molds, they were placed inside of this magnetic ring in an effort to align the magnetic particles present in the PGSA matrix in a radial configuration. Two other alignments are also realized with the setups described in figure 4.6.

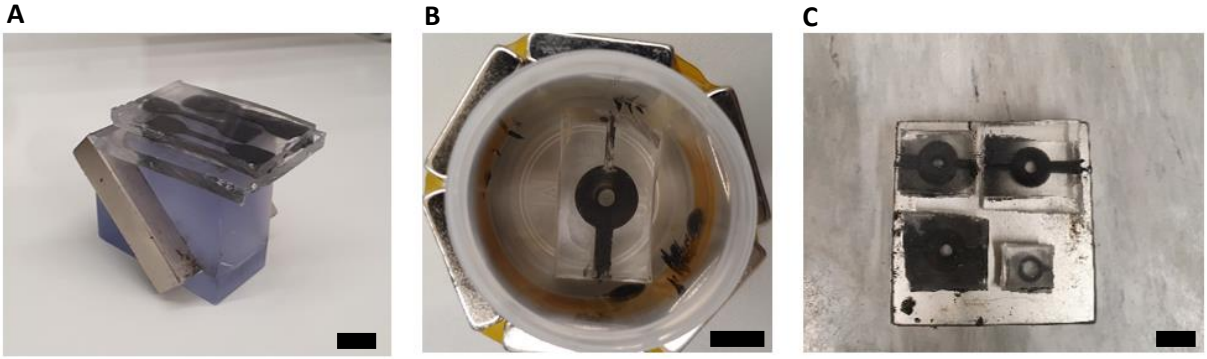

Figure 4.6 | Injected PDMS molds with varying magnetic alignments. (**A**) A 45 ° angle with the flat PGSA composite samples being attracted to the slanted permanent magnet. (**B**) Radial magnetic particle alignment. (**C**) Flat samples with magnetic particles aligned vertically toward the permanent magnet. Scale bars are 10 mm.

4.2.3 Soft Actuator Fabrication Based on 3D Printed PGSA

Different PGSA inks were prepared with varying degrees of acrylation and ratios of solvents. To derive accurate Asiga Max X printer settings for these new materials, a modified approach from the "Asiga Material Configuration File Creation" document was utilized. This file aided in deriving the printer settings for the newly introduced materials. A detailed description of the modified steps will only be shared with the immediate users of the printer at ECTM and the thesis committee, for confidentiality and intellectual property reasons, at the request of Asiga.

Varying the degree of acrylation of PGSA has a direct impact on the properties of the final material and, therefore, also the characteristics before printing. Mainly the density is affected by the degree of acrylation, causing a decrease in viscosity with an increased degree of acrylation. Therefore, it was necessary for some PGSA inks to alter their viscosity in order for them to be compatible with the Asiga Max X. While in the literature, DMSO and EGBEA were used to alter the viscosity of PGSA inks, in this work, ethyl acetate was also used as a means of altering the viscosity when necessary.

A

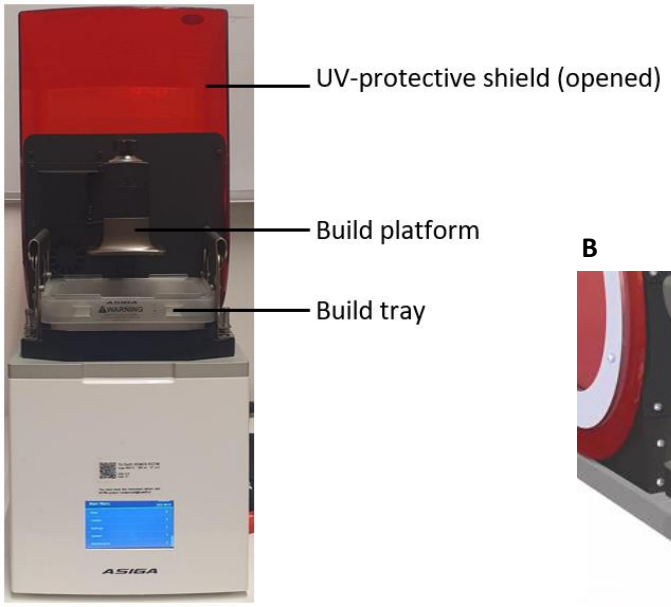

B

Figure 4.7 | Asiga Max X overview. (**A**) The Asiga Max X. (**B**) A closer look at the position of the build tray. The LED is highlighted in yellow, and the positioning sensors are highlighted in green.[126]

The Asiga Max X is a DLP printer with a build platform that allows structures with a maximum volume of 51.8 x 29.2 x 75 mm (see fig. 4.7). It can provide a pixel resolution of 27 µm in the flat XY plane, while the Z plane that determines the layer thickness can be set by the user and has been verified to work with a thickness as low as 5 µm. The LED wavelength is 385 nm, and the light intensity can be set between 0 and 60.58 mW/cm^2. DLP printing is a form of additive manufacturing owing to its layer-by-layer photocuring in order to realize the designed build.

4.2.4 Soft Actuator Fabrication Based on 3D Printed PGSA Magnetic Composite

No examples of DLP 3D printed polymeric magnetic materials were found in previous works. To investigate the compatibility of this type of 3D manufacturing with such a material, the PGSA composites described in section 4.1.4 were subjected to similar processes as the PGSA ink to define the printer settings.

4.3 Material Characterization of PGS and PGSA Prepolymers

The methods for both mechanical and chemical tests for the characterization of the synthesized materials are explained in this section.

4.3.1 Mechanical Properties

Mechanical properties of PGS were studied using uniaxial tensile testing. The stored PGS prepolymer was heated in an oven to 120 °C for approximately 30 minutes to regain its liquid form in order to dispense it into a silanized flat glass Petri dish (see fig. 4.8 A). A thin layer of PGS formed on the bottom of the Petri dish and was placed inside of an oven at different temperatures to thermally cross-link for varying durations. The PGS film was cut into rectangular shapes and subsequently soaked in Dulbecco's Phosphate Buffered Saline (PBS) before tensile tests were conducted (see fig. 4.8 B).

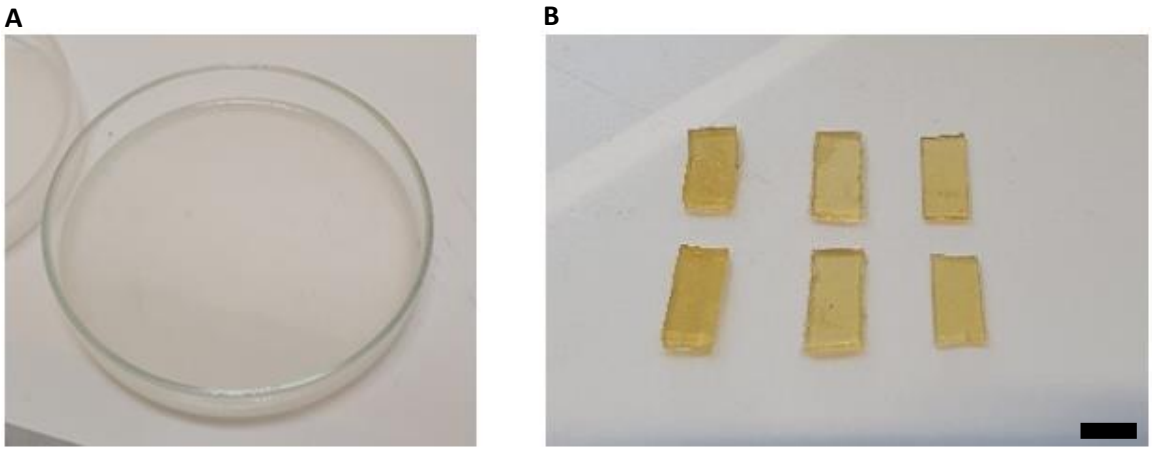

Figure 4.8 | Fabrication of rectangular PGS. (**A**) PGS dispensed into a glass Petri dish. (**B**) Rectangular PGS for use during uniaxial tensile testing. Scale bar is 10 mm.

Tensile test parameters

Tensile tests were performed at the Materials Lab at the Industrial Design Faculty in Delft on a Q800 dynamic mechanical analysis (DMA) test bench. The preload force was set to 50 mN, with an initial strain of 1% and a strain rate of $1\%{\cdot}s^{-1}$ of the gauge length.

Fabrication of PGSA samples for tensile tests

Mechanical properties of PGSA were studied using similar uniaxial tensile testing as described for PGS. Dumbbell-shaped PGSA specimens were fabricated with PDMS molds and the 3D printer adhering to ASTM D412 Type C standards (see fig. 4.9). PDMS molds were prepared and injected according to the methods described in section 4.2.1. An STL file of the dumbbell shape was imported into the Asiga Composer software, and slice thicknesses of 20 µm were used to 3D print the samples.

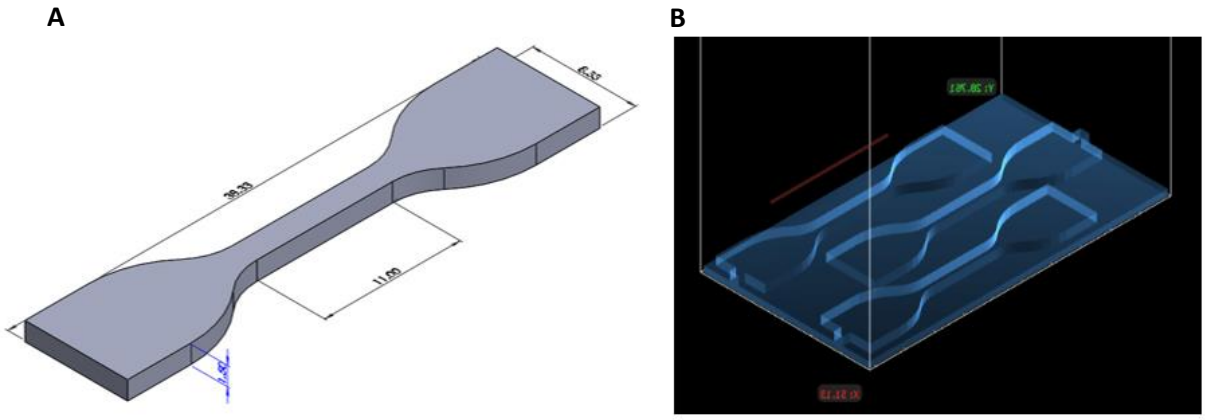

Figure 4.9 | ASTM D412 dumbbell shapes. (**A**) CAD model of ASTM standard with an adjusted size to fit the build platform and gauge width used in previous studies**.** (**B**) Overview of 3D print in the Asiga composer software used for PDMS molds.

All samples were washed in ethanol for 24 hours and subsequently soaked in PBS for another 24 hours to remove soluble fractions before mechanical testing. Paper frames were used to help ease the handling of the sticky materials and increase the grip between the clamps of the DMA Q800 (see fig. 4.10). The paper frames were cut out using a Silhouette Studio CAMEO 4 blade cutter. Samples were elongated until failure with a preload force of 1 mN, an initial strain of 0.4%, and a strain rate of $1\%{\cdot}s^{-1}$ of the gauge length.

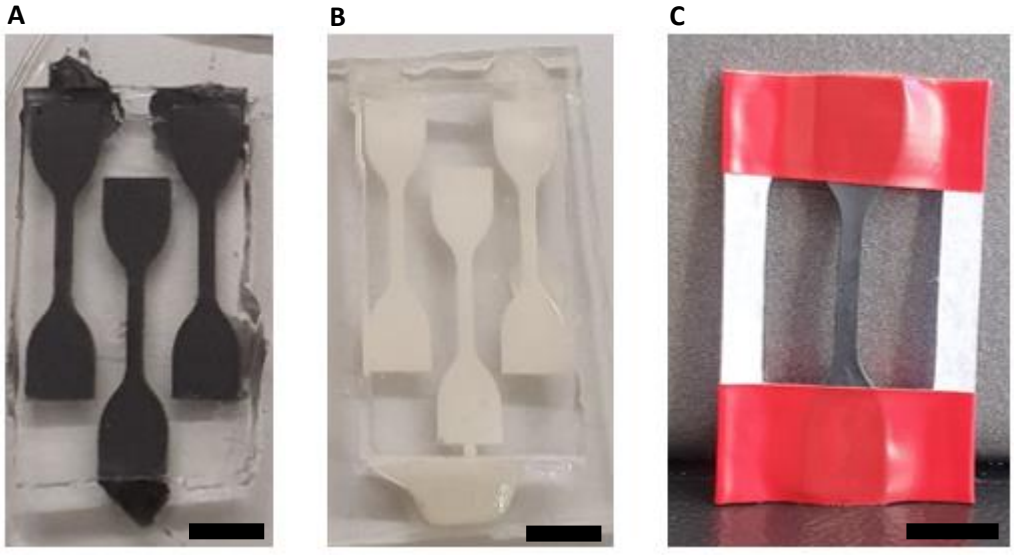

Figure 4.10 | PGSA samples. (**A**) PGSA composite samples in their PDMS molds. (**B**) PGSA samples in their PDMS molds. (**C**) PGSA composite dumbbell-shaped sample in a paper frame. Scale bars are 10 mm.

4.3.2 Degradation Properties

The aim of the final device is to be used inside the anterior chamber of the eye during cataract surgery, which typically does not last longer than 20 minutes in total. However, since the present study focuses on biodegradable elastomers for the fabrication of the soft actuators, a degradation assay was performed to investigate the degradation properties of the synthesized PGSA.

PGSA samples, as described for the tensile tests, were used for this degradation assay. After washing in ethanol and soaking in PBS, samples were oven-dried for 24 hours at 60 °C. Dried samples were placed in a plastic frame that supports the samples inside a PBS solution, thereby preventing them from sticking to any surface (see fig. 4.11). Simultaneously, this plastic frame supports the samples for tensile testing afterward to study the influence of the degradation on the mechanical properties.

Degradation protocol

Samples are tested on day one, and degraded samples are extracted from the PBS solution once a week for three consecutive weeks to perform tensile tests as described in section 4.3.1. The pH values were measured every seven days, and PBS would be replaced if the pH showed any alterations. Degraded samples are dried at 60 °C for 24 hours before weighing and testing.

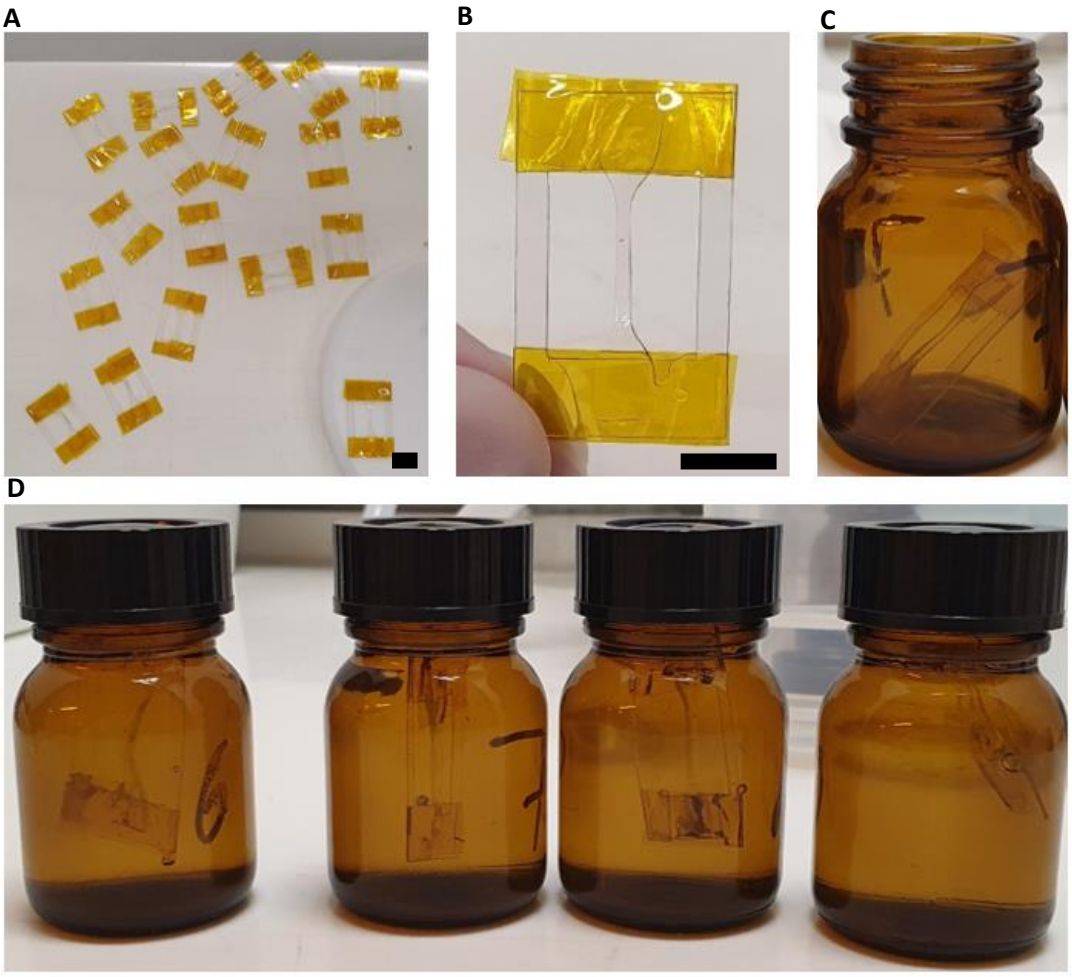

Figure 4.11 | 3D printed PGSA degradation samples. (**A**) Several degradation samples before being subjected to the degradation assay. (**B**) Close-up of a sample attached to a plastic frame with polyamide tape. (**C**) Plastic frames prevent the sample from sticking to any surface inside the glass vial. (**D**) Degradation samples suspended in a PBS solution. Scale bars are 10 mm.

Degradation of photocured PGSA in PBS occurs in an incubator at 37 °C. The plastic material was previously subjected to a degradation assay of its own for one week to verify that it would not influence the degradation assay. Weight and pH values were measured before and after placing the plastic inside a cleaned 50 mL glass vial with PBS. After oven-drying the samples at 60 °C overnight, the weight and pH values remained unchanged.

Accelerated degradation study

According to previous works on PGSA, degradation of PGSA in PBS solutions is extremely slow and only shows significant mass loss in a short period when exposed to enzymatic degradation in lipase solutions. Based on these studies, it is also evident that there is a discrepancy between the in vitro and in vivo degradation of PGS, which fully degrades in 6 weeks in vivo, but only 15% in PBS in 10 weeks.[109] Despite this discrepancy, an in vitro degradation study of the different PGSA samples will provide data relative to the well-known in vivo degradation properties of the polymeric network present in PGS. Hence, an accelerated degradation assay is performed by means of in vitro hydrolysis in a sodium hydroxide (NaOH) solution to attain relative differences for in vitro degradation of PGSA. NaOH promotes hydrolysis, the chemical breakdown of the polymer due to a reaction with water molecules in polymers that contain ester groups. PGSA is such a polymer and will experience hydrolysis in a basic medium.

Square 5 mm x 5 mm PGSA samples were 3D printed with a thickness of 1 mm and were washed with ethanol for 24 hours. The same shape was also fabricated with PDMS molds following the methods described in sections 4.2.1 and 4.2.2 to investigate differences in degradation properties between the two fabrication methods. All samples were then dried overnight in an oven at 60 °C. After weighing the samples, they were incubated in a 0.1 mM NaOH (Sigma-Aldrich, cat. no. 30620-M) solution at 37 °C in an incubator. 8 mg of 50 wt% NaOH pellets were dissolved in 1000 mL demineralized (demi) water to achieve a basic solution which was then poured into 22 ml glass vials where the samples were placed afterward. After different time intervals, samples were extracted, washed, and dried at 60 °C before measuring the net mass loss.

4.3.3 Gel Permeation Chromatography

The molecular weight distributions of PGS and PGSA were acquired using gel permeation chromatography (GPC). A glass vial was used to dissolve 5 mg of the polymers in 1 mL of dimethylformamide (DMF). A syringe was used to inject 5 mg of polymer inside a glass vial, and a Sartorius micropipette was used to measure 1 mL of the solvent. A small magnetic stirrer was placed inside the mixture and left to stir overnight. Before placing the sample vials inside the device, the dissolved polymer samples were filtered using a syringe filter. The filtered mixture was transferred to new glass vials that were placed in the tray of the GPC, where 10 µL was injected as analyte.

GPC tests were performed on a UFLC Shimadzu LabSolutions GPC located at the applied sciences faculty. The device is calibrated for polymers using the American PMMA standard and is equipped with two detectors. A Shimadzu SPD-20A ultraviolet detector is designated as detector A and a Shimadzu RID-10A refractive index (RI) detector as detector B. The elution time was 15 minutes for both samples, and the wavelength of the UV detector was 315 nm.

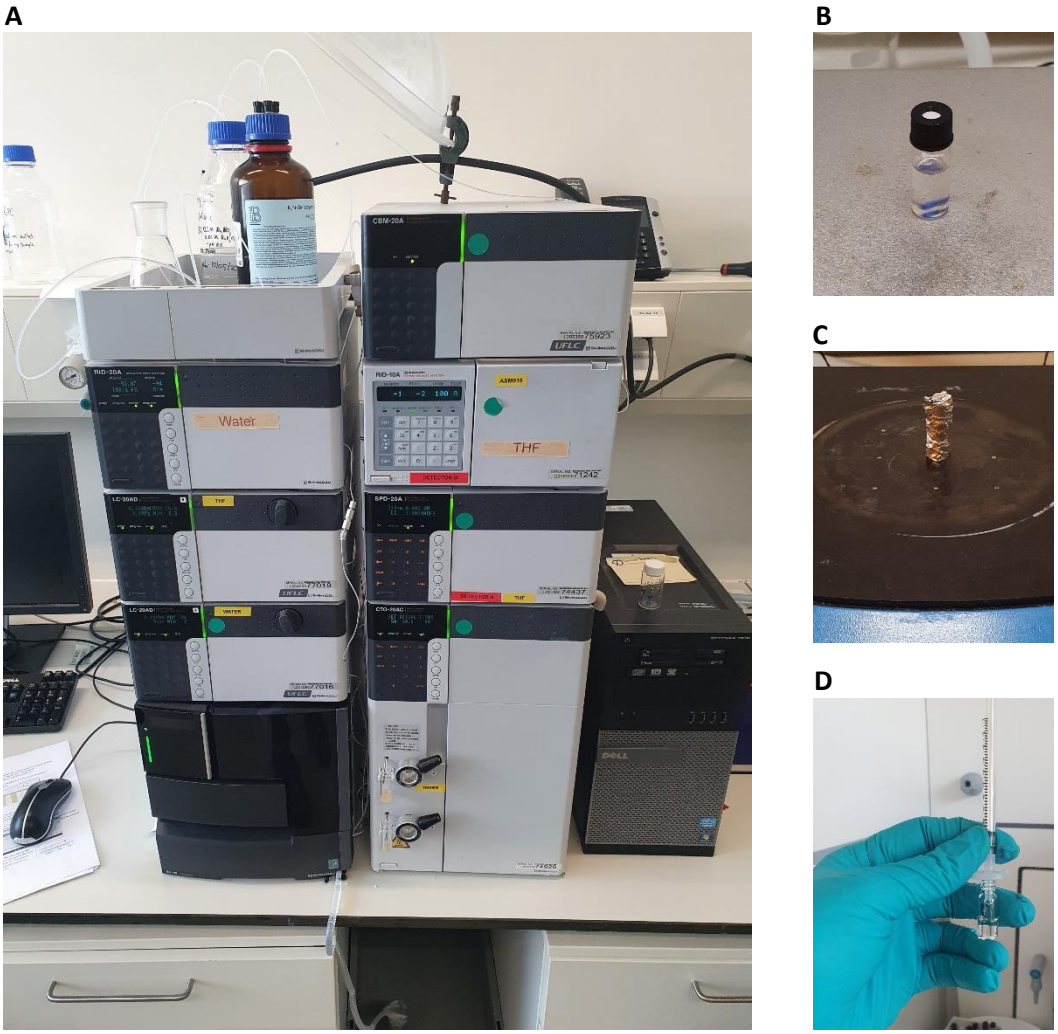

Figure 4.12 | Overview of the GPC experiment. (**A**) The GPC setup at the Applied Sciences Faculty (**B**) Glass vial containing PGS being dissolved in DMF with a small magnetic stir bar. (**C**) PGSA covered from light on a magnetic stirrer. (**D**) Filtration of the samples with a syringe filter before inserting the analyte into the device.

4.3.4 Swelling and Shrinking Properties

This thesis aims to utilize the synthesized materials in the anterior chamber of the eye to expand the iris. While the perceived device remains at the site of application for a limited amount of time, during fabrication, PGSA deals with swelling and shrinking mechanisms. PGSA experiences a high degree of swelling in ethanol which facilitates the removal of soluble content from the unreacted ink. In order to study the swelling and shrinkage of the materials synthesized in this work, square-shaped samples were prepared through 3D printing and PDMS molding (see fig. 4.13 A). These samples were placed in ethanol for 24 hours, after which weight and volume were measured. Subsequently, all samples were soaked in PBS for another 24 hours, and the same measurements were repeated once again to study the net mass and volumetric changes between the initial fabrication and the final structure.

Not only does this provide essential insights into the fabrication processes of these materials, but it also provides relevant information for other potential applications for which these versatile materials are interesting. The degree of swelling is very important for those applications that require extended in-vivo use or are required to operate in an aqueous environment.

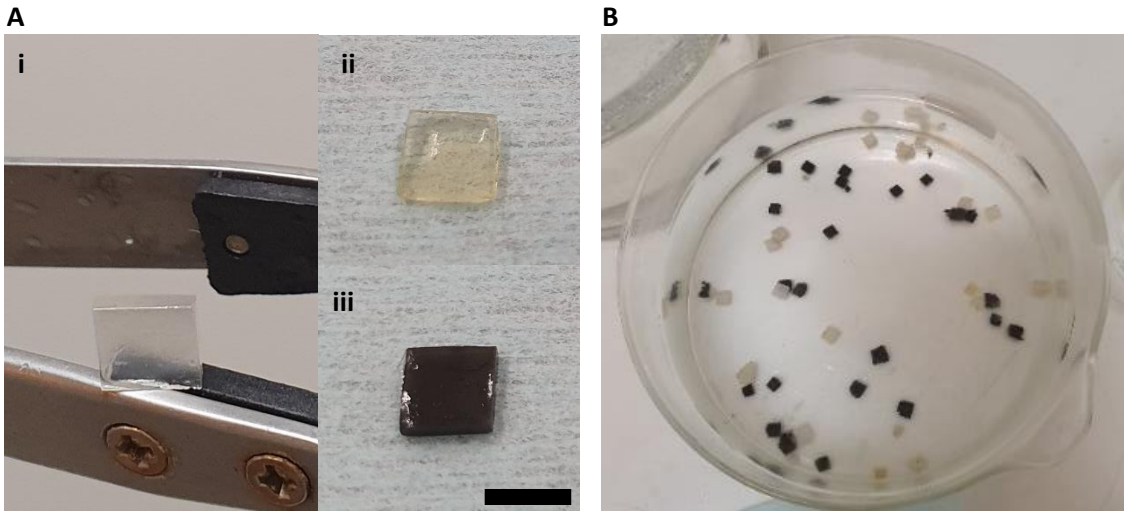

Figure 4.13 | PGSA samples for the accelerated degradation. (**A**) i, printed PGSA. ii, PGSAUV. iii, PGSAC. Scale bar is 5 mm. (**B**) PGSA samples in ethanol.

4.3.5 Hyperelastic Material Model Parameters Derived from Mechanical Properties

While numerous studies used finite element modeling for PGS, only a handful of previous studies used this method to simulate PGSA. Of those previous studies, only one mentions the use of curve fitting to determine the tensile modulus for a network structure of PGSA enhanced with polyethylene glycol diacrylate (PEGDA).[127] To achieve proper hyperelastic material parameters, tests should be performed under the same condition in which the material will be used. Since the main objective is to expand the pupil by radial stretching, data from the uniaxial tests are used to derive hyperelastic material model parameters. However, additional tests, such as a biaxial test, are recommended to achieve more reliable parameters. Due to the complete absence of any material model parameters, COMSOL Multiphysics was utilized to derive hyperelastic material model parameters for the different materials that were synthesized during this project based purely on uniaxial test results. A zero-dimensional model was set up in COMSOL, and by using the optimization interface, hyperelastic material model parameters were extracted for the Neo-Hookean and Mooney-Rivlin models. The stretch values required by the COMSOL model were calculated based on the strain of representative samples from each tested batch of materials.

4.4 Device Actuation

In this final section of the materials and methods, to achieve a demonstration of the concept, the actuation setups for the different types of prototypes are described.

4.4.1 Pneumatic Actuation Setup

A single channel autonomous pump, the Elveflow AF1 Series, capable of pressures between - 700 and 1000 mbar, was used to actuate printed PGSA device prototypes pneumatically. Different dispensing tip sizes were securely attached using a Luer lock connection, that in turn, is attached to an output channel via a plastic tube from the device to provide prototypes with pressurized air.

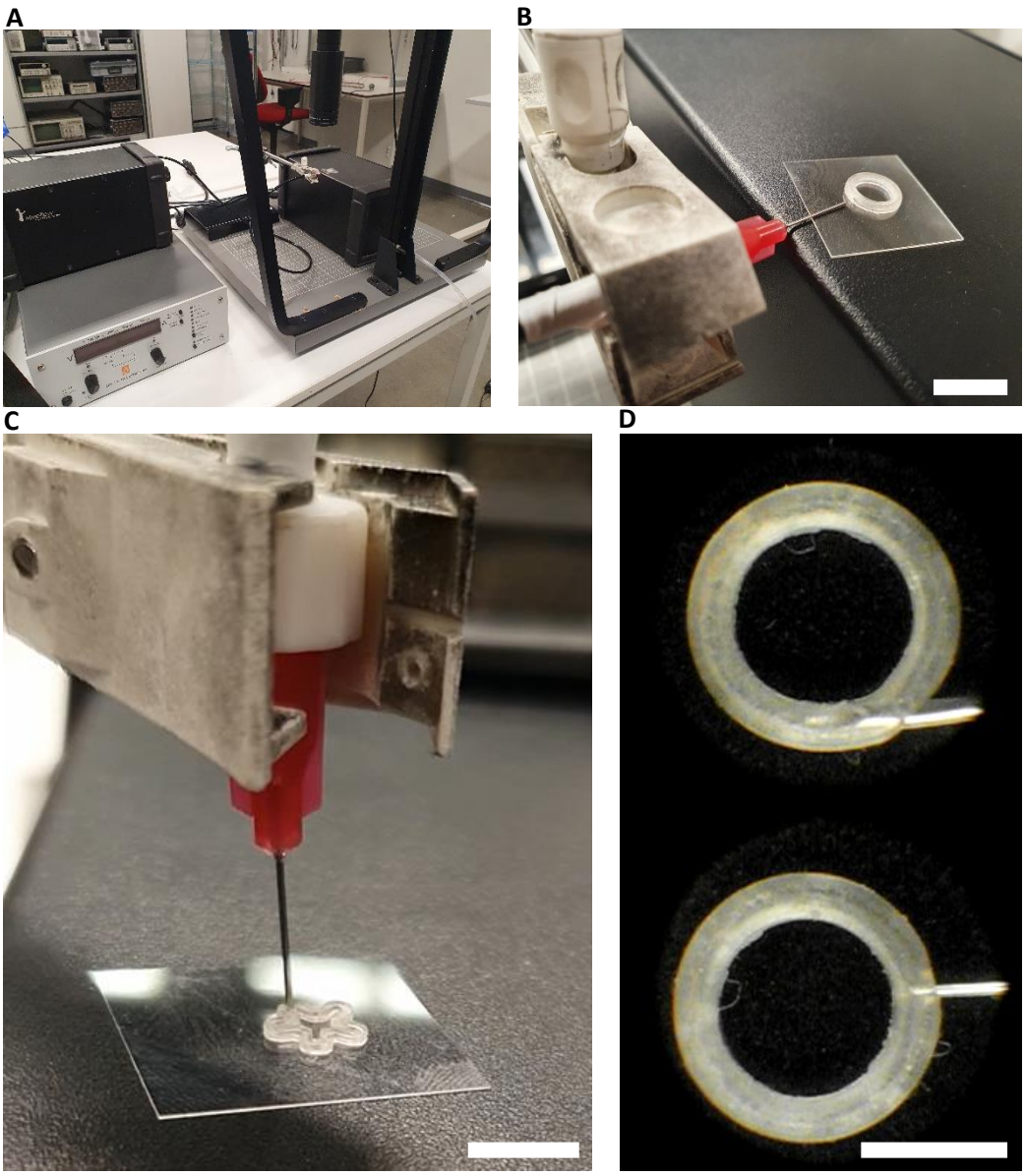

Figure 4.14 | Actuation setup with the pressure unit and the dispensing tip inserted into the prototype. (**A**) Overview of the setup. (**B**) Dispensing tip held horizontally for actuation through a laterally-printed inlet. Scale bar is 10 mm. (**C**) Dispensing tip held vertically for actuation through a top-sided printed inlet. Scale bar is 10 mm. (**D**) Different tip sizes are inserted through the printed orifice. Scale bar is 5 mm.

4.4.2 Magnetic Actuation Setup

Currently, 3D printed PGSA composite only possesses an arbitrary distribution of CIP particles. To showcase its magnetic properties, simple shapes were 3D printed and introduced in a DXSB-50 electromagnet via a glass rod with double stick tape on its tip to suspend the samples within the gap (see fig. 4.15). Magnetic actuation was attempted with both permanent magnets and an electromagnet.

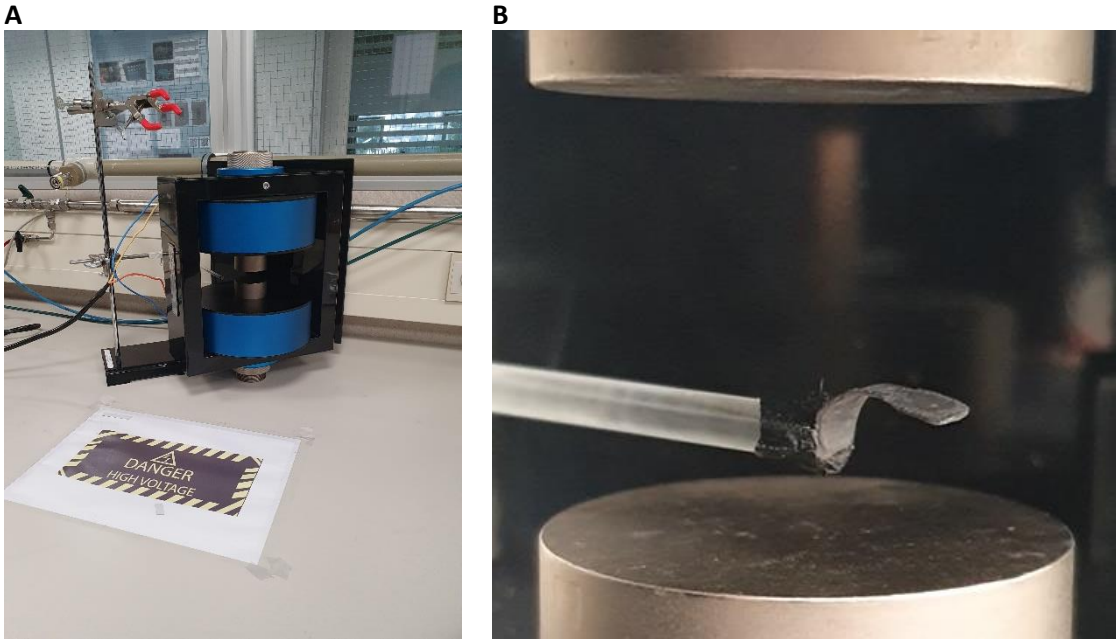

Figure 4.15 | Electromagnetic actuation setup. (**A**) DXSB-50 electromagnet from Xiamen Dexing Tech. (**B**) A 3D printed PGSA composite sample is attached to a glass rod in the magnetic gap. Scale bar is 10 mm.

To demonstrate the possibility of magnetic actuation with the synthesized materials, PGSA composite dumbbell shapes and device prototypes, fabricated by means of PDMS molds as described in sections 4.2.1 and 4.2.2, were also actuated using the aforementioned electromagnet. Here the different magnetic particle alignments will allow for more sophisticated motions compared with 3D printed PGSA composite.

5 Results

This chapter presents the results of the synthesis of the polymers, their properties, and their actuation capabilities. The synthesized materials are highlighted in the first section, followed by section 5.2, which presents the fabricated device prototypes. Then, the results of the characterization of the synthesized materials are discussed in section 5.3. Finally, the achieved actuations with the device prototypes from section 5.2 are presented in section 5.4.

5.1 Synthesized Materials

In this thesis, three different polymers were successfully synthesized.

5.1.1 PGS

Different PGS batches were synthesized, with the difference being only the polymerization duration. All PGS was allowed to polymerize for 2 hours in a nitrogen environment at 120 °C. Then, in a vacuum oven, different time ranges between 22 and 94 hours were used to synthesize PGS with different degrees of cross-linking. After the polycondensation reaction, a viscous, yellowish, and almost entirely transparent liquid was obtained (see fig. 5.1). By altering the duration of cross-linking, two main PGS prepolymer batches were synthesized to use for the fabrication of the device. PGS from polycondensation durations of 48 and 72 hours are denoted as PGS48 and PGS72. Other durations led to PGS variations that were not useful for further application during this thesis.

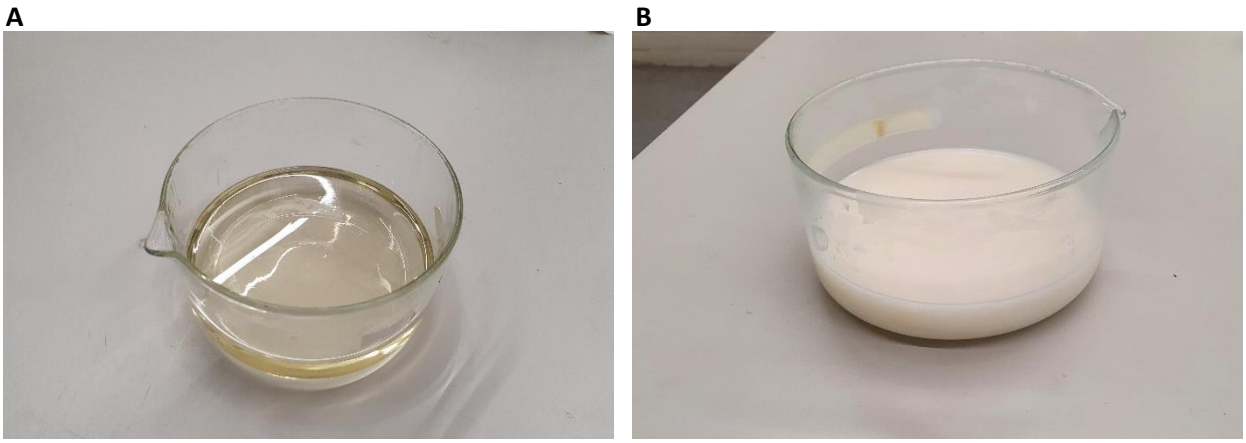

Figure 5.1 | PGS prepolymer. (**A**) After cross-linking for 72 hours, PGS turns into a viscous and transparent liquid. (**B**) PGS, when cooled down, becomes white and solid.

PGS72 was used to make thin films of approximately 1.5 mm by dispensing PGS prepolymer in glass Petri dishes. In this work, fabrication with PGS was limited to thermal curing, where it was possible to achieve different material properties by altering the duration of thermal curing of PGS that was allowed to cross-link for 72 hours (see fig. 5.2).

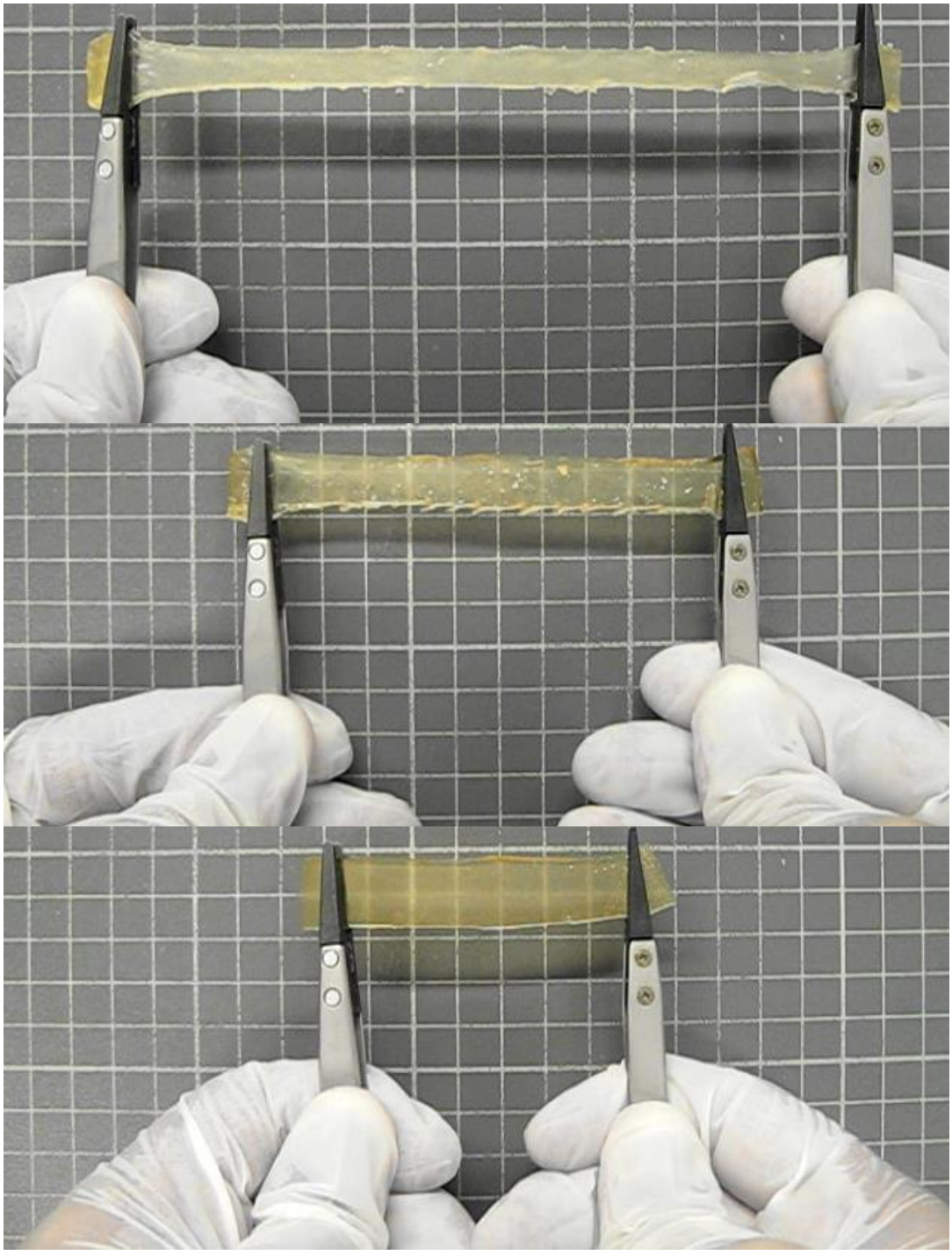

Figure 5.2 | Qualitative comparison of the stretchability of PGS30, PGS40, and PGS48 (from top to bottom). Samples that initially have the same dimensions displayed great variation in stretchability when manually stretched with a similar force to show qualitative differences in material properties. The different PGS samples were all fabricated from PGS that was cross-linked for 72 hours. The squares are 1 cm. PGS30,40,48 corresponds to 30, 40, 48 hours of thermal curing.

5.1.2 PGSA

PGSA of different degrees of acrylation was successfully synthesized using the modified synthesis process described in appendix A. Acryloyl chloride was used in ratios varying between 0.3 mol/mol to 0.6 mol/mol of hydroxyl groups present in PGS. The exact degree of acrylation can be calculated using the different proton peaks obtained from proton nuclear magnetic resonance (H NMR) spectroscopy. Since such measurements could not be performed within the confinements of this thesis, the degrees of acrylation are approximated from previously published works and are based purely on the molar ratios acryloyl chloride was added to PGS prepolymer.[121] Degrees of acrylation of approximately 17, 23,29, and 35% were tested for further application as inks.

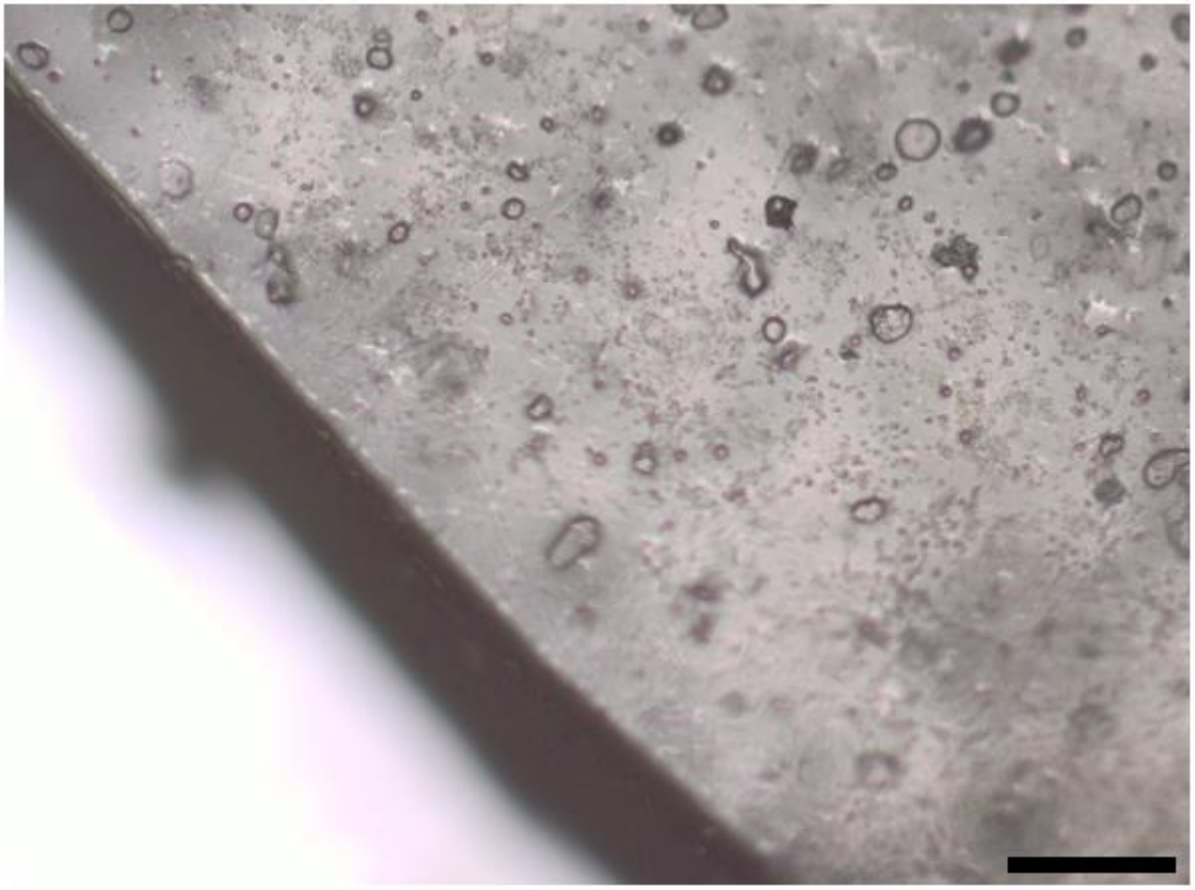

Figure 5.3 | Surface morphology of demolded PGSA. Scale bar is 200 µm.

5.1.3 PGSA Inks

PGSA inks from varying degrees of acrylation were synthesized by adding TPO to the prepolymer. Not only DMSO and EGBEA but also ethyl acetate was able to adjust the viscosity of the PGSA ink to a compatible range for use with the Asiga Max X and did not seem to influence the ink quality in any negative way. In the limited time span that the inks were available during this thesis, the inks maintained similar characteristics in all the solvents used to dilute the inks.

PGSA inks from all the degrees of acrylation were tested with different ratios of the diluents EGBEA/DMSO. In total, 14 different inks were tested with the Asiga printer, which resulted in two successful inks ratios that were compatible with the printer.

PGSA inks with degrees of acrylation of 17% (PGSA17) and 29% (PGSA29) were used in the remainder of this work to print PGSA structures. 80 wt% PGSA17 was diluted in DMSO/EGBEA to achieve a compatible ink for this degree of acrylation. 95 wt% PGSA29 was diluted with DMSO/EGBEA as a higher degree of acrylation resulted in a lower density material (see table 5.1). This decrease in density with an increasing degree of acrylation is in accordance with previously published works on polymers.[109,128,129] It can be explained due to the fact that the acrylation of the polyester bonds of glycerol in PGS causes these chains to become longer, in turn causing them to occupy more space. Therefore, the total free volume between these acrylated chains in the elastomer network also expands, causing the density to decrease. Based on this principle, a higher degree of acrylation with a similar amount of starting prepolymer should result in a higher volume of acrylated PGS. However, this was not focused on during the synthesis of the PGSA batches in this work.

Material	Density (g/cm^3)
PGSA17	1.07 {0.019}
PGSA23	1.18 {0.041}
PGSA29	1.35 {0.038}
PGSAC	2.14 {0.033}

Table 5.1 | Ink densities of PGSA measured at 40 °C. Values are reported as the mean, followed by the standard deviation in braces. PGSA17, 23, 29 corresponds to 17, 23, 29 % acrylation of PGSA. PGSAC corresponds to PGSA composite.

PGSA composite inks with two different iron powders were synthesized and tested for printing with the undisclosed modified protocol from Asiga. PGSA23 with 20 wt% and 50 wt% CIP, whilst stirring at 80 °C for 10 minutes, resulted in the best all-around ink compared to mixtures with other degrees of acrylation or with iron(III) oxide powder. Stirring the mixture at a higher temperature caused the PGSA to start curing, which was indicated by an increase in viscosity which could be felt with the lab spoon. No additional benefits were noticed for stirring the mixture longer than 10 minutes. Since adding CIP to the elastomer makes it less compliant, it followed that a high degree of acrylation was more suitable as a PGSA composite ink. After further testing, 20 wt% CIP proved to possess the ability for faster photocuring and had a better affinity for achieving reasonable resolutions and softer

outcomes. PGSA23 was therefore mixed with micro-sized biodegradable carbonyl iron powder (CIP) to achieve a fully biodegradable polymeric composite ink that maintains its magnetic properties after being DLP 3D printed.

PGSA ink remained printable as long as sufficient ink was present in the Asiga build tray, which required a minimum of approximately 20 -30 mL of PGSA before prints started to fail. One batch of PGSA ink remained printable after spending almost two months in the fridge. PGSA composite ink was not available for a prolonged period. However, after being stored in a fridge at 4 °C for three weeks, it showed stiff fragmented pieces that appeared as cracks (Fig. 5.4 A). Despite the cracks, both the PGSA and PGSA composite inks were able to be printed again by heating the entire build tray to 40 °C and stirring the ink with an Asiga spatula that prevents the bottom of the build tray from getting damaged.

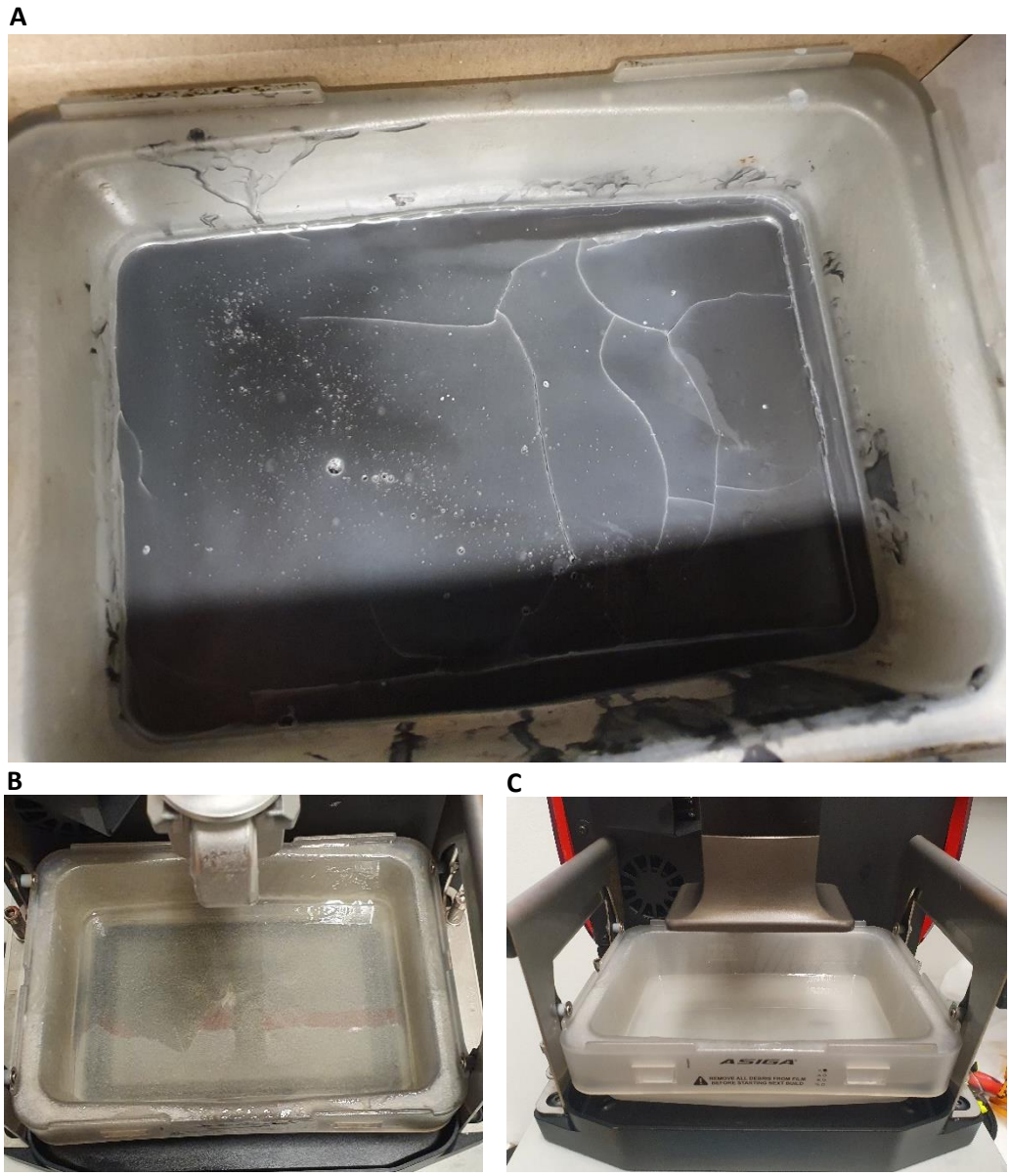

Figure 5.4 | PGSA inks. (**A**) PGSA composite ink showing signs of what appears to be crazing (**B**) PGSA17 ink batch. (**C**) PGSA29 ink batch.

5.2 Fabricated Devices

In this thesis, prototypes of the device were fabricated through different methods. Both 3D printing and molding were used to achieve different shapes and sizes of the final device.

5.2.1 Fabricated Soft Actuator with PGS Molding

PGS from different batches was injected into PDMS molds with PDMS, and other materials, as substrates. After silanization, PDMS, glass, silicon wafers, and Teflon were used as substrates. PGS had to be heated up to at least 70 °C on a hot plate or in an oven to flow through the syringe and dispensing tip used to inject the molds, and the plunger was used to aspirate the viscous PGS into the needle. The plunger was used to insert the viscous PGS into the needle. Before injection, the molds and substrates were bound together using polyamide tape, which can withstand high temperatures during thermal cross-linking (see fig. 5.5 A).

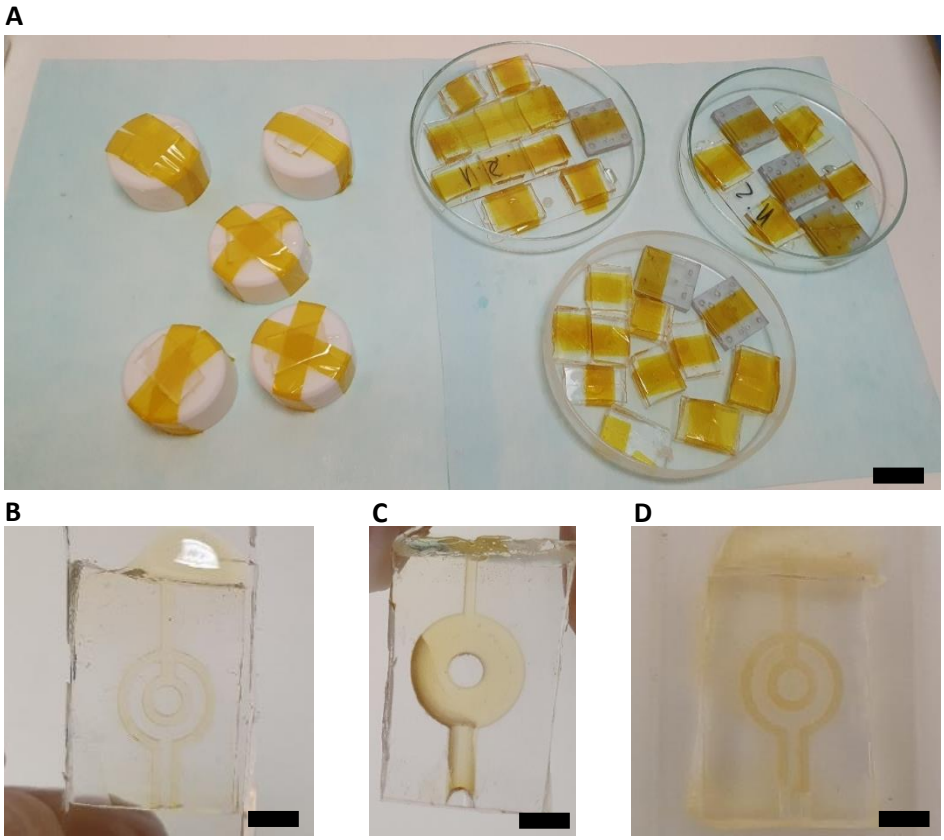

Figure 5.5 | Thermally cured PGS samples in PDMS molds. (**A**) Overview of different substrates for PDMS molds. Scale bar is 20 mm. (**B**) The middle part of the device in a PDMS mold on a PDMS substrate. Scale bar is 5 mm. (**C**) The outer part of the device in a PDMS mold with the substrate removed. Scale bar is 5 mm. (**D**) The middle part of the device in a PDMS mold on a glass substrate. Scale bar is 5 mm.

Despite silanization of the PDMS mold and the different substrates, it was only possible to fully demold the PGS after prolonged cross-linking. PDMS molds on a Teflon or PDMS substrate showed the most potential for successfully assembling a device. It was clear that PGS48 had to be thermally cured for at least 36 hours to be potentially demoldable. Hence, multiple samples were thermally cured at once for 36 hours. Subsequently, a sample would be taken out every hour to check their ability to be demolded. After demolding, PGS cured for 46 hours proved to possess the best balance between stiffness and elasticity (see fig. 5.6).

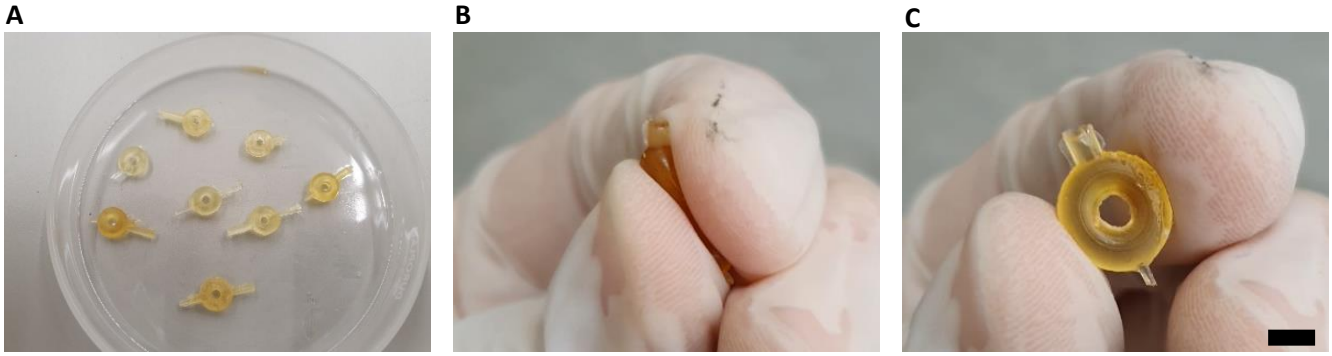

Figure 5.6 | Fabricated PGS samples. (**A**) some of the samples that were demolded and stacked on top of each other. (**B**) Squeezing of a sample. (**C**) Samples were all able to regain their shape after being fully compressed. Scale bar is 5 mm.

While most demoldable PGS parts were too brittle and stiff, PGS48 demolded at 46 hours of thermal curing proved to be useful. However, with this degree of curing, stacked samples were not able to be cured together, they only managed to become stiffer due to further cross-linking but did not join together. Uncured PGS was added to facilitate this process. Still, the features of the middle layer were too small to be able to cure between the top and bottom parts. While a larger device could possibly solve this issue, the actual device would be required to be even smaller than what was experimented with.

Finally, an attempt was made to fabricate the device with only two parts by designing a new shape fusing the middle and one outer layer into one (see fig. 5.7). However, this made the demolding much more difficult for the new larger part of the device.

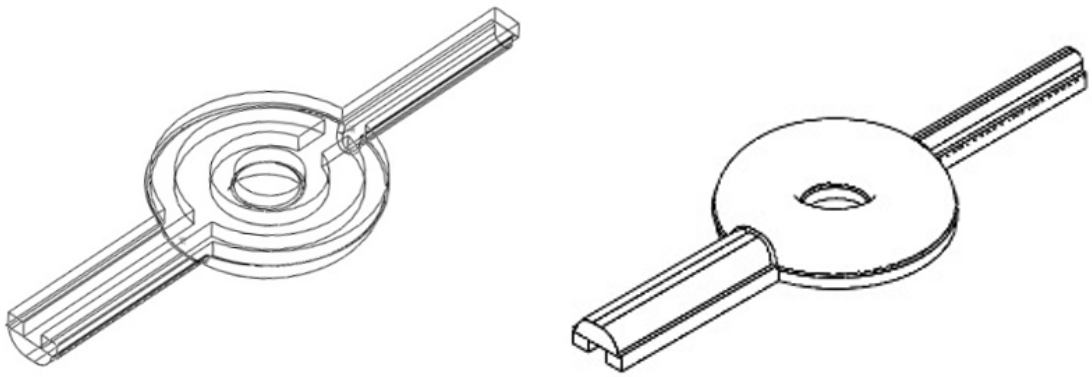

Figure 5.7 | Adjusted mold consistent of two layers instead of three. Top and bottom isometric views.

The PGS device parts that were demoldable could not be stacked together because of the inability to demold them at an earlier stage (see fig. 5.8). Adding uncured PGS in between layers also did not improve the ability to stack the different parts on top of each other.

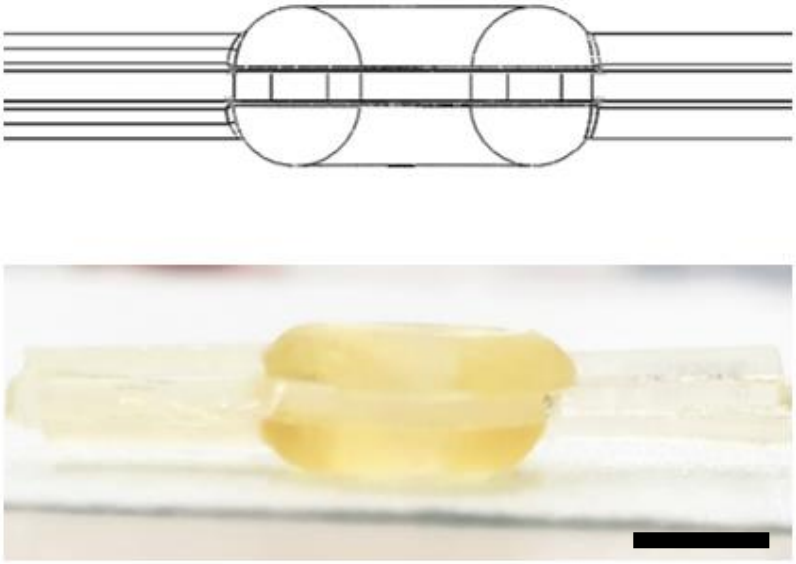

Figure 5.8 | Stacked layers. Design and realized sample. Scale bar is 5 mm.

5.2.2 Fabricated Soft Actuator with PGSA Magnetic Composite Molding

PDMS molds, similar to those used for PGS but lacking a channel, as well as a smaller variant, were injected with PGSA composite to achieve a ring-shaped device that would expand when a magnetic field is generated. The PGSA composite ink was UV cured for durations typically between 15 and 20 minutes.

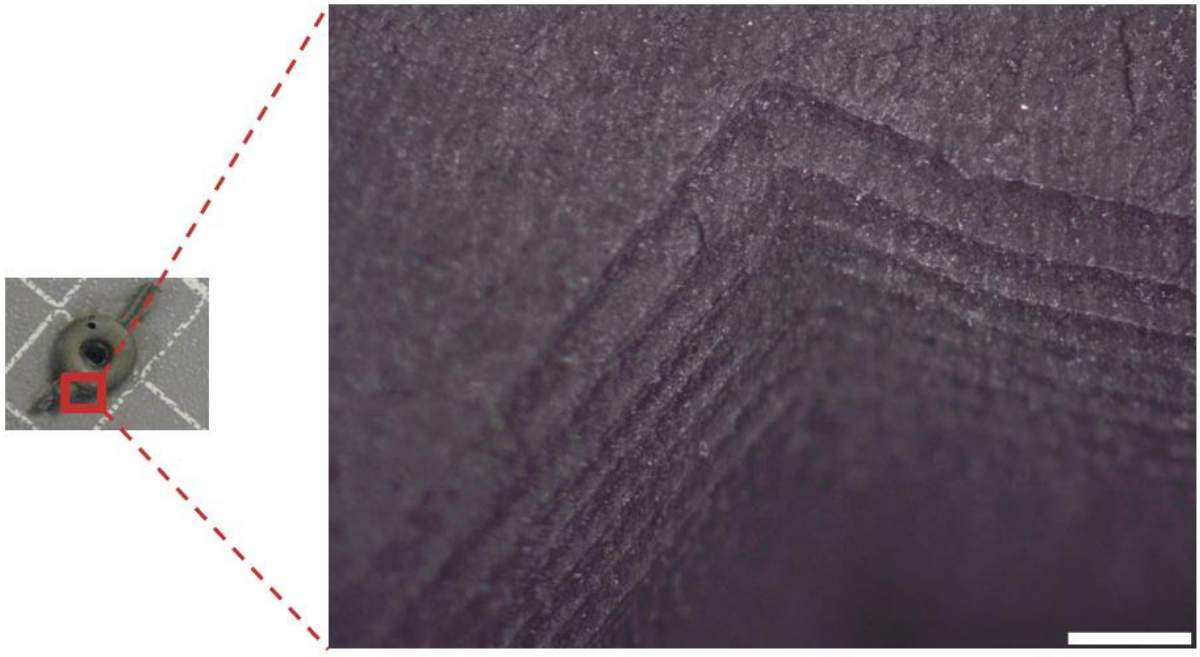

Figure 5.9 | PGSA composite ring. The visible layers are remnants from the circular-shaped parts of the 3D printed molds. Scale bar is 200 µm.

Contrary to PGS, the PGSA composite was easily demoldable, and the material was not sticky thanks to the iron particles, making its manipulation easier.

5.2.3 Fabricated Soft Actuator with 3D Printed PGSA

After deriving the printer settings, PGSA ink was used to print different structures, ranging from simple dumbbell shapes used for tensile tests to complex hollow structures that function as a prototype for the final device (see fig 5.10).

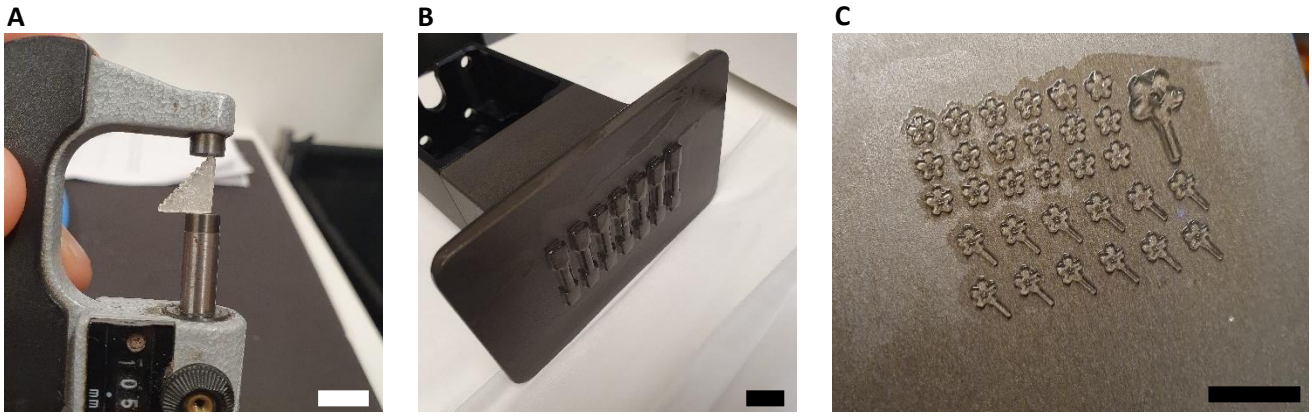

Figure 5.10 | 3D printed PGSA structures. (**A**) A small test structure for determining some of the printer settings. (**B**) PGSA dumbbell-shaped samples for the purpose of performing tensile tests. (**C**) Rim-like device prototypes with and without inlet channels for pneumatic actuation. Scale bar are 10 mm.

With the achieved fully compliant prints, the aim of fabricating a soft device was very successful. The goal with both the material and the printer settings was to achieve such a composition of the final device. This caused the device to be very soft but, therefore, very difficult to manipulate. Another issue with 3D printed devices that are meant for pneumatic actuation and possess a fluidic chamber inside is that due to the mechanism behind 3D printing, the channel will always be filled with uncured ink. In this case, PGSA ink occupies the complete internal structure of the fabricated devices, and when the device is exposed to the outside environment, it could cause the uncured ink to photopolymerize and block the channel indefinitely. For both the issues described above, the solution is to submerge new prints in ethanol, followed by soaking them in PBS. Ethanol causes the print to swell due to uptake into the photocured PGSA and aids in washing the prints from uncured ink. 2-propanol (IPA) is also an option to wash new prints, but it tends to destroy them after minimal exposure due to the very thin walls of the print. For the millimeter-sized devices that were printed, it takes approximately 2 - 4 hours to wash off the uncured resin. Samples were then immediately placed in a PBS solution, in which the photocured PGSA floats to the surface. This is caused by a decrease in density of the sample due to ethanol (0.79 $g \cdot cm^{-3}$) uptake, which has a lower density than PBS (~1 $g \cdot cm^{-3}$). After soaking in PBS for another 2-4 hours, the prints become very amenable and are considerably less sticky. More details regarding the effects of these postprocessing steps are presented in section 5.3.5.

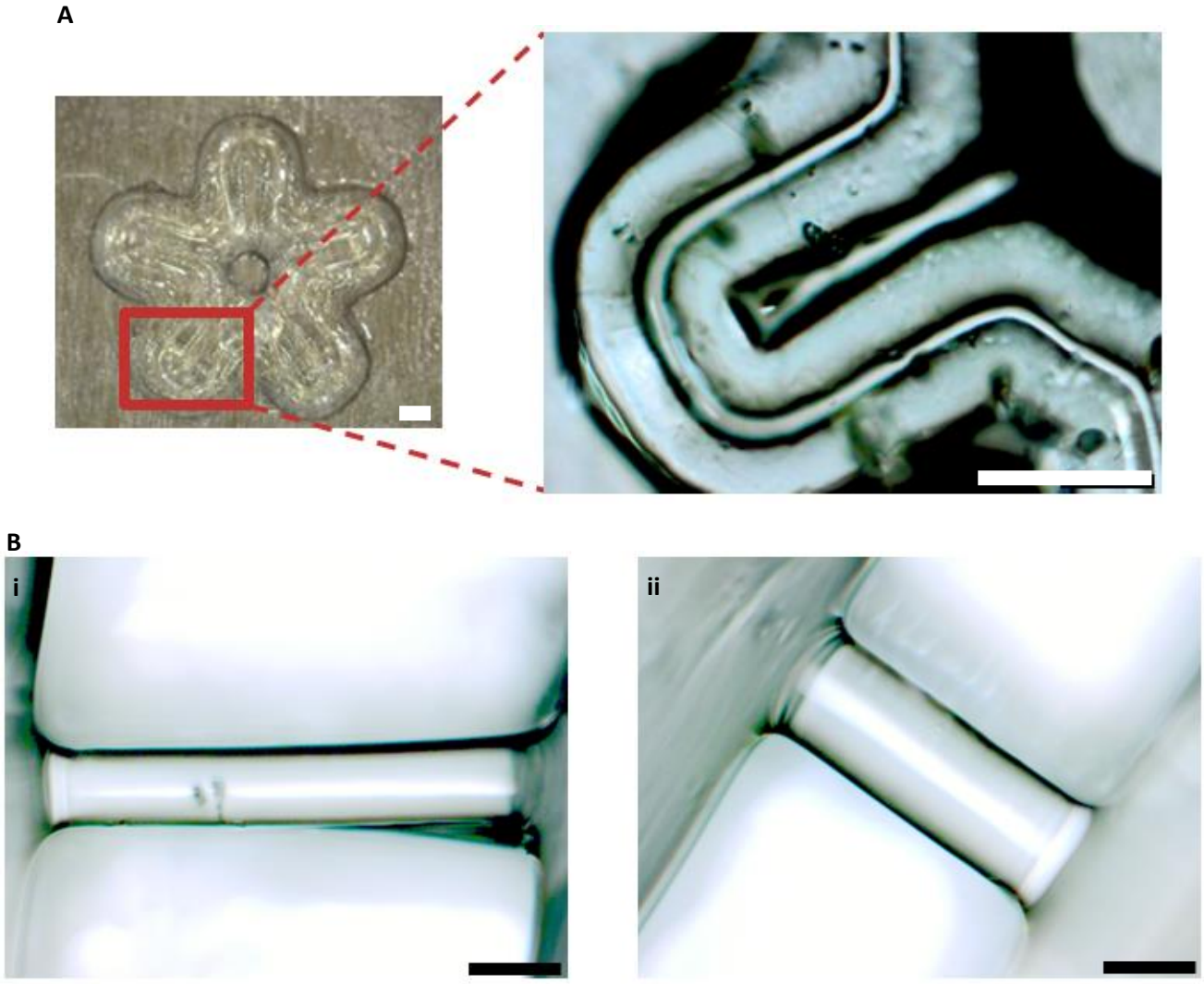

Figure 5.11 | Achievable prints. (**A**) A rim-like device with a fluidic channel meant for actuation and an exploded view of the internal channel. Scale bars are 200 µm. (**B**) Suspended beam structures 3D printed with PGSA17. The beam is suspended between two walls. i, The beam spans 640 µm with a diameter of 89 µm. ii, The beam spans 420 µm with a diameter of 140 µm. Scale bars are 100 µm.

Not only the circular design with a thicker outer and thinner inner wall and the rim-like shape were achieved with 3D printing (see fig. 5.11 A). The combination of CAD software and the Asiga Max X with the correct printer settings proved to be a powerful tool in fabricating fluidic elastomeric devices. Different prototypes with very defined features on a micrometer scale were fabricated using the printer. Micrometer scale features are possible without any postprocessing, where it was possible to print freestanding feature sizes of around 90 µm (see fig. 5.11 B). With the LED pixel size of 27 µm, this entails that PGSA ink is printable with a width of three pixels only. No postprocessing was performed on the samples used to showcase the feature size, which could be decreased even further by exposure to certain solvents. Microscopic images featuring device prototype structures are presented in figure 5.12.

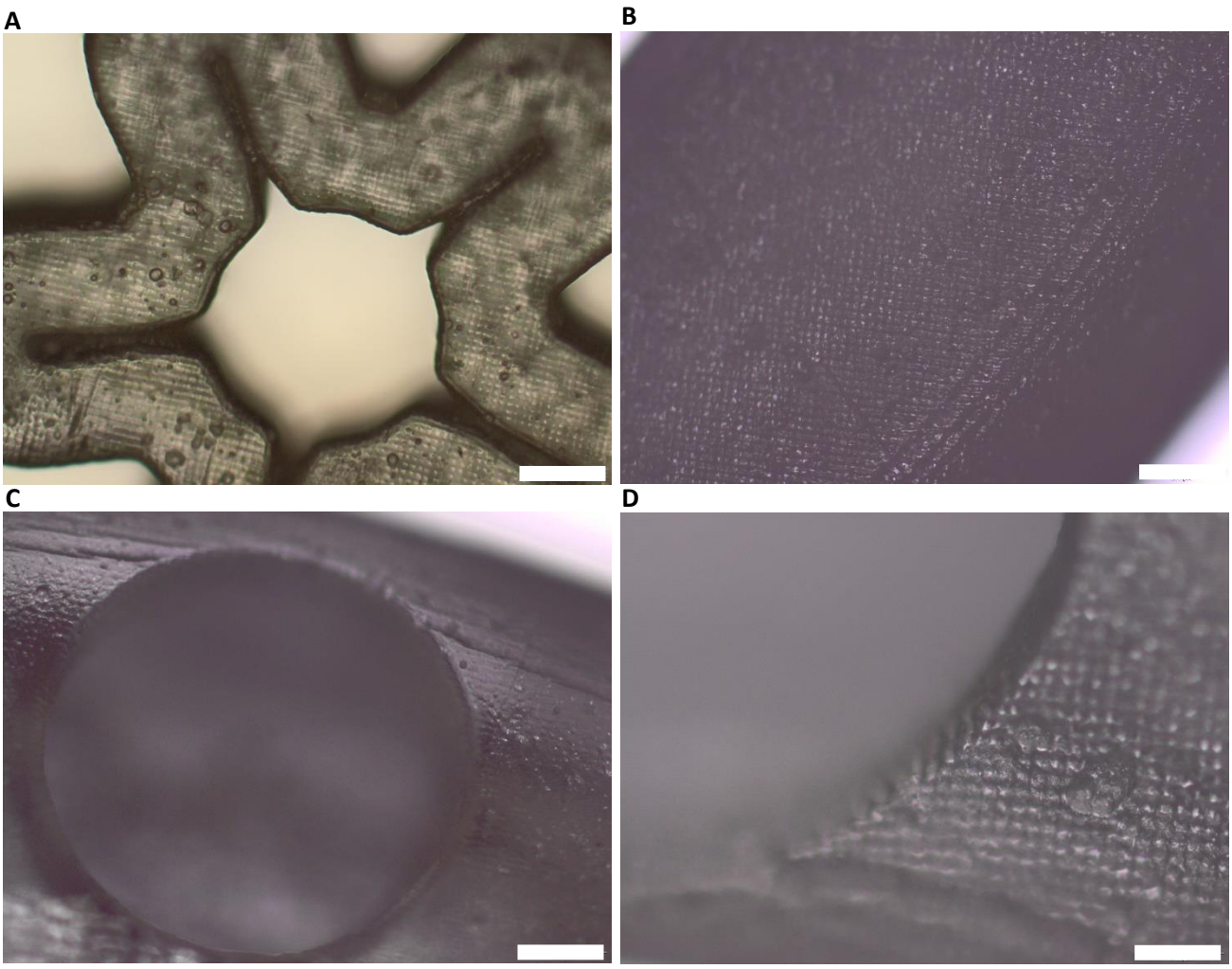

Figure 5.12 | 3D printed prototypes. (**A**) A device prototype with an outer diameter of approximately 1.6 mm containing an opening for a dispensing tip and an internal hollow channel. Scale bar is 200 µm (**B**) Tilted view of the filleted corners showing the resulting layered structure of the 3D printed device. Scale bar is 200 µm. (**C**) Close up of the inlet in a ring-shaped prototype. Scale bar is 200 µm. (**D**) A close-up displaying the achieved feature definition of a circular opening. The grid-like structure on the surface of the device is an artifact of the individual LED pixels of 27 µm. Scale bar is 100 µm.

Following the described steps for mixing CIP with PGSA, the best results followed from adding 20 wt% CIP to PGSA23, increasing the temperature to 80 °C, and manually stirring the mixture for 10 minutes. It was also not necessary to introduce additional concentrations of TPO to the ink. Printer settings were adjusted to manage printing the fully opaque material (see fig. 5.13). While printing with the same slice thickness as PGSA ink, it takes approximately 50-60% more time to complete a print of the same build height. Nonetheless, printing this material is exceedingly fast compared with the PGSA composite demolding with PDMS. Moreover, it also allows faster prototyping and more complex shapes to be realized. While the ring-shaped prototypes seemingly remained sufficiently soft for actuation purposes, they were also noticeably easier to manipulate after printing. These devices also do not possess a hollow internal channel. Therefore, the postprocessing steps of washing and soaking in ethanol and PBS, respectively, were not necessary in this case. Meaning that while the printing process itself takes longer, there is no need for additional operations afterward.

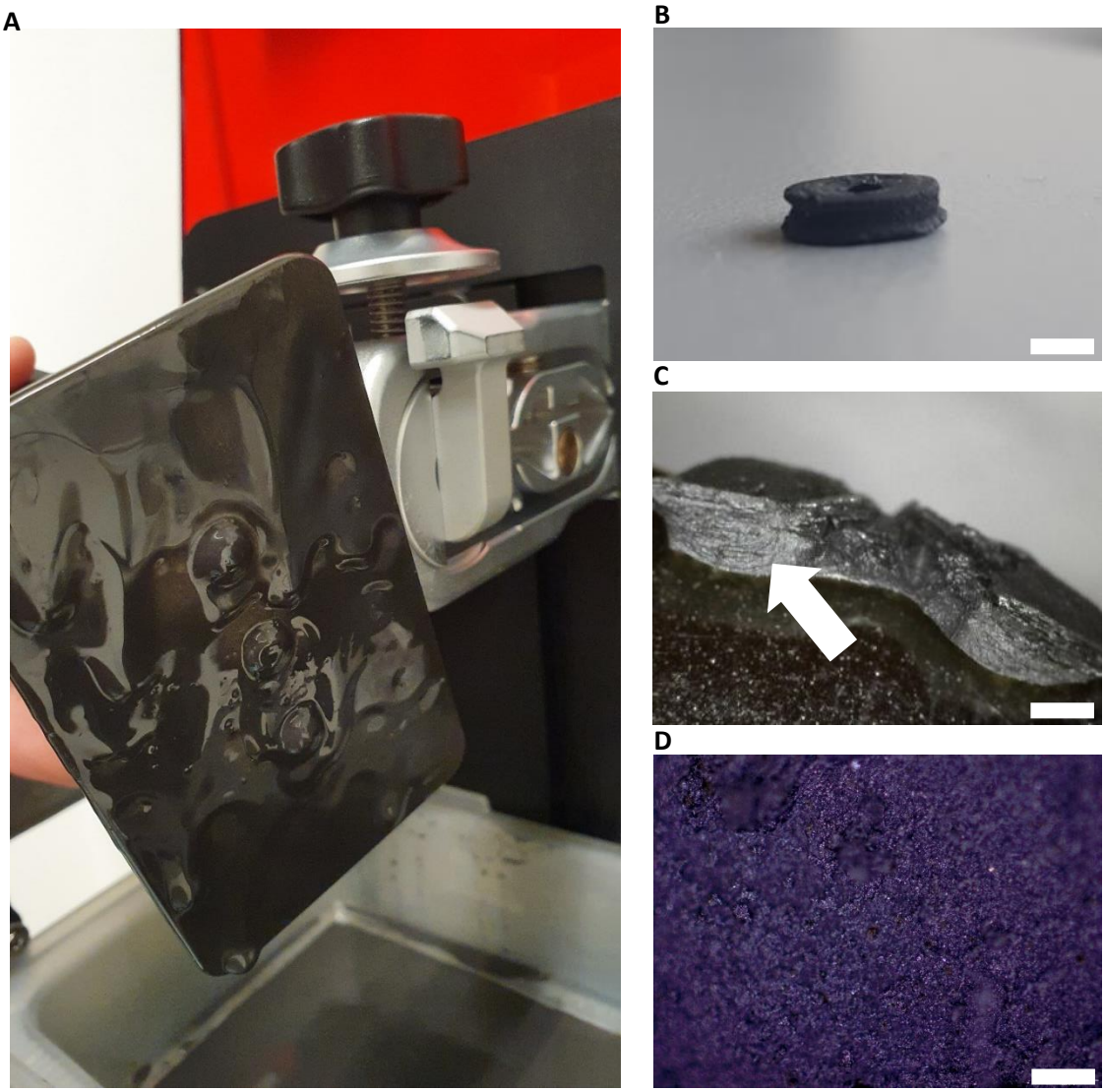

Figure 5.13 | 3D printed PGSA composite. (**A**) 3D prints still attached to the build platform. (**B**) A PGSA composite ring-shaped prototype. Scale bar is 2 mm (**C**) Cross-section of the printed PGSA composite rings displaying the layered internal structure due to additive manufacturing. Scale bar is 1 mm (**D**) Surface morphology of the printed PGSA composite. Scale bar is 100 µm.

It is noteworthy that the different PGSA composite prints not only showed good feature definitions, but also maintained their magnetic properties. However, it must be noted that these structures, different from their demolded counterparts, do not possess any particular magnetic particle alignment as of yet.

With the synthesized inks, it is possible to alter the mechanical and chemical properties with UV or thermal postprocessing. More details are found in section 5.3.2 regarding the mechanical properties. UV-curing was attempted with an Otoflash G171 post-curing unit and the Philips UV lamp. However, both of these seemed to not have any effect on the mechanical properties indicating that radicals that form thanks to the 1 wt% TPO are only sufficient for the initial photocuring during printing. PGSA allows for two radical groups to form when TPO is added, but by increasing the mole fraction of TPO in the ink, it is theoretically possible for UV postprocessing to have a greater effect on printed structures. Thermal post-curing was also applied, resulting in a definite increase in the toughness of the material and a change of color from transparent yellowish to an opaque brown color.

5.3 Characterization of Materials

In this chapter, the acquired material properties for the synthesized materials are discussed in detail. First, the mechanical properties are presented in sections 5.3.1 and 5.3.2. Then, the degradation properties are discussed in section 5.3.3, followed by the results of the GPC measurements in section 5.3.4. The swelling and shrinking characteristics are discussed in section 5.3.5, and finally, the derived hyperelastic material model properties are presented in section 5.3.6.

5.3.1 Mechanical Properties of PGS

A soft and stretchable material is desired for the final application in this project. Hence the mechanical properties of PGS were investigated and are presented in this section. PGS72 was used to fabricate three flat PGS films by dispensing PGS prepolymer into glass Petri dishes that were thermally cured for 30, 40, and 48 hours. There is a clear contrast in color and textures between the three, with longer curing times corresponding to a darker color and a stiffer but less sticky material. The tensile modulus is determined based on strain values between 5 and 10%. Representative stress-strain curves from each tested batch are given in figure 5.14, while an overview of the tensile moduli is presented in table 5.2.

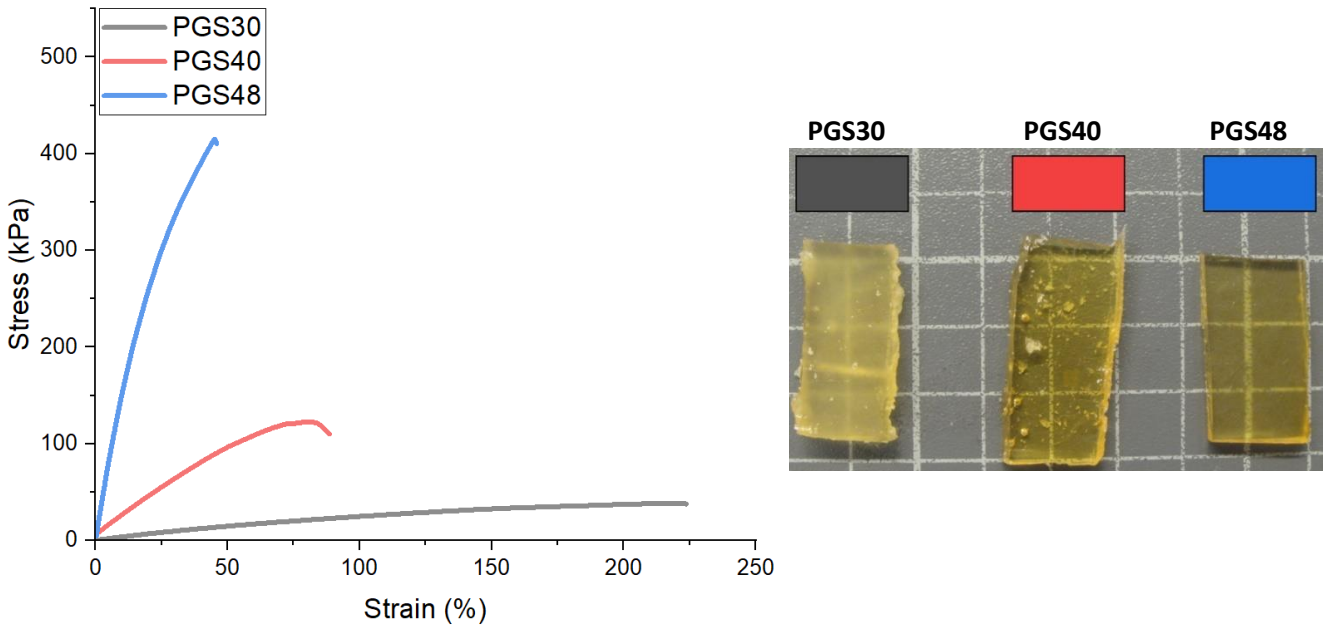

Figure 5.14 | Representative stress-strain curves of the three tested PGS samples. PGS30,40,48 corresponds to 30, 40, 48 hours of thermal curing.

Material	Tensile modulus (kPa)	Number of samples
PGS30	0.34 {0.08}	6
PGS40	3.15 {0.97}	6
PGS48	10.60 {2.24}	10

Table 5.2 | Measured tensile modulus for PGS samples. Values are reported as the mean, followed by the standard deviation in braces. PGS30,40,48 corresponds to 30, 40, 48 hours of thermal curing.

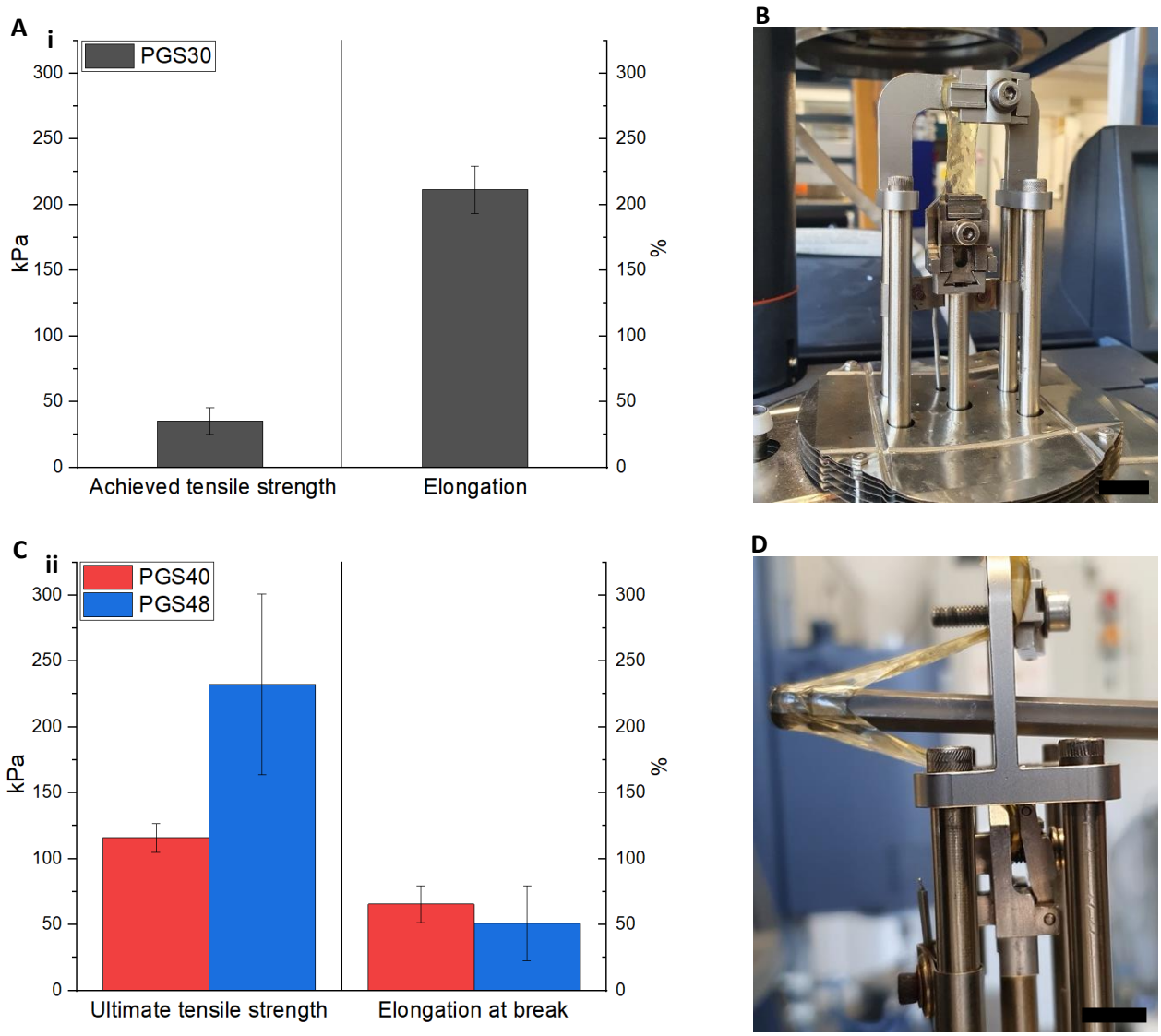

Figure 5.15 | Ultimate tensile strength and elongation of rectangular PGS samples. (**A**) Error bars represent the standard deviation of the mean. i, Bar plot representing the achieved elongation and tensile strength for PGS30. ii, Ultimate tensile strength and elongation of PGS40 and PGS48 that did reach failure. PGS30,40,48 corresponds to 30, 40, 48 hours of thermal curing. (**B**) PGS samples elongated in the DMA. (**C**) The smallest possible PGS30 samples that could be held by the clamps were all insufficiently elongated for them to reach failure. The samples required more elongation to reach failure. Scale bar is 10 mm.

There is a direct relationship between increased duration of curing and increased tensile modulus and tensile strength (see fig. 5.15 A). However, with increasing stiffness comes a decrease in elongation of the samples. For PGS30, the tensile strength is not representative as the DMA did not allow for further elongation of the samples. None of the 30 hours cured PGS samples were destroyed during tensile tests (see fig. 5.15 C).

5.3.2 Mechanical Properties of PGSA

For PGSA, paper frames were a helpful tool in dealing with the sticky material while also providing the clamps an increased surface area to hold onto. A universal paper frame could be used for slightly different sizes between the printed and demolded samples. More about this discrepancy in sizes is discussed in section 5.3.5. Table 5.3 summarizes all the relevant mechanical properties of the tested materials. The tensile modulus was determined based on the strains between 5 and 10%, and the total area under the curves was used to determine tensile toughness.

Material	Tensile modulus (kPa)	Ultimate tensile strength (kPa)	Elongation at break (%)	Tensile toughness (kj/m^{-3})	Number of samples
Printed PGSA29	2.44 {0.47}	112.18 {15.76}	74.89 {7.34}	26.67 {2.64}	3
Printed PGSA23	1.55 {0.13}	95.44 {6.26}	63.59 {3.93}	30.85 {5.42}	2
Printed PGSA17	1.23 {0.21}	53.29 {9.08}	39.23 {0.66}	15.15 {0.08}	4
PGSAUV 10 min	2.02 {0.30}	73.94 {18.58}	44.74 {14.68}	24.14 {4.68}	7
PGSAUV 15 min	2.00 {0.13}	115.92 {12.82}	71.06 {7.53}	48.32 {6.62}	5
PGSAUV 20 min	1.95 {0.05}	80.98 {31.76}	38.92 {23.91}	27.09 {17.58}	3
PGSAC 15 min	3.59 {0.41}	124.43 {30.13}	43.98 {8.46}	37.87 {11.43}	6
PGSAC 20 min	3.75 {0.07}	166.86 {16.71}	57.98 {9.61}	52.89 {17.18}	3

Table 5.3 | Summary of obtained results for different variations of PGSA. Values are reported as the mean, followed by the standard deviation in braces. PGSA17, 23, 29 corresponds to 17, 23, 29 % acrylation of PGSA. PGSAUV corresponds to UV lamp cured PGSA23. PGSAC corresponds to PGSA composite. Time in minutes indicates the duration of photocuring.

Increasing the degree of acrylation increased the tensile modulus, the ultimate tensile strength, and the achieved elongation regarding printed PGSA. PGSA17 was the softest achieved material with an average tensile modulus of 1.23 kPa but simultaneously displaying a lower tensile strength and elongation. In contrast to PGS, there was no positive effect on the elongation of PGSA samples with a lower stiffness, despite the fact that the different PGSA inks were synthesized from the same PGS72 batch. An explanation for this discrepancy between PGS and PGSA could be the different conditions in which the materials are polymerized. PGS forms polymer chains through thermal curing at elevated temperatures, while printed PGSA samples were photocured by means of UV irradiation.

The resulting polymer chains from photocuring could, for example, become shorter with an increased degree of acrylation, causing the sample to break upon lesser strain. A second explanation could be due to the fact that printed PGSA is basically a number of stacked photocured layers. The increase in the degree of acrylation could influence the bonds that form while printing between these layers. A third explanation could be that despite the fact that extreme care was taken in preparing the samples, the low stiffness caused some of the softer samples to be afflicted with minor imperfections during handling, potentially causing the samples to fail prematurely (see fig. 5.16 D). Some sample tests could not be incorporated into the results as they suffered from a similar issue with samples not reaching failure within the gauge length of the dumbbell shapes (see fig. 5.16 C).

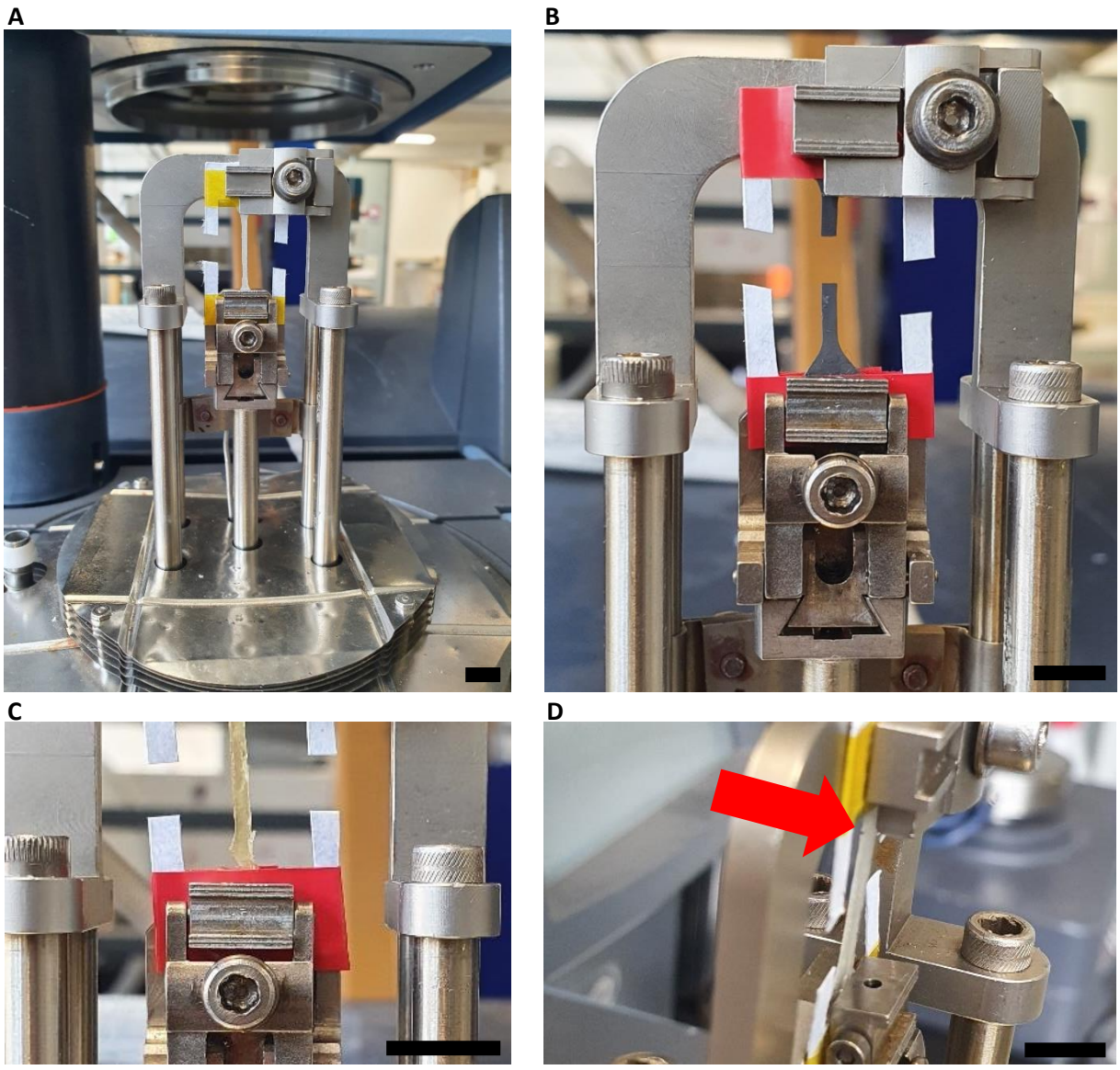

Figure 5.16 | PGSA samples in the DMA. (**A**) PGSA29 samples in a paper frame between the DMA clamps. (**B**) A close-up of a PGSA composite sample in a paper frame that reached representative failure within the gauge length of the dumbbell shape. (**C**) Due to the gripping area of the dumbbell-shaped samples being used for handling, not all failures occurred within the gauge length returning inconclusive results. This specific sample originates from a PGSA23 material batch. (**D**) A small tear in the prepared sample, where failure occurs prematurely. Scale bars are 10 mm.

Photocured PGSA samples demolded from PDMS were fabricated using PGSA23 and showed an increase in stiffness compared to their printed counterparts. This was immediately noticeable after demolding, which greatly facilitated handling these samples. However, except for the stiffness, considering the three different durations of photocuring PGSAUV, the UTS and elongation did not vary too much from the printed samples. While the tensile modulus for PGSA did not change with an increase in curing time, the UTS and elongation show an optimum at 15 min. Altering, in this case, increasing the ratio of the photoinitiator TPO would most likely have resulted in more significant variance in stiffnesses. Based on these results, it can be concluded that PGSA with 1 wt% TPO was already fully cured after 10 min. The comparatively elevated tensile toughness at 15 minutes of photocuring does indicate that other chemical processes are occurring in the time frame between 10 and 20 minutes of curing. Performing FTIR and H NMR on the samples could explain these chemical reactions, but this is outside of the scope of this work. Previous works have not shown the difference between printed PGSA and photocured demolded PGSA, and based on these results with PGSA from the exact same batch of material, there is no significant difference in mechanical properties between the two fabrication methods.

CIP in the elastomeric PGSA23 matrix resulted in a stiffer and stronger material with tensile toughness similar to photocured PGSA. Increasing the duration of photocuring increased both the stiffness and the tensile toughness. PGSAC samples were similar to PGSAUV regarding the handling.

Additionally, thermal post-curing was applied to PGSA17 and PGSAC samples to evaluate the impact on the tensile modulus, ultimate tensile strength, and elongation at break (see table 5.4). Thermal post-curing was performed in an oven at 150 °C for 12 hours for PGSA17, resulting in an increase of the tensile modulus by a factor of over 40. The ultimate tensile strength increased by a factor of 7, while the elongation at break was reduced by a factor of 4. Thermal post-curing was also performed on PGSAC at 150 °C for 3 hours, which increased the tensile modulus and ultimate tensile strength by a factor of almost 10. The elongation did not experience any significant change.

Material	Tensile modulus (kPa)	Ultimate tensile strength (kPa)	Elongation at break (%)	Number of samples
PGSA17	1.23 {0.21}	53.29 {9.08}	39.23 {0.66}	4
Cured PGSA17	50.89 {4.94}	440.12 {24.6}	9.28 {0.67}	4
PGSAC	3.50 {0.51}	83.76 {1.83}	33.94 {5.20}	2
Cured PGSAC	37.98 {-}	861.80 {-}	24.47 {-}	1

Table 5.4 | Changes in mechanical properties due to thermal curing. Values are reported as the mean, followed by the standard deviation in braces. PGSA17 corresponds to 17% acrylation of PGSA. PGSAC corresponds to PGSA composite.

The goal of synthesizing a material with comparable stiffness properties to the iris was successfully achieved to allow for safe interaction between a device and the iris. PGSA could potentially become even softer, but this is not recommended due to the resulting material being very difficult to handle, especially when printed. On the other hand, depending on the level of compliance required by the perceived application, the stiffness can be increased with thermal curing.

5.3.3 Degradation Properties

Extraction of the dumbbell-shaped specimens from the PBS solutions occurred after 7, 14, and 21 days of being placed in a PBS solution in an incubator at 37 °C. Plastic frames prevented the sticky PGSA samples from getting attached to the side walls of the glass vials. Replacement of PBS was unnecessary as the pH, measured with a pH test strip, did not show any change.

Prior to placement of the samples inside the PBS solution, they were washed, soaked, and dried. In the PBS solutions, the samples swelled up once more. Because of this swelling, all samples exhibited buckling but were all extracted successfully without any damage thanks to the polyamide tape (see fig. 5.17 B). The mass loss of the degraded samples was measured three times, and the average remaining mass after each week is presented in figure 5.17 A.

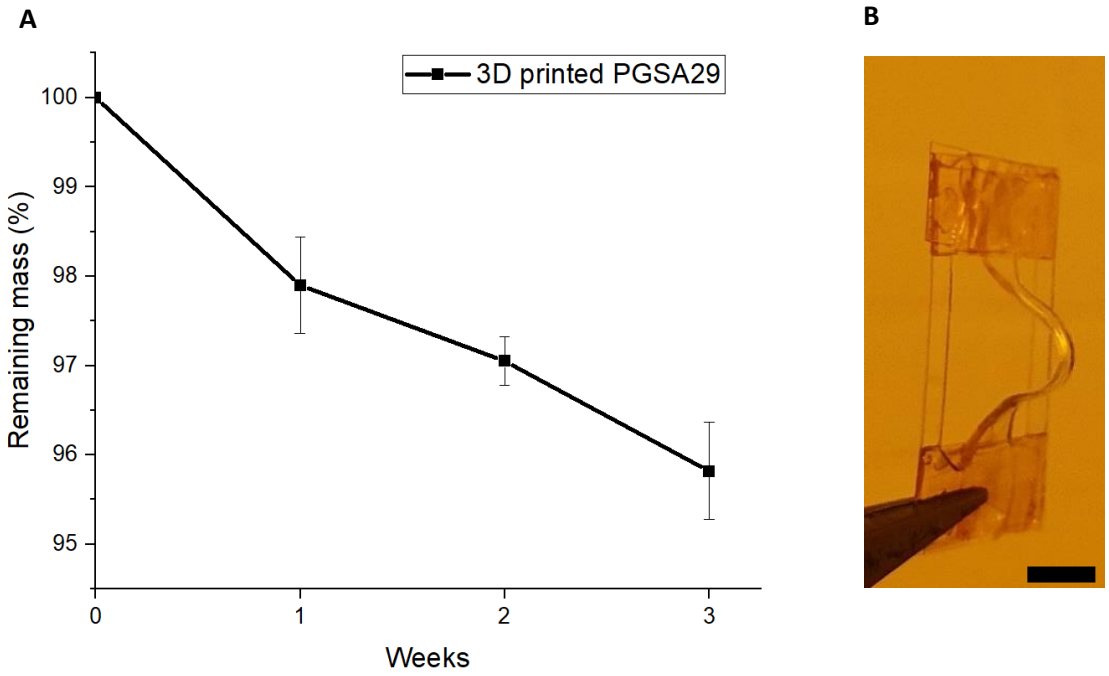

Figure 5.17 | Remaining mass of the degradation samples after drying. (**A**) Error bars represent the standard deviation of the mean. PGSA29 corresponds to 29% acrylation of PGSA. (**B**) Observed buckling after extraction from the degradation medium. Scale bar is 20 mm.

After measuring the mass loss, the samples were subjected to uniaxial tensile tests using the DMA Q800 to study the influence of the mass loss on the mechanical properties. The results are presented in table 5.5. Despite experiencing the mass loss presented in figure 5.17 A, the average tensile modulus increased to a maximum of 1.95 kPa after two weeks, followed by a slight decrease observed after the third week of degradation. Despite this increase in the tensile modulus, it remained insignificant considering the standard deviation. However, a more significant increase was observed for the achieved elongation throughout the degradation assay, with the mean elongation almost doubling after the first week of degradation. PGSA samples were easier to manipulate and handle after weeks 2 and 3. While testing the degraded samples of weeks 2 and 3, three samples were not destroyed and displayed the ability to fully regain their initial shape after testing with the maximum strain that the DMA could provide (see fig. 5.18 and 5.19). This significant increase in elongation, as well as the easier handling of the samples, is believed to be caused by an interaction of the phosphate groups in PBS with the polymer chains present in PGSA. Since there was an increased net weight loss in degraded samples after each week and there was a small decrease in volume, it

might be that some porous cavities still had remnant uncured monomers that remained after washing in ethanol. Perhaps these monomers were only entirely removed after prolonged soaking in PBS, causing a volume decrease after the drying process due to the cavities, now empty, collapsing. The pH of the PBS did not change during the three weeks that the measurements took place, so it is likely not caused by any chemical reaction that has to do with the pH. A second explanation could be that the degradation affects the polymer chains themselves, causing them to become slightly less sturdy. This might have allowed them to reach a higher elongation at break but does not explain the increase in stiffness.

Duration of Degradation	Tensile modulus (kPa)	Ultimate tensile strength (kPa)	Elongation at break (%)	Number of samples
Control	1.42 {0.37}	68.03 {25.83}	69.84 {13.55}	3
1 Week	1.07 {0.21}	124.01 {30.42}	113.96 {16.72}	5
2 Weeks	1.94 {0.19}	315.63 {57.14}	144.06 {8.35}	4
3 Weeks	1.41 {0.05}	163.646 {42.29}	113.66 {21.84}	2

Table 5.5 | Summary of the mechanical properties of the degraded samples. Results from the samples that did not reach failure are excluded. Values are reported as the mean, followed by the standard deviation in braces.

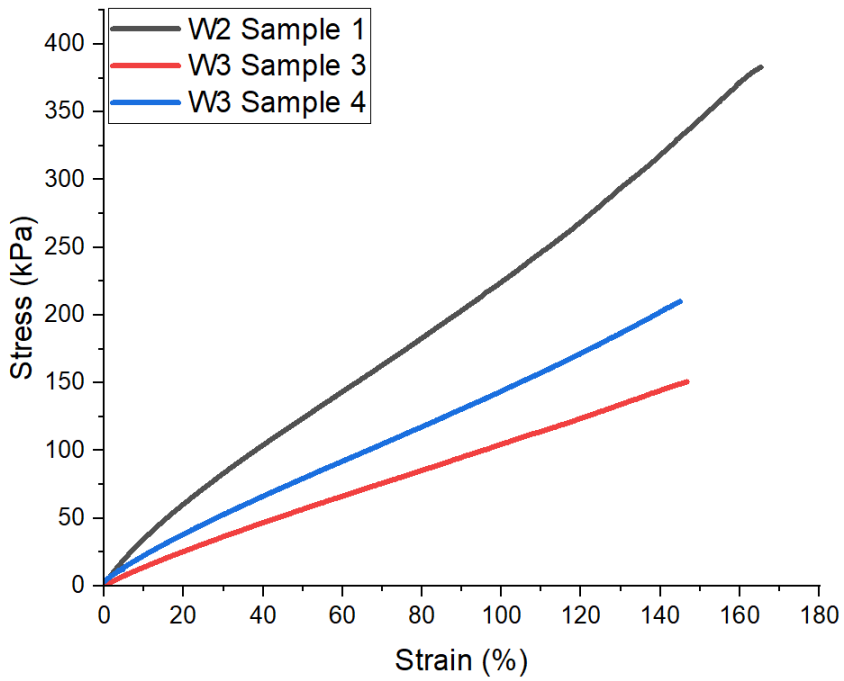

Figure 5.18 | Stress-strain curves of the PGSA degradation samples that were not destroyed during testing.

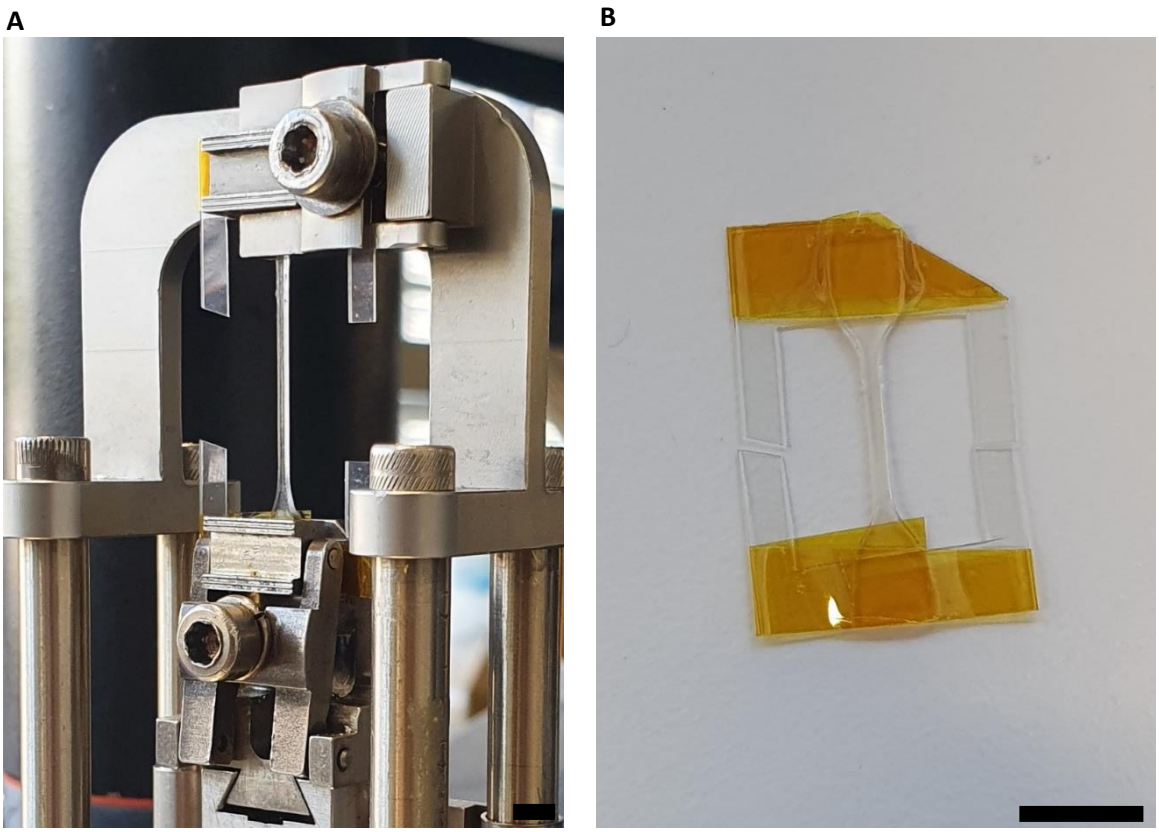

Figure 5.19 | PGSA regained its initial shape after a strain of 165%. (**A**) During the tensile test at maximum elongation (**B**) Sample immediately regains its initial shape after loosening either clamp. The upper right corner of all the frames (in this case, plastic) was cut as it obstructed the hex socket cap screw used to tighten the upper clamp of the DMA. Scale bars are 10 mm.

As expected, the weight loss of the PGSA samples in PBS was quite low. As previous works have shown, PGSA is more susceptible to rapid biodegradation in in-vitro enzymatic solutions. Moreover, since PGS has been used in the human body and the degradation properties are relatively well-known, the hydrolysis degradation experiment resulted in degradation properties that can be compared to PGS. In this experiment, 3D printed PGSA, as well as the UV lamp photocured PGSA and PGSA composite, were tested and compared to the different degrees of cross-linked PGS discussed in section 5.3.1. The results are presented in figure 5.20.

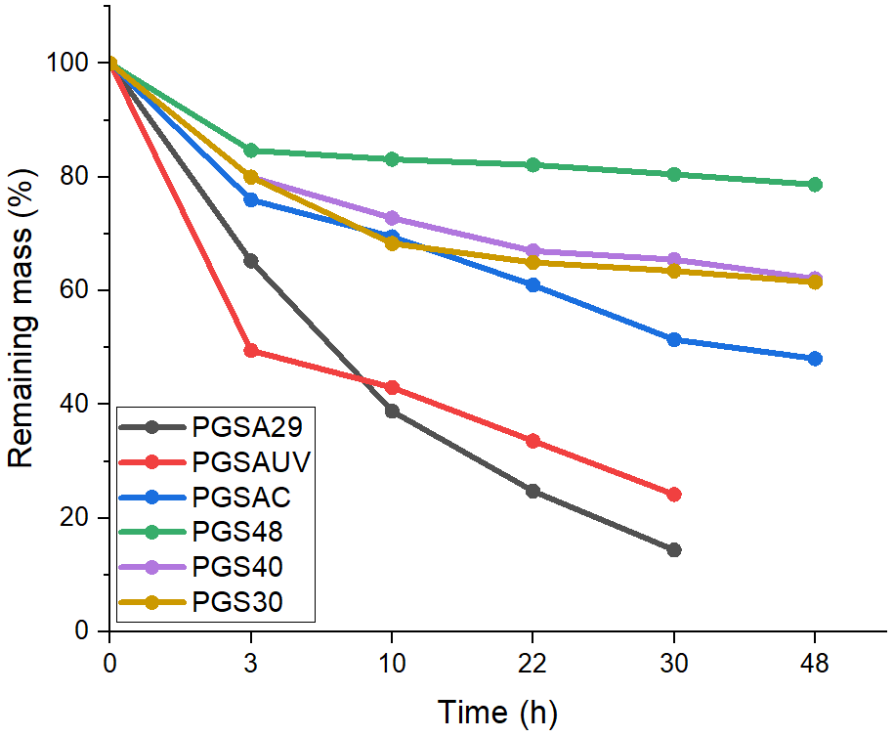

Figure 5.20 | In vitro hydrolytic degradation of 3D printed PGSA, PGSAUV, PGSAC, and PGS showing the remaining mass after extraction from a 0.1 mM NaOH solution. The PGSAUV sample could not be measured at the 22-hour time interval, this value was therefore extrapolated. No data could be obtained for PGSA29 and PGSAUV at the 48-hour interval. PGSA29 corresponds to 29 % acrylation of PGSA. PGSAUV corresponds to UV lamp cured PGSA29. PGSAC corresponds to PGSA composite. PGS30,40,48 corresponds to 30, 40, 48 hours of thermal curing.

The weights of both printed and UV-cured PGSA could not be measured after 48 hours for two different reasons. Printed PGSA experienced dimensional shrinkage while maintaining its square shape, but the sample became very rigid. This caused it to be too fragile to be measured after 48 hours as it immediately fragmented in the NaOH solution while trying to retrieve it. The sample remained very elastic for UV lamp-cured PGSA from the same batch and could not be measured after 48 hours due to it being stuck to the plastic holder it was placed in after extraction. The degradation rate showed some similarity over the first 30 hours, meaning that the fabrication method did not directly influence the mass loss and was limited to the degradation mechanism only. This is most likely caused by differences in the internal polymeric structures. This can be explained by the method 3D printed PGSA works compared to simply photocuring samples with a UV lamp. Additive manufacturing cures, in this case, 20 µm thick layers one by one, contrary to in the case of PDMS molds where a uniform mix of PGSA is already clumped together and is cured at once.

Three different degrees of cross-linked PGS were subjected to the same experiment, resulting in slower degradation than PGSA. PGS48 exhibited relatively low mass loss and almost no dimensional shrinkage. PGSA composite maintained its shape and showed degradation properties similar to PGS. Adding 20 wt% biodegradable CIP to the PGSA elastomeric matrix allowed PGSAC to slow down its degradation to similar values as that of PGS (see fig 5.21 C).

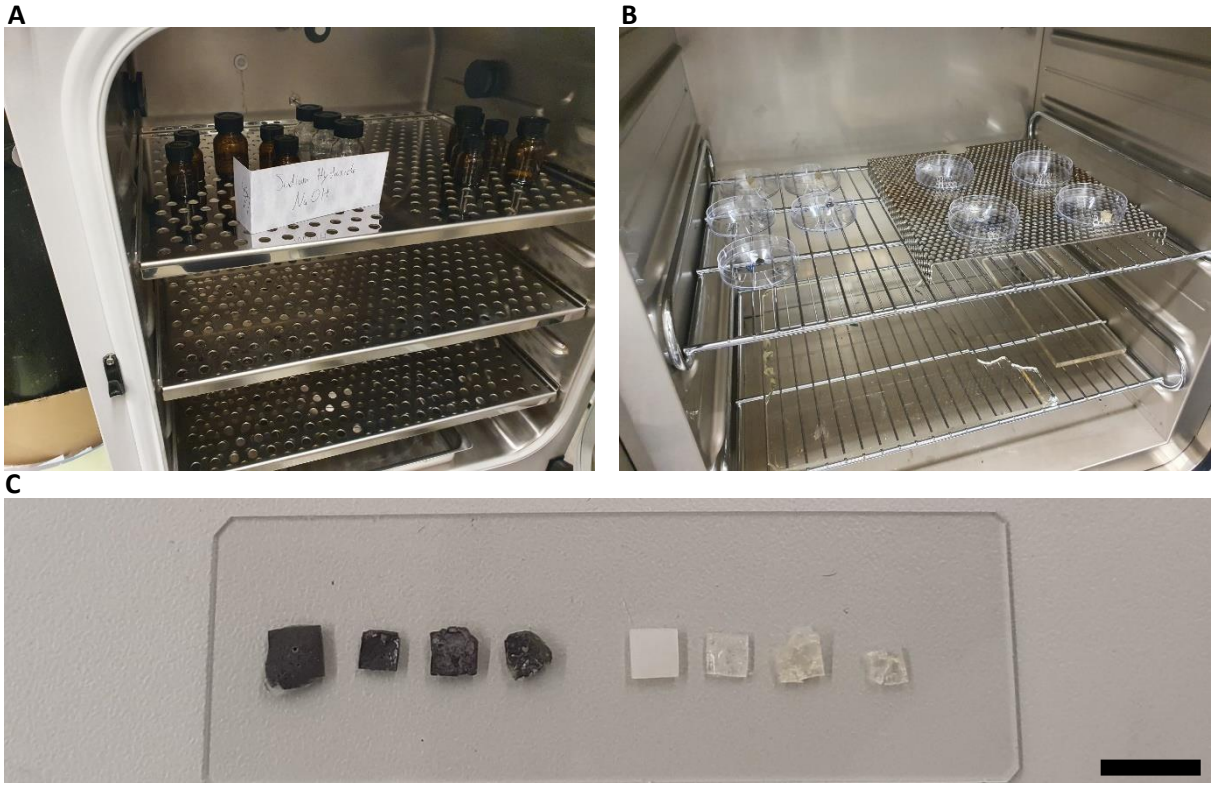

Figure 5.21 | Hydrolysis of fabricated samples. (**A**) Samples in the glass vials in an incubator. (**B**) Extracted samples drying in the oven at 60 °C before measuring the dry weight. (**C**) PGSAC (left, samples with black color) and printed PGSA (right, white color) at different stages of degradation. From left to right: 1) original sample after fabrication. 2) Sample after soaking in PBS. 3) Sample after 3 hours of degradation in NaOH. 4) Sample after 10 hours of degradation. Scale bar is 10 mm.

5.3.4 Gel Permeation Chromatography

GPC measurements provide chemically relevant information for the characterization of the materials that were synthesized in this project. The main results achieved are the molecular weights of PGS and PGSA. The molecular weight of the synthesized PGS is 2073 Da, equivalent to 2073 $g \cdot mol^{-1}$. The molecular weight of the synthesized PGSA29 is 4052 Da, equivalent to 4052 $g \cdot mol^{-1}$. Detailed results are presented in table 5.6.

Polymer	M_n (kDA)	M_w (kDA)	M_z (kDA)	M_M/M_n
PGS	1.5	2.1	3.1	1.4
PGSA	2.4	4.1	7.1	1.7

Table 5.6 | Results from the GPC. M_n is the number average molecular weight. M_w is the average molecular weight. $D = M_w/M_n$ is the dispersity of the polymers.

These values agree with measurements in previously published works on PGS, indicating that despite the slightly altered synthesis conditions did not influence the synthesized materials. The large peaks displayed in figure 5.22 at 10.5 and 10.75 minutes are the result of the detection of the solvent DMF. The peak indicating the detection of PGS and PGSA is highlighted in figure 5.23.

The polycondensation process, in this case of an equimolar mixture, is directly related to molecular weight. The higher the degree of cross-links formed during the polycondensation, the higher the molecular weight. Previously published works have shown that higher molecular weights of PGS were achieved with an equimolar mixture of glycerol and sebacic acid, it then follows that the PGS used in this work, PGS72, could be cross-linked further to increase its molecular weight.[130]

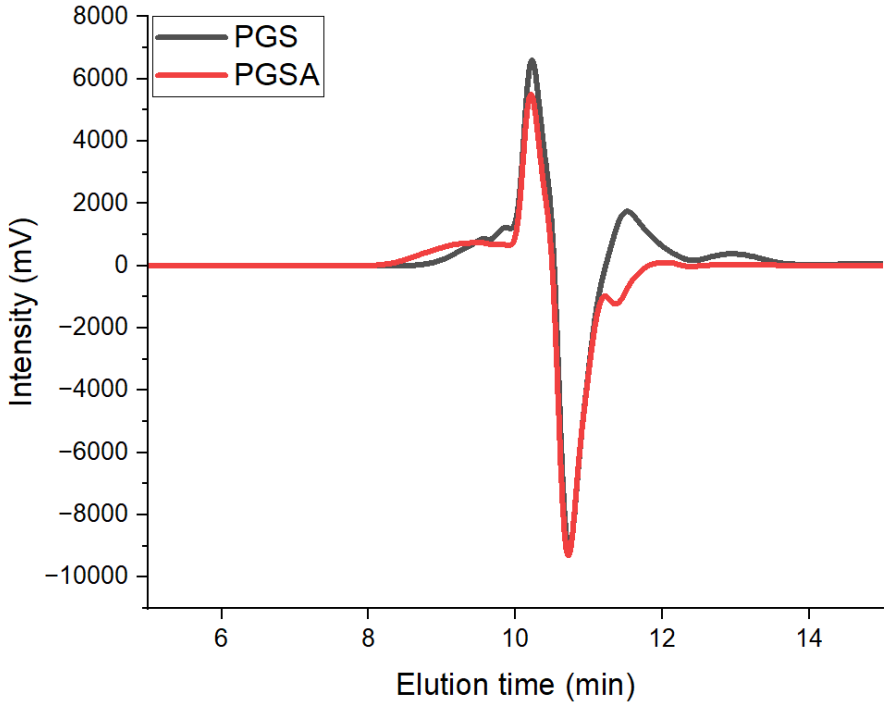

Figure 5.22 | Chromatogram resulting from the GPC tests. A good baseline was measured before the peaks of the polymers were measured after the 8-minute mark, which is indicative of a reliable run.

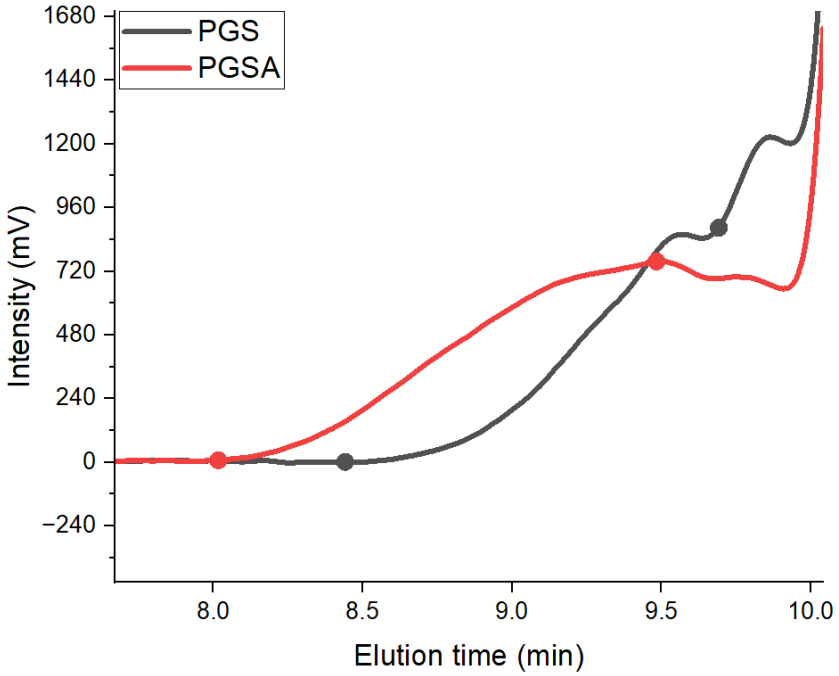

Figure 5.23 | PGS and PGSA chromatogram peaks. The GPC detected PGS between approximately 8.5 and 9.7 minutes and PGSA was detected between 8 and 9.5 minutes. The time marks are highlighted with a dot.

The peak for both polymers is similar but slightly larger for PGSA, indicating a higher molecular weight due to the area under the curve, which was 20% higher than that of PGS. This can be due to multiple factors. The PGSA peak is detected between 8 and 9.5 minutes, while the peaks of the solvent remain virtually unchanged. PGS is used without any purification to initiate the acrylation process by adding acryloyl chloride and triethylamine, having a molecular weight of 90.51 $g \cdot mol^{-1}$ and 101.19 $g \cdot mol^{-1}$, respectively, which could add to its molecular weight. However, it must also be considered that it could be because of the auto-cross-linking of PGS while the acrylation process is ongoing. 4-methoxyphenol is added to the mixture before and after the acrylation step as a polymerization inhibitor to prevent auto-cross-linking of PGS during acrylation. During the synthesis of the different batches of PGSA, it was noted that when higher amounts of PGS (>40g) were used, the mixture appeared more opaque after 24 hours of acrylation. When lower amounts of PGS were used (<30 g), the mixture was visibly more transparent. It is believed that even though the ratio of 4-methoxyphenol is adapted appropriately, this increase in molecular weight of PGSA could be caused by premature cross-linking of the higher concentration of PGS (see appendix: Protocol - Poly Glycerol Sebacate Acrylate Ink for DLP 3D Printing, step 28). This is in accordance with the increased opaque appearance of the mixture after 24 hours of acrylation. It must be noted that a PGSA batch synthesized with an initial weight of PGS of 70 g with the same degree of acrylation also led to more brittle prints (see fig. 5.24).

Figure 5.24 | PGSA synthesized with an increased amount of PGS prepolymer. This resulted in a yellow ink color, which was only the case for this batch, and caused brittle prints.

5.3.5 Swelling and Shrinking Properties

In the literature, ethanol is used to remove uncured monomers and sterilize medical implants. PBS is used as a solution that mimics the human body. For this project, they are used in the post-processing of fabricated samples, and it is important to know the material behavior in these conditions. Therefore square-shaped PGSA samples were fabricated, placed in ethanol for 24 hours, and subsequently in PBS for 24 hours to study the swelling and shrinking of the different PGSA variations (see fig. 5.25). Table 5.7 presents the changes in mass as well as the dimensional changes caused by ethanol and PBS.

Material	Ethanol		PBS	
	Mass (%)	**Volume (%)**	**Mass (%)**	**Volume (%)**
PGSA	113.97 {33.24}	129.84 {6.49}	0.50 {12.35}	- 6.60 {13.86}
PGSAUV	147.78 {22.36}	186.81 {4.91}	19.95 {10.29}	5.08 {11.56}
PGSAC	15.84 {10.27}	24.85 {13.32}	- 19.34 {7.43}	- 11.01 {16.17}

Table 5.7 | Summary of changes relative to initially fabricated samples. Positive entries indicate increase, negative entries are indicative of decrease. Values are reported as the mean, followed by the standard deviation in braces. PGSAUV corresponds to UV lamp cured PGSA. PGSAC corresponds to PGSA composite.

Ethanol uptake in PGSAUV is higher than that of the printed PGSA despite being from the same batch. The resulting final samples of PGSAUV remained slightly larger than the initially fabricated squares, while the printed PGSA was slightly smaller than the initial print, this is also true for the mass changes. While the mass increase is higher in PGSAUV, the mass decrease in PBS was the same, which is not the case for the dimensional change. The 5% larger PGSAUV and 6% smaller printed PGSA is the small discrepancy mentioned in section 5.3.2 but was still accommodated by the cut paper frames. PGSAC is less affected regarding both mass and dimensional changes, both are significantly lower in PGSAC, which in turn causes the final samples to be around 11% smaller and 19% lighter than the initial fabrication.

Figure 5.25 | Measurement of 3D printed dumbbell-shaped sample after ethanol uptake and soaking in PBS.

Weights of the degradation samples used in section 5.3.3 were also measured after extraction and before drying from PBS after degrading for 7, 14, and 21 days. These samples were already treated with ethanol and PBS previously and were dried before being placed inside the PBS solution. Interestingly enough, the degradation samples showed significant PBS uptake (see fig. 5.26), contradicting the results of the smaller squares when placed in PBS immediately after ethanol uptake.

To investigate this phenomenon further, printed PGSA samples were placed in PBS immediately after being printed for 24 hours. While the mass increased by 48.74%, the volume slightly decreased by 6.16%, indicating that PGSA does, in fact, experience PBS uptake while causing slight shrinkage, regardless of any prior treatment. This is in accordance with previous measurements of the degradation samples, where after each week, PBS uptake led to a slightly higher mass immediately after extraction.

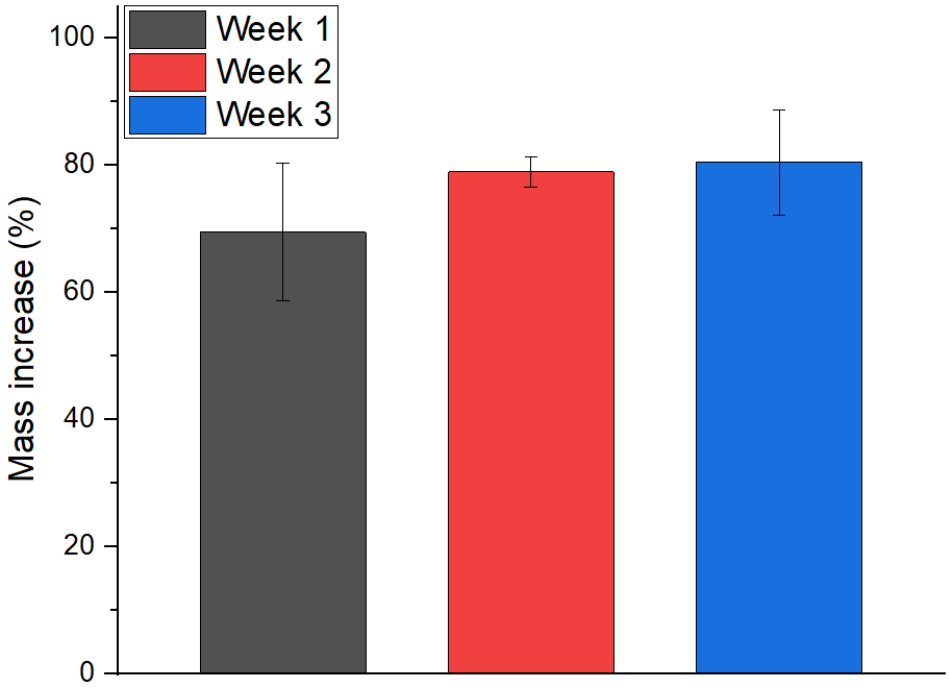

Figure 5.26 | PBS uptake in degradation samples. Week 1 n = 5, week 2 n = 5, week 3 n = 4. Error bars represent the standard deviation of the mean.

5.3.6 Hyperelastic Material Model Parameters Derived from Mechanical Properties

The results from the tensile tests were used to plot the stress against the stretch of the samples in the 0D COMSOL model. The model requires an analytical expression for the engineering stress containing the hyperelastic parameters to fit the results of the uniaxial tensile test data using the optimization module. An expression for the Mooney-Rivlin parameters is already present in COMSOL and is based on the Cauchy and the 2nd Piola-Kirchoff stresses. These are derived for the different models from the volumetric stress, which is given as[94]:

$$S = 2\left(\frac{1}{\lambda} - \frac{1}{\lambda^4}\right)\left(\lambda\frac{\partial W}{\partial I_1} + \frac{\partial W}{\partial I_2}\right)$$

Where λ is the stretch, ∂W is the isochoric strain energy density, and the isochoric invariants are $I_1 = (\lambda^2 + \frac{2}{\lambda})$ and $I_2 = (2\lambda + \frac{1}{\lambda^2})$. This is under the assumption of complete incompressibility and limiting the expression to only uniaxial forces for the invariants.

Then, in the Comsol model, the following stresses are defined:

The 2nd Piola-Kirchoff stress: $S(\lambda) = \frac{P(\lambda)}{\lambda}$

Cauchy stress: $\sigma(\lambda) = \lambda P(\lambda)$

Finally, in the optimization model, the following equations are used to estimate an expression for:

The Mooney-Rivlin parameters[94,131]:

$P(\lambda) = 2(C_{10} + \frac{C_{01}}{\lambda})(\lambda - \frac{1}{\lambda^2})$ With parameters C_{10} and C_{01} to be determined with curve fitting.

And the Neo-Hookean parameter[94]:

$P(\lambda) = \mu\,(\lambda - \frac{1}{\lambda^2})$ With parameter μ to be determined by curve fitting.

Material	Hyperelastic material model parameter		
	Mooney-Rivlin		Neo-Hookean
	C_{10} (Pa)	C_{01} (Pa)	μ (Pa)
PGSA17	-15954	68713	74978
PGSA23	63294	-43587	65211
PGSA29	64159	-29601	84718
PGSAUV	60663	-28585	84385
PGSAC	97056	-25780	155160

Table 5.8 | Resulting hyperelastic material model parameters based on representative stress-strain curves from uniaxial tensile testing.

5.4 Device Actuation

This chapter demonstrates the suggested actuation strategies from the literature review with the fabricated prototypes. Actuation by means of pneumatic and magnetic actuation are described in chapters 5.4.1 and 5.4.2, respectively.

5.4.1 Pneumatic Actuation

The internal chamber of the printed devices highlighted in section 5.2.3 was inflated utilizing the Elveflow pressure controller and a dispensing tip with a diameter slightly larger than the printed circular inlet.

First, to verify the ability of the rim-like geometries of the prototypes to expand into the required circular shape of the iris, an air gun was used to blow air perpendicular to the device on a small glass plate. It was possible to achieve a quasi-circular pattern without any ruptures or tears of the hollow device.

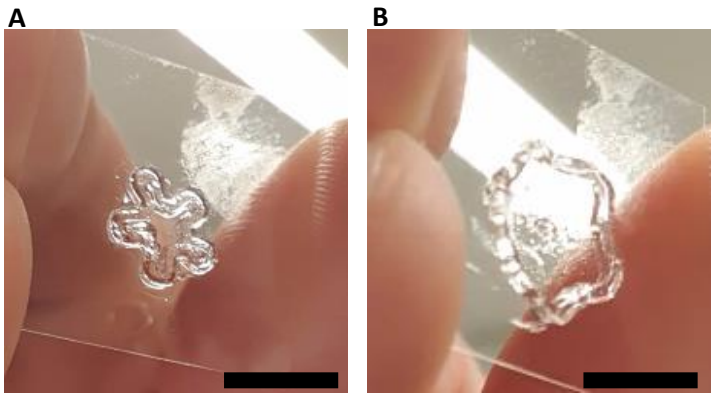

Figure 5.27 | Rim-like prototype expanding by means of applying air from outside the device. Scale bars are 5 mm.

Then, when trying to actuate the prototype by inflating the internal chamber by inserting a dispensing tip inside of the channel, instead of causing the channel to inflate, it caused the small and lightweight prototypes to be launched (see fig. 5.28). Therefore, the channel was manually closed off to secure the connection between the dispensing tip and the prototype. By applying a pressure of approximately 800 mbar, it was possible to repeatedly increase and decrease the diameter of the circular ring-shaped prototype (see fig. 5.29). The prototypes displayed the ability to deform and return to their original shapes while proving to be sturdy and capable of maintaining their structural integrity even after manual agitation (see fig. 5.30).

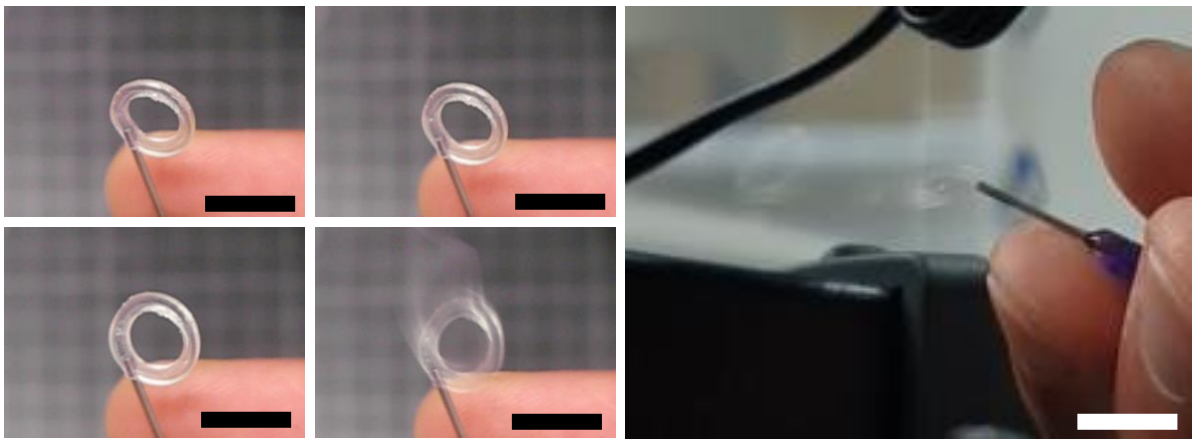

Figure 5.28 | Prototype getting launched from the dispensing tip. Scale bars are 10 mm.

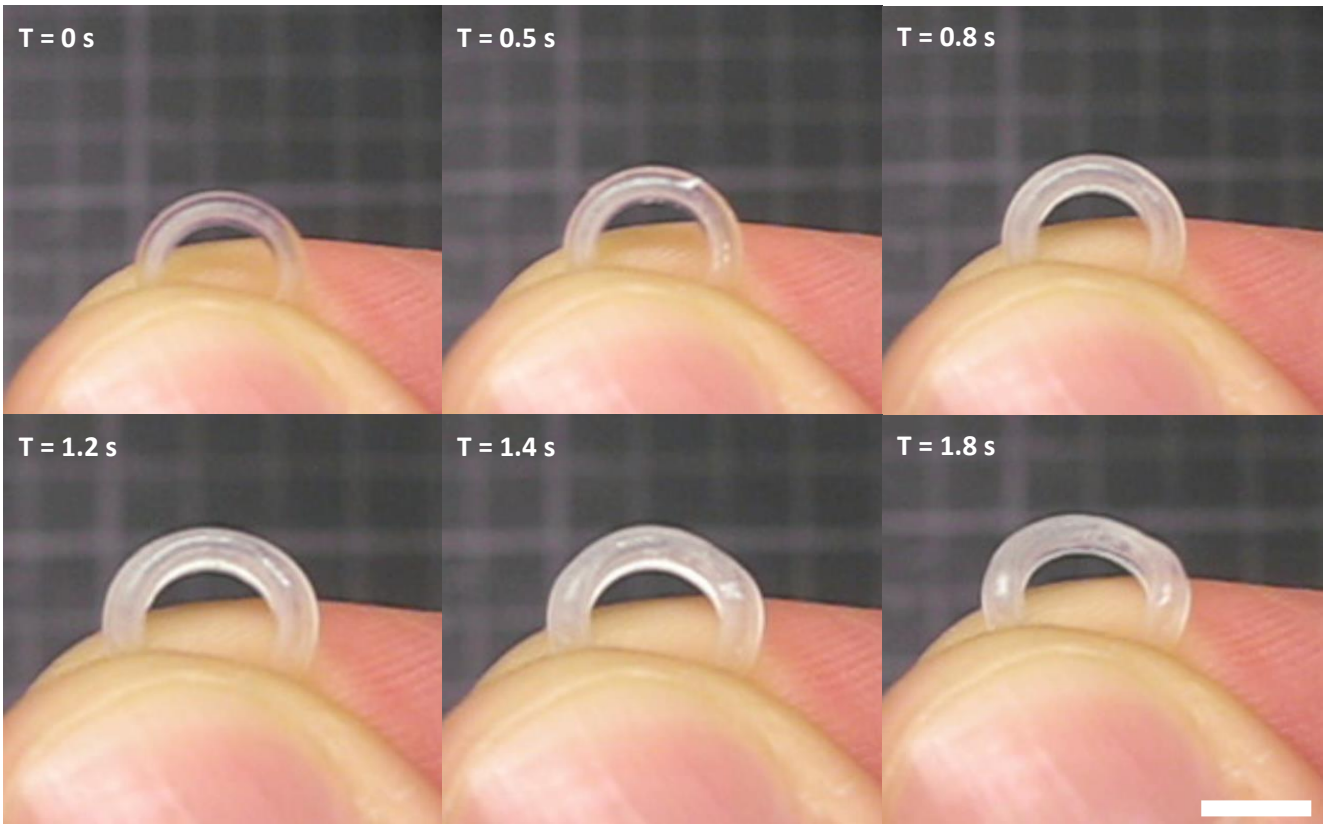

Figure 5.29 | Achieved pneumatic actuation. The outer diameter of the device is 8 mm in the deflated state, and the channel diameter is approximately 0.7 mm. The wall thickness on the inside perimeter is 0.1 mm, and 0.25 mm for the outside perimeter. Scale bar is 5 mm.

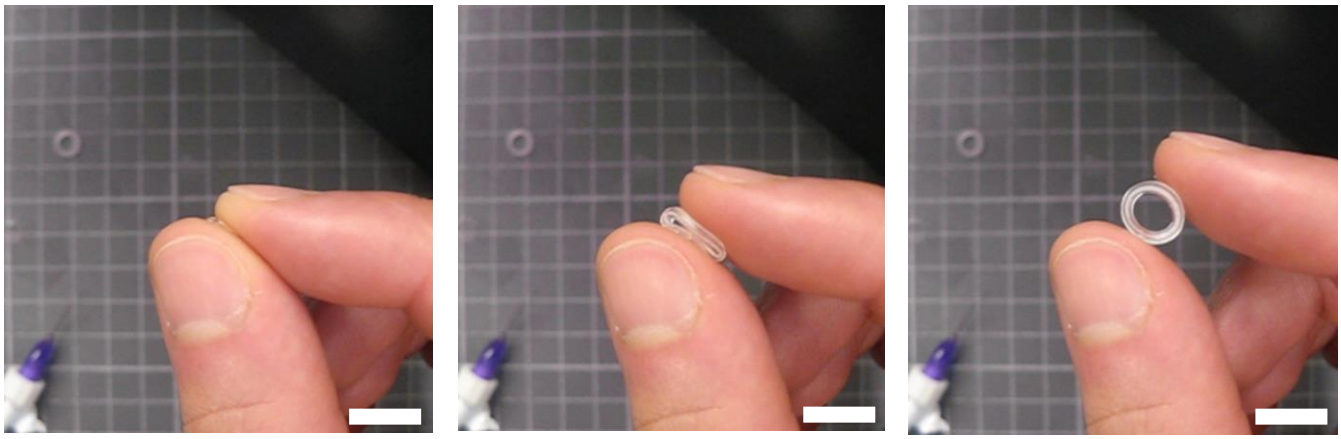

Figure 5.30 | Manual agitation of a prototype. The prototypes can regain their original shape after compressing and stretching them manually while maintaining structural integrity. Scale bars are 10 mm.

When providing pressures above 800 mbar, usually closer to 1000 mbar, the prototypes would burst, letting the air inside escape. These ruptures often occurred on the opposite side of the channel inlet (see fig. 5.31).

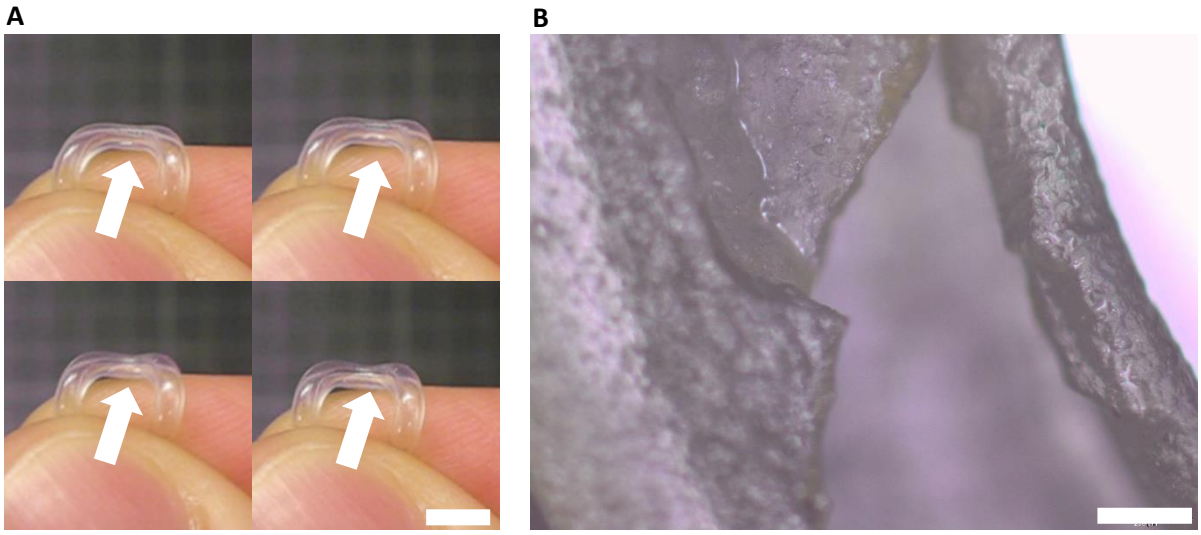

Figure 5.31 | Destroyed prototype due to overpressure. (**A**) Most prevalent location for ruptures and the visually detected propagation of the failure. Scale bar is 5 mm. (**B**) Microscopic image of a rupture caused by overpressure inside of a prototype. Scale bar is 200 µm.

5.4.2 Magnetic Actuation

Both 3D printed and molded magnetically active PGSA composites were subjected to a magnetic field generated by an electromagnet. In addition, printed PGSA composite was also subjected to permanent magnets. Permanent magnets were positioned in order to increase and decrease their proximity to the sample, resulting in a variable applied magnetic field. The electromagnet was controlled by means of changing the voltage and current using a power supply unit. The voltage varied between roughly 0 and 50 V, while the current reached a maximum of 5 A.

Figure 5.32 presents the actuation of a 3D printed PGSA composite ring displaying locomotion toward a permanent magnet. The CIP particles had no specific alignment inside the elastomeric matrix during the printing process.

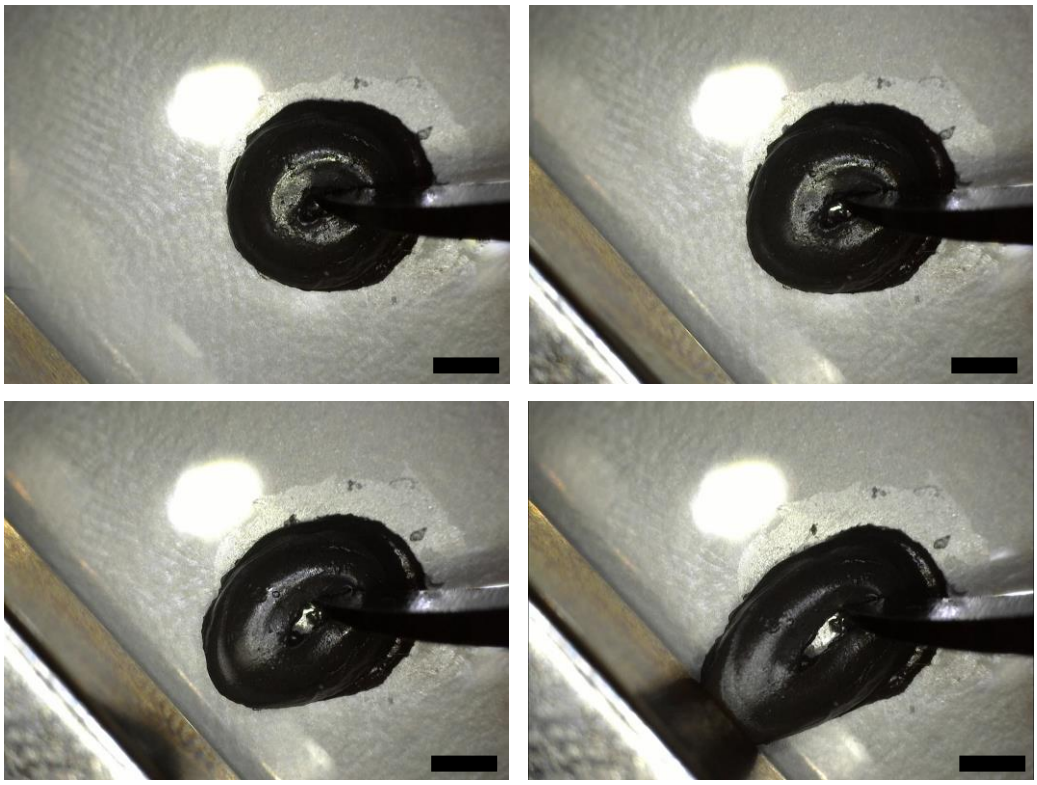

Figure 5.32 | Achieved magnetic actuation. Unilaterally approaching the 3D printed PGSA composite ring. Scale bars are 2 mm.

3D printed PGSA rings were also placed inside the magnetic gap of the electromagnet. However, for circular expansion to occur in reaction to the generated magnetic field lines inside the gap, the ring would have to possess a very particular distribution of magnetic particles inside the soft matrix of PGSA. A 3D printed dumbbell shape was suspended in the magnetic gap of the electromagnet, and a straightening motion could be observed, which is presented in figure 5.33.

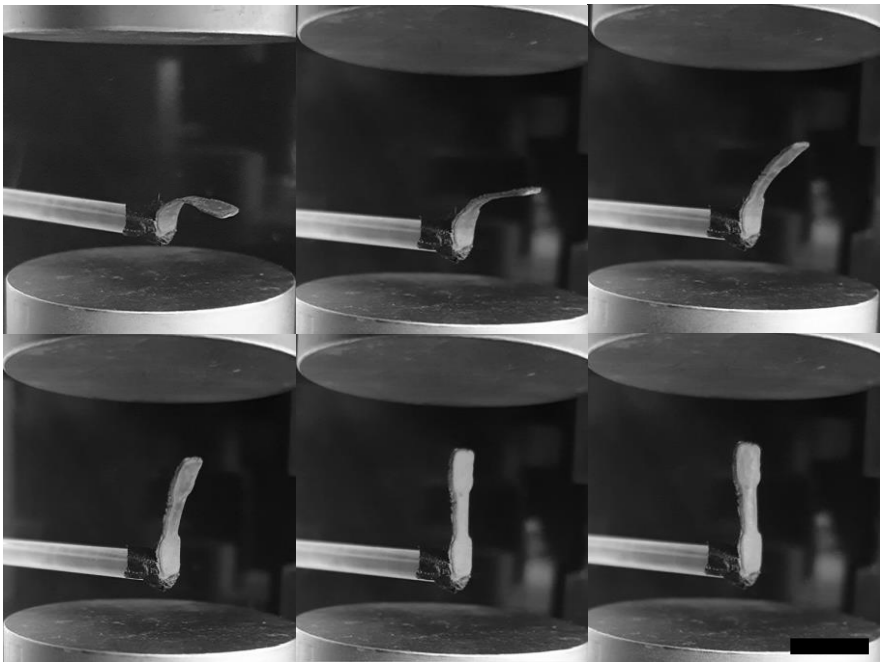

Figure 5.33 | straightening of 3D printed magnetically active PGSA composite. The voltage is increased from 0 to 34.5 V to fully straighten the sample. Scale bar is 10 mm.

The molded PGSA composite samples were subjected to an electromagnetic field to verify the different particle alignments described in section 4.2.2 to demonstrate that the particles can indeed be aligned inside the elastomeric matrix of PGSA. Samples were individually placed in the magnetic gap while the voltage was set to 0 V. Then, increasing the voltage output made it possible to achieve different actuation patterns, some of which are presented in figure 5.34.

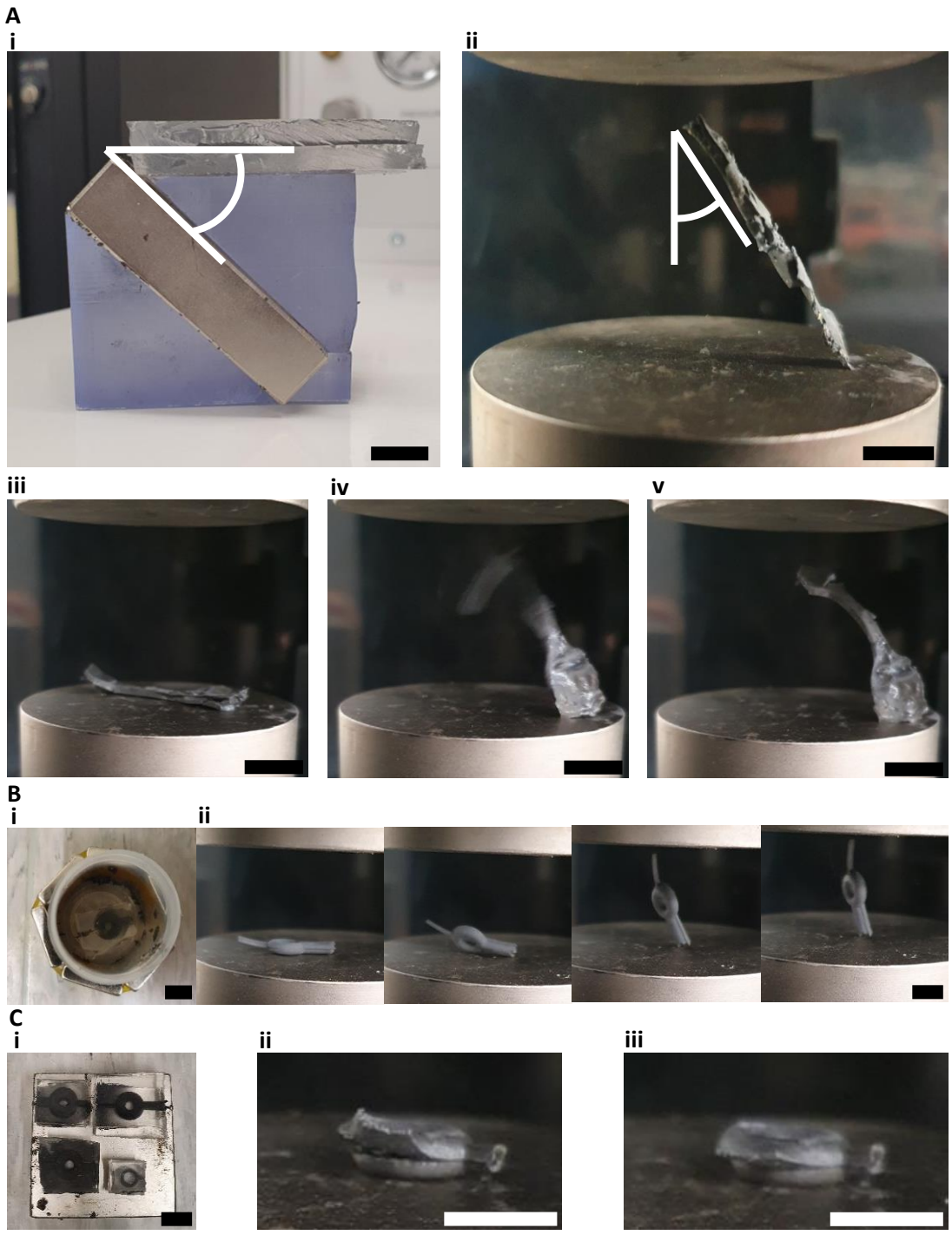

Figure 5.34 | Examples of actuation with different particle alignments in PGSA composite. (**A**) i, Particles are aligned at an angle due to the positioning of the permanent magnet. ii, Magnetic particles align to the uniform magnetic field, causing the sample to become slanted. iii, PGSA composite sample when the magnetic field is off. iv, The sample actuation according to the particle alignment by increasing the generated magnetic field. v, The sample when the magnetic field is maintained. (**B**) i, Radial configuration of the permanent magnets around the sample with the objective to give an orientation to the magnetic particles during UV curing. ii, Actuation overview of a sample with radial particle alignment while increasing the magnetic field. (**C**) i, UV curing on a permanent magnet causes the particle to align downward from this top-view. ii, A sample with no magnetic field. iii, When the magnetic field is activated, the sample aligns completely to the horizontal axis. Scale bars are 10 mm.

6 Discussion and Future work

In the literature, the synthesis of PGS is very straightforward, and the widely accepted protocol consists of two main polycondensation steps under two different environments. The first is usually a 24 hours polycondensation step in a nitrogen environment, and a second polycondensation step for at least another 24 hours in a vacuum environment. However, this process can be modified to change the resulting mechanical properties, as proposed in the present work. The first step under nitrogen flow is reduced to only 2 hours, after which the polycondensation is continued for a prolonged time in a vacuum oven. The advantage of the proposed synthesis approach is to allow for easier processing in the context of the limited access conditions of the lab used at EKL. However, there is also the following drawback. During the second step of the polycondensation reaction in a vacuum oven, it was impossible to keep stirring the polymer, and this lack of stirring impacts the polymerization process, which will need further investigation.

A PGSA composite (PGSAC), achieved by mixing carbonyl iron powder with the synthesized PGSA ink, could be DLP printed with an ASIGA Max X. While this was done with an arbitrary distribution of magnetic particles, it is the first time a polymer composite was printed via DLP printing. After contacting Asiga, they confirmed that it is possible to include permanent magnets in close proximity to the build tray while a print is occurring. This could potentially lead to different alignments of the CIP particles of each individual layer. Therefore, with 3d printing PGSA composite, not only more complex shapes can be realized, but even more complex magnetic particle alignments could also potentially be realized. This would also make it possible to fabricate a 3D printed PGSA composite ring with the required alignments for radial expansion. However, a more intricate setup of permanent magnets or a stronger electromagnetic field is required to achieve the desired radial expansion with PGSA composites.

Soft robotics allows for soft sensing methods as well as actuation. Implementing sensing capabilities onto the pneumatically actuated device would give the surgeon information about the rate of iris dilation and constriction while performing the surgery. Basic capacitive sensing could be one of the sensing methods for this purpose but was not attempted during this thesis.

With the Asiga MAX X, it is possible to cure different layers and areas of the print with varying energy exposure. This can be achieved by either increasing the duration of exposure, increasing the light intensity, or combining both. Based on the mole fraction of the photoinitiator used in the PGSA ink, two radicals are formed during the cleavage reaction. Since this is the case, it is theoretically possible to cure the polymer with different energies. However, it greatly depends on the prepolymer and photoinitiator ratio. If sufficient photoinitiator is added to the polymer, it should be possible to create PGSA prints where different mechanical properties are available throughout the print. This could open the door for 4D printing applications.

Previous works provided different solutions for dealing with the demolding of sticky materials, such as PGS. In this project, the use of ethanol and PBS did not help with the demolding of PGS, which was therefore not further considered for the fabrication of the final device. Perhaps a different demolding agent could be investigated in the future to demold the samples at the required level of cross-linking.

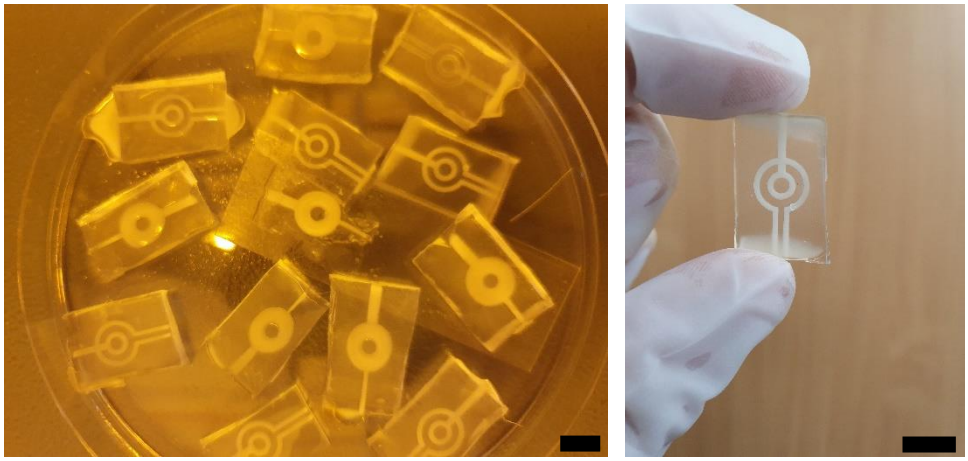

Figure 6.1 | PGS samples after soaking in ethanol and PBS. Except for changing the appearance, it did not help with the demolding of PGS from PDMS molds. Scale bars are 10 mm.

Rectangular PGS samples were used for mechanical characterization during tensile testing. This was due to the temporary unavailability of a laser cutter. A laser cutter will allow the same ASTM D412 dumbbell shapes used for PGSA to give more optimal failure modes. The dimensions of the gauge length were carefully measured, but this process would be more accurate if dumbbell-shaped samples were fabricated. PDMS demolding of these shapes was, similar to the issue in figure 6.1, still not possible for the desired curing durations described in section 5.3.1.

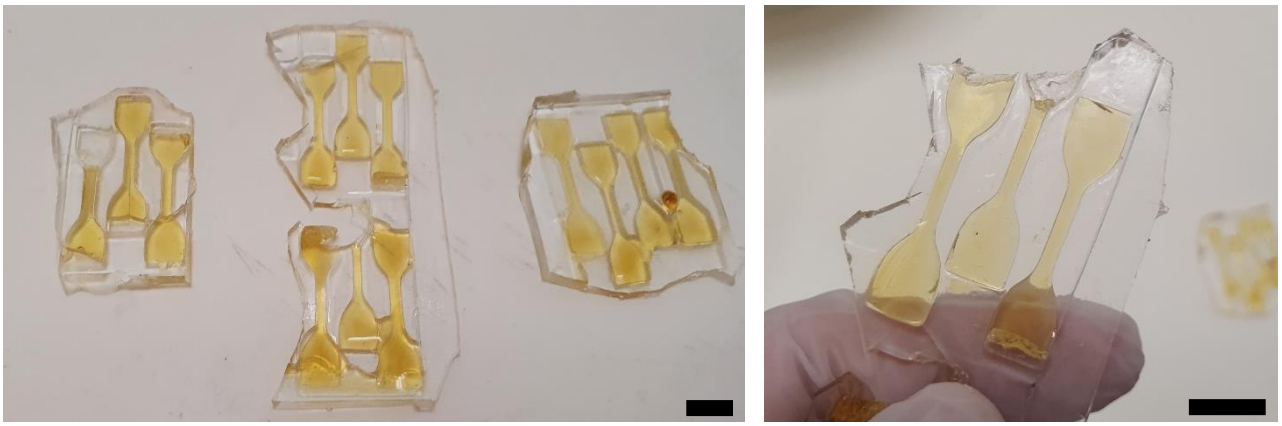

Figure 6.2 | Dumbbell-shaped PGS molds. It was not possible to demold the displayed samples. Scale bars are 10 mm.

While synthesizing PGSA, washing and purifying as best as possible during the process is very important. Incomplete removal of triethylamine salts and not washing with an HCL solution will cause great imperfections in the final material (see fig. 6.2).

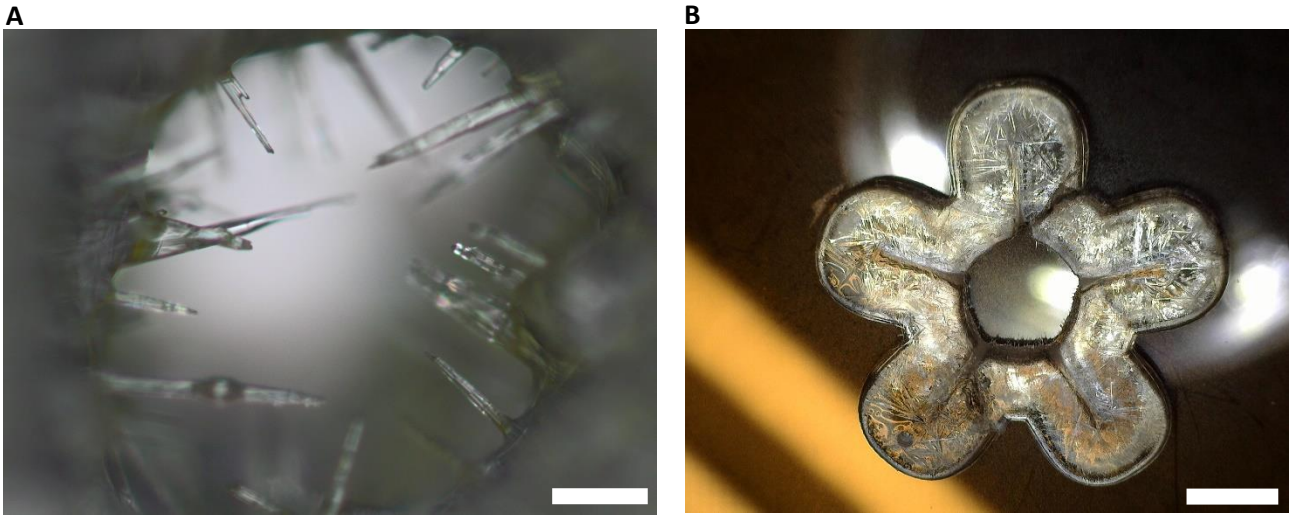

Figure 6.3 | Crystal-like imperfections in insufficiently washed PGSA. (**A**) Close-up of the crystal-like spikes present on the inside and outside of a fabricated prototype. Scale bar is 50 µm. (**B**) The spikes are visible throughout the prototype while still having good feature definitions. Scale bar is 2 mm.

Relevant future work will have to include the synthesis and material characterizations of a broader range of degrees of acrylation for PGSA and different ratios of reagents. In this thesis, equimolar amounts of glycerol and sebacic acid were used for the condensation of PGS, and equimolar amounts of acryloyl chloride and triethylamine were used for the acrylation step. A good place to start would be changing these ratios.

Unfortunately, it was not possible to measure the viscosity and change of viscosity of the synthesized inks with time. The Asiga possesses a function termed “Viscosity analyzer”, which determines a range of the viscosity of the material in the build tray based on the flow speed measured by the sensors after the build platform is dipped in the ink. However, this function was only able to provide some reference values. In the future, characterization of the viscosity will give a precise range of values that the ink has to maintain. Currently, this is based on trial and error and personal experience.

The increase in tensile properties and elongation of the 3D printed degradation samples could be because of the polymer chains that are less strongly bonded after degradation. This causes the chains to be weaker and allow for more elongation when tested. The samples were not tested by soaking in demi water, which would have resulted in a very interesting comparison that would tell if the increase in the measured properties was perhaps due to the phosphate groups in PBS. Also, the results of this degradation assay can now be used to alter the mechanical properties of PGSA.

The achieved materials have a lower tensile modulus compared with previously published works while simultaneously achieving tensile toughness similar to previously published works with comparable degrees of acrylation of PGS. From this, it can be concluded that the material properties have been successfully adjusted for use in the final overarching aim of this project. Studies investigating mechanical properties of the eye conclude that the tensile modulus of the iris ranges between 0.52 and 4 kPa. [132–134] Meaning that the synthesized materials are optimal for the application regarding safety and capability of soft pneumatic and magnetic actuation.

Soft fluidic actuation also includes hydraulic actuation. While this was attempted, it suffered from the same issue that pneumatically actuated samples deal with. The prototypes were able to be filled with a liquid but did not experience any actuation due to the liquid escaping through the inlet (see fig. 6.4). For both forms of fluidic actuation, it is necessary to find a compliant and compatible sealant to prevent gasses and liquids from escaping for further testing with the suggested actuation methods.

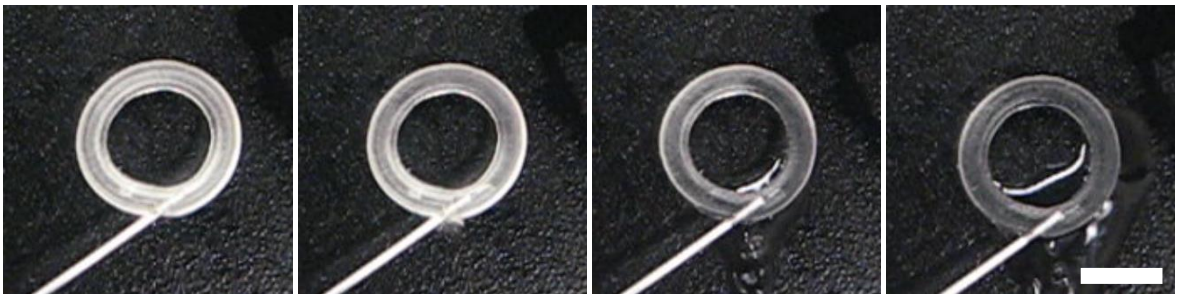

Figure 6.4 | Attempt at hydraulic actuation. Scale bar is 5 mm.

While the pneumatic actuation of a fabricated prototype is demonstrated in this thesis, future work will have to include a setup that features a secured connection between the pressure controller and the prototype. A potential solution is utilizing a similar inlet and sealing the connection between the dispensing tip and the prototype with a sealant, such as an epoxy or even small amounts of uncured PGS. However, for the final device, it is suggested that the connection between the device and a pressure controller occurs just outside of the anterior chamber of the eye. This can be achieved by printing a channel that is an extension of the internal hollow channel of the device. An intricate geometrical design is required to keep the whole channel from expanding and have actuation occur only for the radial expansion of the iris.

Printed PGSA prototypes can deform without any damage, which is essential when considering the device will have to fit through the corneal incision of around 1.8 – 3.2 mm (see section 2.1.3). The devices fabricated in this work should theoretically already fit. However, an injection needle will have to be developed specifically to allow the implantation to occur within a reasonable time to avoid increasing operative times. This injector will have to consider the tubes (either printed with the same material or a tube from a pressure controller) that will be attached to the device.

For magnetic actuation, it must be considered that up to 8 T is still safe for the human body.[67] However, an issue arises when a patient or the surgeon has, for example, a biomedical implant, which would inhibit the use of a magnetic field to 25 mT and 0.5 mT for conductive and electrically active implants, respectively. Hence, it is necessary to perform experiments to deduce the required magnetic forces to achieve radial expansion of the iris and study if that force would cause any dangers for frequently used implants and other devices that could be present in the operating room. Also, this thesis did not discuss the best magnetic actuation setup to achieve radial expansion of iris tissue. A type of electromagnetic face mask placed in a circular pattern around the eye or head of the patient could be a potential solution. However, this must be given more attention in future work.

7 Conclusions

This research aimed to provide the groundwork for designing and fabricating a soft robotic pupil expansion device. This was successfully achieved, starting with the synthesis of three biomaterials that were used to fabricate different device prototypes with a conventional molding technique. While PGS could not be used to fabricate a prototype successfully, it was used in an acrylation reaction to synthesize different PGSA inks. The synthesis process of this ink was carefully documented, which resulted in a detailed protocol that can be used to reproduce the achieved results.

PGSA ink was 3D printed, and feature sizes of around 90 µm were realized. It was also possible to rapidly fabricate device prototypes that were later used to showcase the ability to actuate pneumatically. A ring-shaped prototype exhibited a rapid increase in diameter due to its geometry, proving that the achieved material is suitable for the perceived final application. Magnetic microparticles were incorporated into the elastomeric matrix of PGSA, and it was possible to 3D print this material proving that DLP 3D printing is compatible with a magnetically active biomaterial. The stiffness of the synthesized materials, and therefore that of the devices, is in the same order as that of the human iris.

For all these materials, some of the main mechanical properties are presented and used to derive hyperelastic material model parameters utilizing COMSOL Multiphysics. An accelerated degradation assay showed that PGSA degrades slower than PGS, regardless of the fabrication method. PGSA composite showed degradation characteristics comparable with PGS, indicating that CIP particles influence the degradation of PGSA.

In conclusion, in this thesis, the synthesis of PGSA was developed from the ground up, leading to the design and fabrication of different device prototypes by means of molding techniques and 3D printing. With these prototypes, it was possible to demonstrate that the suggested types of soft actuation are functional. The achievements in this thesis not only provide the basis for a soft robotic pupil expansion device but also provides a basic understanding of a very versatile biomaterial that can be used in numerous biomedical applications.

Appendix

Protocol - Poly Glycerol Sebacate Acrylate Ink for DLP 3D Printing

Materials

Reagents

- 2-Butoxyethyl acetate (Sigma-Aldrich, cat. no. 801395)
- 2-Propanol (Honeywell, cat. no. 33539)
- 4-(Dimethylamino)pyridine (Sigma-Aldrich, cat. no. 107700)
- 4-Methoxyphenol (Sigma-Aldrich, cat. no. M18655)
- Acetone (Honeywell, cat. no. 32201)
- Acryloyl chloride (Sigma-Aldrich, cat. no. A24109)
- Demineralized water
- Dichloromethane (Sigma-Aldrich, cat. no. 270997)
- Dimethyl sulfoxide (Sigma-Aldrich, cat. no. 276855)
- Diphenyl(2,4,6-trimethylbenzoyl)phosphine oxide (Sigma-Aldrich, cat. no. 415952)
- Ethyl acetate (Sigma-Aldrich, cat. no. 319902)
- Glycerol (Sigma-Aldrich, cat. no. G7893)
- Hydrochloric acid (Sigma-Aldrich, cat. no. 320331)
- Sebacic acid (Sigma-Aldrich, cat. no. 84809)
- Sodium sulfate (Sigma-Aldrich, cat. no. 239313)
- Triethylamine (Sigma-Aldrich, cat. no. 471283)

Equipment

- Aluminum foil
- Analytical laboratory scale
- Buchner funnel
- Bump trap
- Coil condenser
- Cork flask support ring
- Dispensing tips
- Disposable laboratory spatulas
- Filter paper
- Ice cubes
- Keck joint clips
- Lab spoon
- Laboratory thermometer
- Magnetic stirrer
- Magnetic stir bar
- Magnetic stir bar retriever
- Micropipette
- Parafilm
- Refrigerator (2–8°C)
- Rotary evaporator
- Rubber stoppers
- Rubber funnel adaptor

- Rubber tubing
- Separatory funnel
- Side-arm flask
- Stirring heating mantle
- Three-neck round bottom flask
- Tweezers
- Vacuum grease
- Vacuum oven
- Weighing papers

Procedure

Chemical synthesis of PGS prepolymer

1| Clean the three-neck round bottom flask with acetone, 2-propanol, and demineralized water. Dry the flask with clean room paper as much as possible

2| Leave the three-neck round bottom flask in the oven overnight at T>80°C to remove any remaining water condensation from the flask before reactants are added.

3| Measure an equimolar amount of glycerol and sebacic acid into the dried flask. Adjust the volume of reactants to the volume of the flask. Do not fill the flask over the equator.

4| Make sure the sebacic acid is submerged in the glycerol. **! CAUTION** Any sebacic acid, not in contact with glycerol will stick to the walls of the flask and therefore not react during the polycondensation.

5| Place the round-bottom flask inside the stirring heating mantle, and add a magnetic stir bar inside the round-bottom flask

6| Use vacuum grease on the bottom end of the coil condenser and place it in the middle neck of the flask.

7| Use plastic tubing to connect the bottom lateral opening of the coil condenser with the water inlet. Connect the other (top) lateral opening of the coil condenser to the water outlet.

8| Close the two lateral necks of the flask and the top of the coil condenser with rubber stops.

9| Use a clamp holder to hold the temperature probe in place. The temperature probe should be submerged in the mixture but not touching the glass bottom. Preferably use a rubber stop with a pre-made hole for the temperature probe. If any leaks are detected, use parafilm to seal them.

10| Set the temperature of the mantle to 120°C. **! CAUTION** Make sure the temperature probe remains in the mixture at all times.

11| Begin a nitrogen purge of the flask by applying a vacuum for 2 minutes with a vacuum line and a dispensing tip. After 2 minutes, remove the vacuum line and use a nitrogen flow for 2 minutes. Plug in a dispensing tip on top of the coil condenser to provide the flask with an exhaust. Repeat this three times. **! CAUTION** Overpressure may lead to damaged glassware or propel the rubber stops.

12| Provide nitrogen flow during the duration of the polycondensation.

13| Open the water supply so that water is continuously running through the coil condenser.

14| Start the magnetic stirring at the lowest possible setting. Initially, the mixture is very viscous and hard to stir. The stirring speed may be increased later.

15| When the mixture reaches a stable temperature of 120°C, start timing the polycondensation reaction for 2 h.

16| Close off the water supply and the nitrogen line.

17| Turn off the stirring heating mantle and remove the coil condenser.

18| Remove the round bottom flask and place it on a cork flask support ring. **! CAUTION** The bottom half of the round bottom flask is very hot!

19| While the mixture is still hot, pour it into a glass beaker of sufficient volume. Cover the beaker with aluminum foil while still under the fume hood.

20| Place this beaker inside a larger beaker to transport and use it in the vacuum oven.

21| Provide holes in the aluminum foil using a sharp object.

22| Set the temperature of the vacuum oven to 120°C and place the beaker inside.

23| Turn on the vacuum pump and provide the highest vacuum level available for at least 22 h.

24| When the preferred duration of polycondensation is achieved, turn off the vacuum oven. Proceed with purging the vacuum oven with nitrogen flow.

25| The final PGS prepolymer of the chosen level of cross-linking can be retrieved from the glass beaker and stored in a refrigerator at 4 °C until further use.

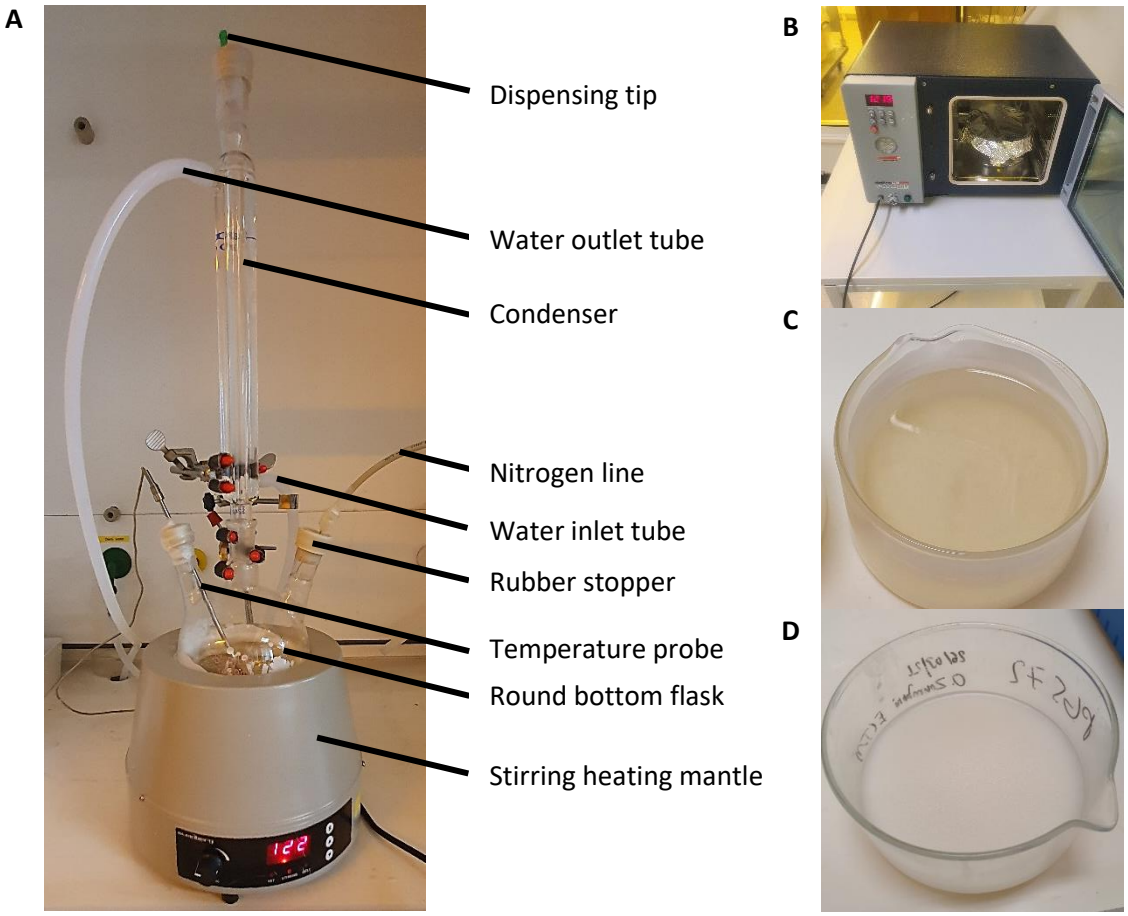

Figure 1| PGS prepolymer synthesis. (**A**) Polycondensation setup for PGS in a nitrogen environment at 120 °C. (**B**) Continuation of polycondensation reaction in a vacuum oven at 120 °C in a larger confining glass beaker. (**C**) PGS prepolymer as a yellow viscous liquid immediately after synthesis. (D) PGS prepolymer at room temperature appears as a white, solid wax-like substance.

Chemical synthesis of PGSA prepolymer

Preparation of PGS prepolymer for acrylation

26| Repeat step 1 for the flask that will be used for the PGSA prepolymer

27| PGSA prepolymer consists of a mixture of 10% (w/v) of PGS prepolymer, 0.01% (w/v) 4-(dimethylamino)pyridine, and 0.005% (w/v) 4-methoxyphenol in dichloromethane.

28| Measure, at the most, 30 g of PGS prepolymer inside the round bottom flask. The PGS prepolymer can be heated up to make it easier to measure and move the PGS prepolymer. **! CAUTION** PGS tends to prematurely cross-link in case higher volumes are used. It is not recommended, but this can be elucidated by adding more 4-methoxyphenol.

29| Add a magnetic stir bar and place the mixture on a magnetic stirrer to speed up the dissolving of the PGS prepolymer.

Acrylation of PGS prepolymer

30| Create an ice bath by pouring ice cubes and water into a beaker that can accommodate the round bottom flask.

31| Hold the round bottom flask steady using clamp holders. Make sure the part of the flask with the viscous mixture is submerged in the ice bath.

32| While stirring the mixture, provide a nitrogen flow inside the round bottom flask.
! CAUTION Keep the nitrogen flow moderate. Otherwise, the top layer of the mixture will solidify, making the next steps unnecessarily more difficult.

33| Leave the mixture for 10 min to stir in the ice bath under nitrogen flow until it reaches 0 °C. Use a laboratory thermometer to check the temperature of the mixture.

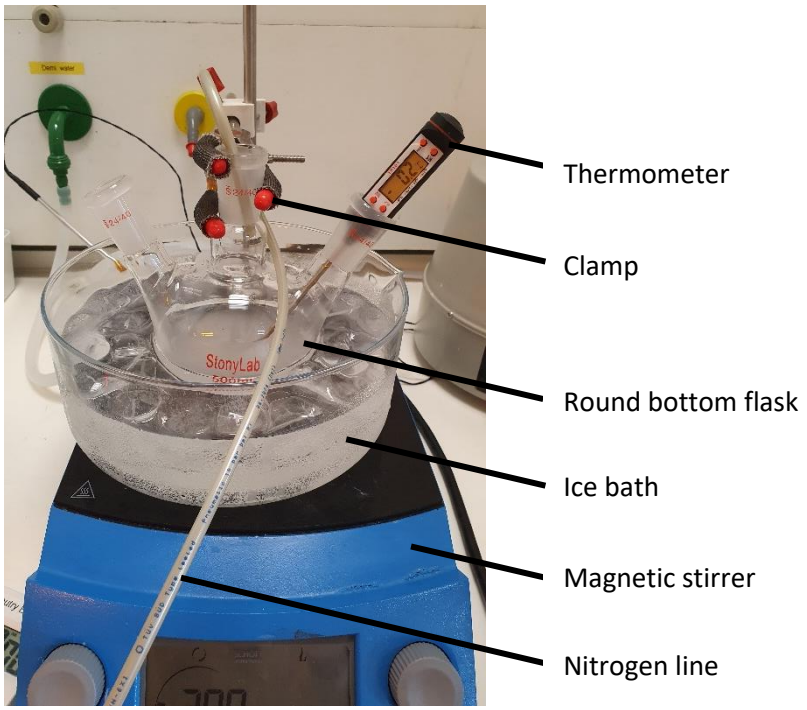

Figure 2| Preparation for acrylation of PGS. Dissolved PGS in a round bottom flask being stirred in an ice bath under nitrogen flow.

34| Before adding the acrylation chemicals, wrap the round bottom flask in aluminum foil and turn off the lights of the fume hood.

35| Remove the nitrogen flow and place the aluminum foil-covered round bottom flask outside the ice bath, on a magnetic stirrer, or in a stirring mantle.

36| Depending on the required degree of acrylation, measure molar equivalents of acryloyl chloride and triethylamine in two separate containers. Always use the analytical lab scale under the fume hood. **! CAUTION** Do not, under any circumstance, mix these two reagents outside the main flask or without adding a solvent.

37| Under the exclusion of light, add triethylamine to the round bottom flask.

38| Under the exclusion of light, slowly add acryloyl chloride to the round-bottom flask. Perform this addition drop-wise and ensure the mixture is being stirred continuously. **! CAUTION** Be wary of the fumes from the reaction.

39| Leave the mixture to rest at room temperature for 24 h while it is being stirred.

Post-Processing and Purification of PGSA prepolymer

40| While the mixture is still stirring, add the same amount of 4-methoxyphenol added to the mixture during step 29.

41| Fill the water bath of the rotary evaporator with an adequate amount of water and heat it to 40 °C.

42| Clean a magnetic stir bar retriever with acetone, 2-propanol, and demineralized water. Dry it as much as possible with cleanroom paper. Use it to retrieve the magnetic stir bar inside of the flask.

43| Pour the mixture into the rotary flask while it is on a cork flask supporting ring. Use a clean glass funnel if necessary.

44| Apply vacuum grease to the rotary evaporator flask holder and place the bump trap on it. Use a keck joint clip in addition to the existing metal clip available on the rotary evaporator.

45| Apply vacuum grease to the other end of the bump trap and attach the rotary flask to it with a keck joint clip.

46| Apply a vacuum of 450 mbar and close the filling valve. Make sure that at least half of the flask is submerged in the water bath.

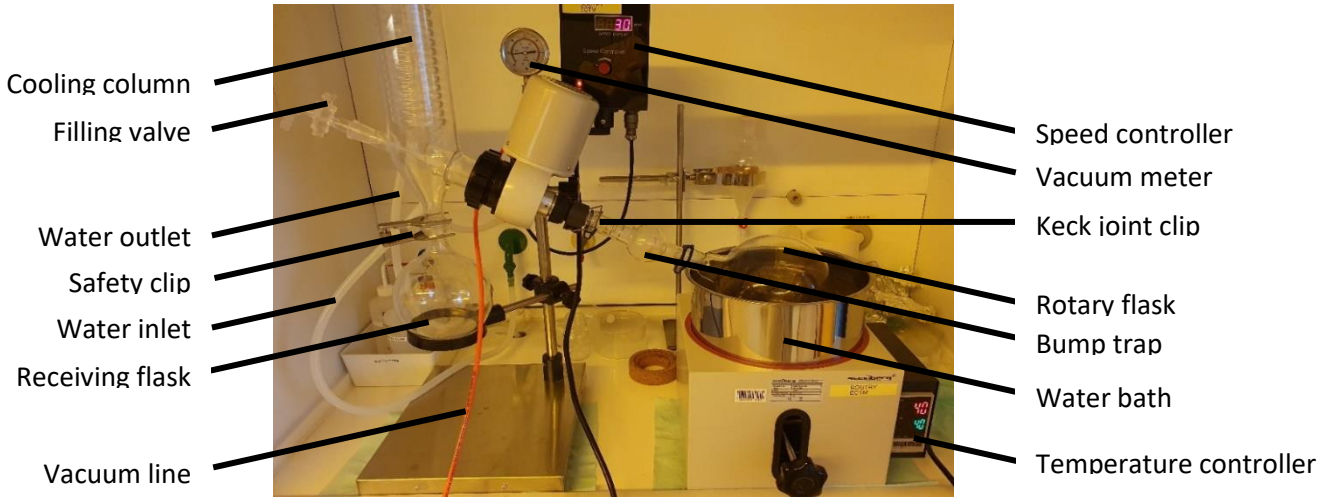

Figure 3| Rotary evaporation to remove solvents. The rotary evaporation setup for the removal of dichloromethane and ethyl acetate during the synthesis of PGSA.

47| Make sure water flows in and out of the evaporation column of the rotary evaporator and start rotating the flask. It is not necessary to go over 60 revolutions per minute. 15-30 r/min is optimal for this step.
48| Keep evaporating dichloromethane until a viscous liquid is left inside the flask.
49| In reverse order, remove the flask and place it on a cork flask supporting ring.
50| Add an equivalent volume of Ethyl acetate to the viscous mixture to dissolve the mixture.
51| Prepare a clean vacuum filtration setup. Start by placing the Buchner funnel with a rubber funnel adaptor on top of a side-arm flask.
52| Place a filter paper inside the Buchner funnel and use a plastic tube to attach a vacuum line to the side-arm flask.
53| Open the vacuum valve as much as possible and adjust the position of the filter paper, sealing all the holes as much surface of the Buchner funnel as possible.
54| With the vacuum applied, carefully pour the dissolved mixture into the Buchner funnel. The filtration will proceed increasingly slower because the triethylamine salts will aggregate on the filter paper.
55| The mixture in the side-arm flask will be much more transparent with the bulk of the triethylamine salts left in the Buchner funnel.
56| Repeat this step as many times as necessary to reach a clear solution. **! CAUTION** More triethylamine salts will develop during the acrylation process for a higher degree of acrylation. This step will be more challenging to perform with a higher degree of acrylation. In that case, make sure to replace the filter paper sooner.
57| Pour the clear mixture into a separation funnel and note the volume. **! CAUTION** Make sure the separation funnel is closed.
58| Measure 30 mM hydrochloric acid solution diluted in demineralized water. A volume equivalent to the mixture is advised but use at least 100 mL of hydrochloric acid solution. Add it to the mixture and note the total volume.
59| Put on the separation funnel lid. Proceed to shake the two components vigorously until they are well-mixed.
60| Cover the separation funnel with aluminum foil to avoid premature photocuring.
61| Remove the separation funnel lid and let the mixture rest until clear organic and aqueous layers are visible in the separation funnel. **! CAUTION** It takes several hours for this split between the layers to become discernable, hence leaving it overnight and away from light is optimal.
62| Depending on the duration of cross-linking of PGS prepolymer and the degree of acrylation, an aqueous layer will either be on top or at the bottom of the organic layer. Note the volume of each separate layer.
63| To determine which layer is the organic layer, add a known volume of demineralized water to the separation funnel. After a while, it becomes apparent which layer gained that known volume of demineralized water. That layer is the aqueous layer and can be disposed of.
64| Pour the remaining organic mixture into a beaker and add small amounts of sodium sulfate. Use a clean lab spoon to stir the mixture carefully.
65| Sodium sulfate will drop to the bottom, and the organic compounds can be poured back into the rotary flask. Based on how well the aqueous compounds were disposed of, it might be necessary to repeat this step several times. **! CAUTION** Do not use too much sodium sulfate for each repetition; the more sodium sulfate is used, the less PGSA will be left inside of the mixture.

66| Repeat steps 42 and 44-49 with the following adjustment: the solvent is ethyl acetate and requires a pressure of 99 mbar. With ethyl acetate, it is visible when it is done; there will be no more liquids entering the receiving flask.

67| The remaining mixture in the rotary flask is PGSA. Collect as much PGSA as possible by repeatedly heating the flask to 40 °C to make it less viscous.

68| Keep the PGSA prepolymer protected from light and store it at 4 °C until further use.

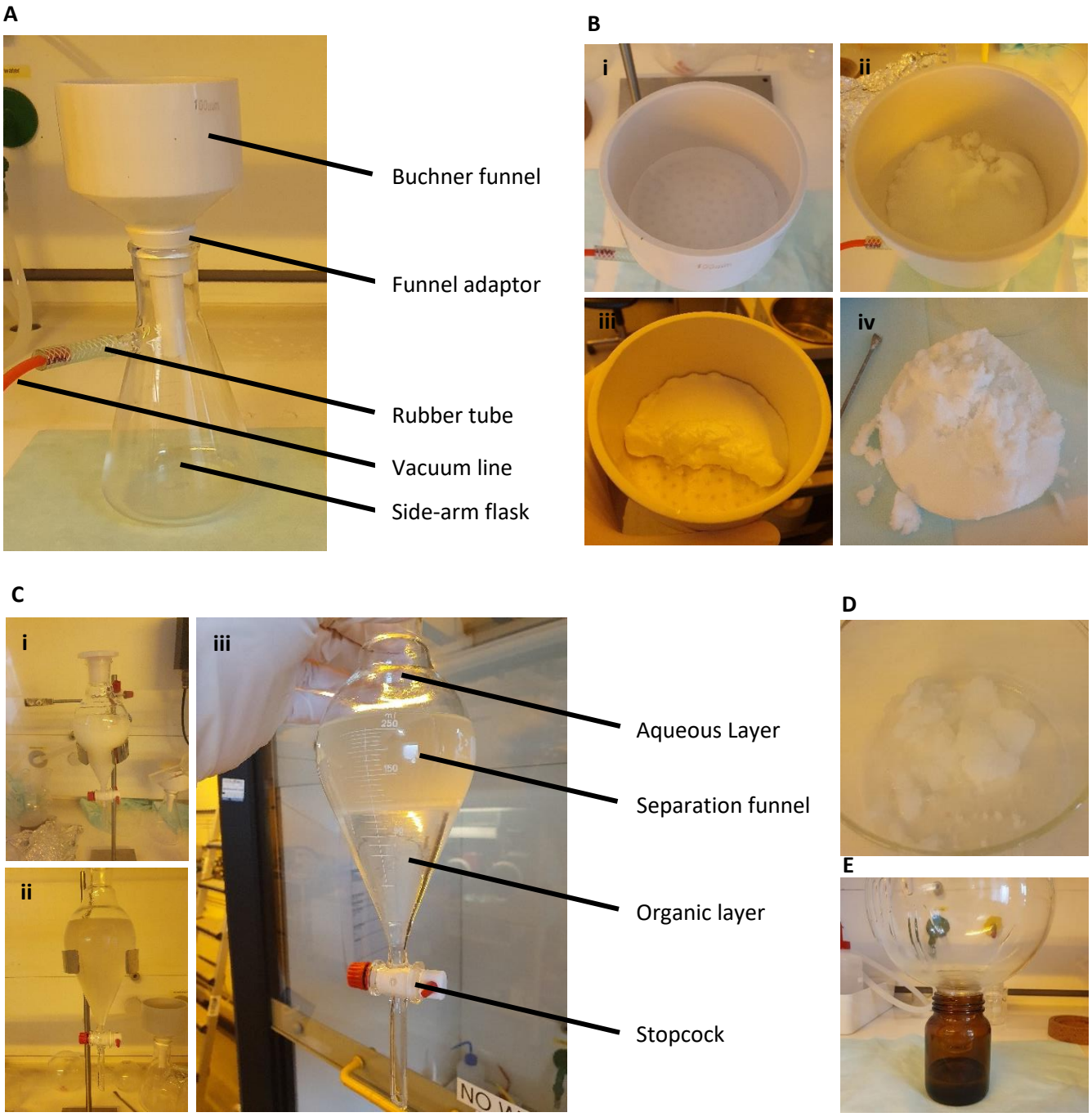

Figure 4| Washing steps of PGSA. (**A**) Vacuum filtration setup. (**B**) The different status inside the Buchner funnel. i, A clean filter paper placed in the funnel. ii, Regular amount of triethylamine salts after the first filtration step. iii, High amounts of triethylamine salts due to a high degree of acrylation, filtration is very slow. iv, Removed filter paper before disposal. (**C**) timelapse of hydrochloric acid wash. i, After adding a hydrochloric acid solution, the mixture turns white. ii, After approximately 1 h it turns back to the regular yellowish color. iii, The following day, two clearly visible layers are discernable. (**D**) Remaining sodium sulfate in a glass beaker after pouring the mixture back into the rotary flask. (**E**) Final retrieval of viscous PGSA prepolymer.

Synthesis of PGSA Ink for 3D printing

69| For PGSA ink, 1 wt% diphenyl(2,4,6-trimethylbenzoyl)phosphine oxide is added as a photoinitiator to make it compatible with digital light processing (DLP) printing.

70| Add the desired amount of PGSA prepolymer in a clean container of choice.

71| Calculate 1 wt% of this weight and add it to the container under the exclusion of light.

72| Add a magnetic stir bar and place the container on a magnetic stirrer for 1 h.

73| 2-Butoxyethyl acetate and dimethyl sulfoxide can be added to the PGSA ink to control the viscosity. **! CAUTION** There is a range of optimal viscosities for DLP printing. The viscosity of PGSA will vary significantly based on the desired degree of acrylation.

Bibliography

1. Johns Hopkins Medicine. Common Surgical Procedures. *https://www.hopkinsmedicine.org/health/treatment-tests-and-therapies/common-surgical-procedures* (2022).

2. Surgical operations and procedures statistics - Statistics Explained. *https://ec.europa.eu/eurostat/statistics-explained/index.php?title=Surgical_operations_and_procedures_statistics* (2021).

3. Micieli, J. A. & Arshinoff, S. A. Cataract surgery. *CMAJ* **183**, 1621 (2011).

4. Bourne, R. R. A. *et al.* Causes of blindness and vision impairment in 2020 and trends over 30 years, and prevalence of avoidable blindness in relation to VISION 2020: The Right to Sight: An analysis for the Global Burden of Disease Study. *Lancet Glob Health* **9**, e144–e160 (2021).

5. Leffler, C. T., Hadi, T. M., Udupa, A., Schwartz, S. G. & Schwartz, D. A medieval fallacy: The crystalline lens in the center of the eye. *Clinical Ophthalmology* vol. 10 649–662 Preprint at https://doi.org/10.2147/OPTH.S100708 (2016).

6. Davis, G. *The Evolution of Cataract Surgery*. (2016).

7. Jaimes-Nájera, A., Gómez-Correa, J. E., Coello, V., Pierscionek, B. K. & Chávez-Cerda, S. Single function crystalline lens capable of mimicking ciliary body accommodation. *Biomed Opt Express* **11**, 3699 (2020).

8. Roskamp, K. W., Paulson, C. N., Brubaker, W. D. & Martin, R. W. Function and Aggregation in Structural Eye Lens Crystallins. *Acc Chem Res* **53**, 863–874 (2020).

9. Henry Marriner. Human Eye Png - Eye Ball Cross Section, Transparent Png. *https://www.pngitem.com/middle/iTxRbTm_human-eye-png-eye-ball-cross-section-transparent/* (2019).

10. Bhat, S. P. *Crystallins, genes and cataract*. *genes Progress in Drug Research* vol. 60 (2003).

11. Bobrow JC, B. T. J. S. *Lens and cataract American Academy of Ophthalmology*.

12. Liu, Y. C., Wilkins, M., Kim, T., Malyugin, B. & Mehta, J. S. Cataracts. *The Lancet* vol. 390 600–612 Preprint at https://doi.org/10.1016/S0140-6736(17)30544-5 (2017).

13. Lee Ann Remington OD, M. F. in C. A. and P. of the V. S. (Third E. 2012. lens structure 2.

14. Clark JI. Development and maintenance of lens transparency. In Albert DM, Jakobiec FA, editors: Principles and practice of ophthalmology Philadelphia, 1994, Saunders, p 114.

15. Vinson, J. A. Oxidative stress in cataracts. *Pathophysiology* vol. 13 151–162 Preprint at https://doi.org/10.1016/j.pathophys.2006.05.006 (2006).

16. Malyugin, B. Cataract surgery in small pupils. *Indian Journal of Ophthalmology* vol. 65 1323–1328 Preprint at https://doi.org/10.4103/ijo.IJO_800_17 (2017).

17. Borkenstein, A. F., Borkenstein, E. M. & Malyugin, B. Ophthalmic Viscosurgical Devices (OVDs) in Challenging Cases: a Review. *Ophthalmology and Therapy* vol. 10 831–843 Preprint at https://doi.org/10.1007/s40123-021-00403-9 (2021).

18. Harshal Wasnik *et al.* A Comprehensive Review of Molecular Biology and Genetics of Cataract. *International Journal for Research in Applied Sciences and Biotechnology* **8**, 11–20 (2021).

19. Leffler, C. T., Klebanov, A., Samara, W. A. & Grzybowski, A. The history of cataract surgery: from couching to phacoemulsification. *Ann Transl Med* **8**, 1551–1551 (2020).

20. Roy, P. N., Mehra, K. S. & Deshpande, P. J. *Cataract surgery performed before 800 B.C. Brit. J. Ophthal* vol. 59.

21. Isawumi, M. A., Kolawole, O. U. & Hassan, M. B. *COUCHING TECHNIQUES FOR CATARACT TREATMENT IN OSOGBO, SOUTH WEST NIGERIA*. vol. 47 (2013).

22. Wetzig, P. C., Thatcher, D. B. & Christiansen, J. M. *THE INTRACAPSULAR VERSUS THE EXTRACAPSULAR CATARACT TECHNIQUE IN RELATIONSHIP TO RETINAL PROBLEMS*.

23. Singh, K., Misbah, A., Saluja, P. & Singh, A. Review of manual small-incision cataract surgery. *Indian Journal of Ophthalmology* vol. 65 1281–1288 Preprint at https://doi.org/10.4103/ijo.IJO_863_17 (2017).

24. Bernhisel, A. & Pettey, J. Manual small incision cataract surgery. *Curr Opin Ophthalmol* **31**, 74–79 (2020).

25. Publications Pvt Ltd, M. *Symposium Viscoexpression technique in manual small incision cataract surgery Nikhil S Gokhale*.

26. Chen, X., Xu, J., Chen, X. & Yao, K. Cataract: Advances in surgery and whether surgery remains the only treatment in future. *Advances in Ophthalmology Practice and Research* **1**, 100008 (2021).

27. Melancia, D., Pinto, L. A. & Marques-Neves, C. Cataract surgery and intraocular pressure. *Ophthalmic Research* vol. 53 141–148 Preprint at https://doi.org/10.1159/000377635 (2015).

28. definitivehc. https://www.definitivehc.com/resources/healthcare-insights/most-common-surgical-procedures-ascs. (2022).

29. Grzybowski, A. & Kanclerz, P. Methods for achieving adequate pupil size in cataract surgery. *Curr Opin Ophthalmol* **31**, 33–42 (2020).

30. Dupps, W. J. Mydriatic strategies for cataract surgery: optimizing efficacy and cost. *Journal of Cataract and Refractive Surgery* vol. 47 977–978 Preprint at https://doi.org/10.1097/j.jcrs.0000000000000726 (2021).

31. Hashemi, H., Seyedian, M. A. & Mohammadpour, M. Small pupil and cataract surgery. *Current Opinion in Ophthalmology* vol. 26 3–9 Preprint at https://doi.org/10.1097/ICU.0000000000000116 (2015).

32. Uy, H. S., Cruz, F. M. & Kenyon, K. R. Efficacy of a hinged pupil expansion device in small pupil cataract surgery. *Indian J Ophthalmol* **69**, 2688–2693 (2021).

33. Salviat, F. *et al.* Evaluation of a uniplanar pupil expansion ring in small-pupil cataract surgery: a feasibility study. *Int Ophthalmol* **42**, 489–496 (2022).

34. Chang, D. F. *et al.* ASCRS White Paper: Clinical review of intraoperative floppy-iris syndrome. *J Cataract Refract Surg* **34**, 2153–2162 (2008).

35. Horvath, K. & Vultur, F. Correlation between urological alpha1-AR antagonist medication and changed intraoperative iris behavior. *Int Ophthalmol* **31**, 99–104 (2011).

36. Ariga, M., Nivean, M. & Utkarsha, P. Pseudoexfoliation syndrome. *Journal of Current Glaucoma Practice* vol. 7 118–120 Preprint at https://doi.org/10.5005/jp-journals-10008-1148 (2013).

37. Halkiadakis, I. *et al.* Causes and management of small pupil in patients with cataract. *Oman J Ophthalmol* **10**, 220–224 (2017).

38. Balal, S. *et al.* Management and outcomes of the small pupil in cataract surgery: iris hooks, Malyugin ring or phenylephrine? *Eye (Basingstoke)* **35**, 2714–2718 (2021).

39. Hashemi, H., Mohammadpour, M., Jabbarvand, M., Nezamdoost, Z. & Ghadimi, H. Incidence of and risk factors for vitreous loss in resident-performed phacoemulsification surgery. *J Cataract Refract Surg* **39**, 1377–1382 (2013).

40. Bouffard, M. A. The Pupil. *CONTINUUM: Lifelong Learning in Neurology* **25**, 1194–1214 (2019).

41. Thomas Moazed, K. *Iris: Understanding the Essentials*. (2020).

42. Melgar, M., Yee, ; & Buchan, J. LSHTM Research Online. *Community Eye Health Journal* 84–85.

43. Fu, H. *et al.* Angle-Closure Detection in Anterior Segment OCT based on Multi-Level Deep Network. (2019) doi:10.1109/TCYB.2019.2897162.

44. Park, K. S. *et al.* Effects of miosis on anterior chamber structure in glaucoma implant surgery. *J Clin Med* **10**, 1–10 (2021).

45. Alpa S. Patel, M. D. & Koushik Tripathy. Pupil Expansion Devices and Mechanical Stretching of the Pupil. https://eyewiki.aao.org/Pupil_Expansion_Devices_and_Mechanical_Stretching_of_the_Pupil (2021).

46. beye. Compare Iris Retractors. *https://www.beye.com/compare/iris-retractors*.

47. Wang, J. da *et al.* Comparison of different pupil dilatation methods for phacoemulsification in eyes with a small pupil. *BMC Ophthalmol* **22**, (2022).

48. Nderitu, P. & Ursell, P. Iris hooks versus a pupil expansion ring: Operating times, complications, and visual acuity outcomes in small pupil cases. *J Cataract Refract Surg* **45**, 167–173 (2019).

49. Wilczynski, M., Wierzchowski, T., Synder, A. & Omulecki, W. Results of phacoemulsification with Malyugin Ring in comparison with manual iris stretching with hooks in eyes with narrow pupil. *Eur J Ophthalmol* **23**, 196–201 (2013).

50. Tian, J. J., Garcia, G. A., Karanjia, R. & Lu, K. L. Comparison of 2 pupil expansion devices for small-pupil cataract surgery. *J Cataract Refract Surg* **42**, 1235–1237 (2016).

51. Tan, R. K. Y., Wang, X., Perera, S. A. & Girard, M. J. A. Numerical stress analysis of the iris tissue induced by pupil expansion: Comparison of commercial devices. *PLoS One* **13**, (2018).

52. Lockington, D. *et al.* Modelling floppy iris syndrome and the impact of pupil size and ring devices on iris displacement. *Eye (Basingstoke)* **34**, 2227–2234 (2020).

53. Hawkes, E. W., Majidi, C. & Tolley, M. T. *Hard questions for soft robotics*. *Sci. Robot* vol. 6 https://www.science.org (2021).

54. Bao, G. *et al.* Soft robotics: Academic insights and perspectives through bibliometric analysis. *Soft Robotics* vol. 5 229–241 Preprint at https://doi.org/10.1089/soro.2017.0135 (2018).

55. Lee, C. *et al.* Soft robot review. *International Journal of Control, Automation and Systems* vol. 15 3–15 Preprint at https://doi.org/10.1007/s12555-016-0462-3 (2017).

56. El-Atab, N. *et al.* Soft Actuators for Soft Robotic Applications: A Review. *Advanced Intelligent Systems* **2**, 2000128 (2020).

57. Boyraz, P., Runge, G. & Raatz, A. An overview of novel actuators for soft robotics. *High-Throughput* vol. 7 Preprint at https://doi.org/10.3390/act7030048 (2018).

58. Dou, W. *et al.* Soft Robotic Manipulators: Designs, Actuation, Stiffness Tuning, and Sensing. *Advanced Materials Technologies* vol. 6 Preprint at https://doi.org/10.1002/admt.202100018 (2021).

59. Coyle, S., Majidi, C., LeDuc, P. & Hsia, K. J. Bio-inspired soft robotics: Material selection, actuation, and design. *Extreme Mechanics Letters* vol. 22 51–59 Preprint at https://doi.org/10.1016/j.eml.2018.05.003 (2018).

60. Guo, Y., Liu, L., Liu, Y. & Leng, J. Review of Dielectric Elastomer Actuators and Their Applications in Soft Robots. *Advanced Intelligent Systems* **3**, 2000282 (2021).

61. Gu, G. Y., Zhu, J., Zhu, L. M. & Zhu, X. A survey on dielectric elastomer actuators for soft robots. *Bioinspiration and Biomimetics* vol. 12 Preprint at https://doi.org/10.1088/1748-3190/12/1/011003 (2017).

62. Li, M., Pal, A., Aghakhani, A., Pena-Francesch, A. & Sitti, M. Soft actuators for real-world applications. *Nature Reviews Materials* vol. 7 235–249 Preprint at https://doi.org/10.1038/s41578-021-00389-7 (2022).

63. Goh, G. D. *et al.* 3D Printing of Robotic Soft Grippers: Toward Smart Actuation and Sensing. *Advanced Materials Technologies* Preprint at https://doi.org/10.1002/admt.202101672 (2022).

64. Ebrahimi, N. *et al.* Magnetic Actuation Methods in Bio/Soft Robotics. *Advanced Functional Materials* vol. 31 Preprint at https://doi.org/10.1002/adfm.202005137 (2021).

65. Mishra, S. R., Dickey, M. D., Velev, O. D. & Tracy, J. B. Selective and directional actuation of elastomer films using chained magnetic nanoparticles. *Nanoscale* **8**, 1309–1313 (2016).

66. Hines, L., Petersen, K., Lum, G. Z. & Sitti, M. Soft Actuators for Small-Scale Robotics. *Advanced Materials* vol. 29 Preprint at https://doi.org/10.1002/adma.201603483 (2017).

67. Yang, Z. & Zhang, L. Magnetic Actuation Systems for Miniature Robots: A Review. *Advanced Intelligent Systems* **2**, 2000082 (2020).

68. Xu, T., Yu, J., Yan, X., Choi, H. & Zhang, L. Magnetic actuation based motion control for microrobots: An overview. *Micromachines* vol. 6 1346–1364 Preprint at https://doi.org/10.3390/mi6091346 (2015).

69. Song, H. *et al.* Reprogrammable Ferromagnetic Domains for Reconfigurable Soft Magnetic Actuators. *Nano Lett* **20**, 5185–5192 (2020).

70. Mohd Jani, J., Leary, M., Subic, A. & Gibson, M. A. A review of shape memory alloy research, applications and opportunities. *Materials and Design* vol. 56 1078–1113 Preprint at https://doi.org/10.1016/j.matdes.2013.11.084 (2014).

71. Kirillova, A. & Ionov, L. Shape-changing polymers for biomedical applications. *Journal of Materials Chemistry B* vol. 7 1597–1624 Preprint at https://doi.org/10.1039/c8tb02579g (2019).

72. Ula, S. W. *et al.* Liquid crystal elastomers: An introduction and review of emerging technologies. *Liquid Crystals Reviews* vol. 6 78–107 Preprint at https://doi.org/10.1080/21680396.2018.1530155 (2018).

73. Kularatne, R. S., Kim, H., Boothby, J. M. & Ware, T. H. Liquid crystal elastomer actuators: Synthesis, alignment, and applications. *Journal of Polymer Science, Part B: Polymer Physics* vol. 55 395–411 Preprint at https://doi.org/10.1002/polb.24287 (2017).

74. Traugutt, N. A. *et al.* Liquid-Crystal-Elastomer-Based Dissipative Structures by Digital Light Processing 3D Printing. *Advanced Materials* **32**, (2020).

75. Malachowski, K. *et al.* Stimuli-Responsive Theragrippers for Chemomechanical Controlled Release. *Angewandte Chemie* **126**, 8183–8187 (2014).

76. Rosenbluth, R. F. & Fatt, I. *Temperature Measurements in the Eye*. Exp. Eye Res* vol. 25 (1977).

77. Zhu, Q. *et al.* Near infrared (NIR) light therapy of eye diseases: A review. *International Journal of Medical Sciences* vol. 18 109–119 Preprint at https://doi.org/10.7150/ijms.52980 (2021).

78. Chou, C.-P. & Hannaford, B. *rement and ding of McKibben Pneumatic Artificial Muscles*. *IEEE TRANSACTIONS ON ROBOTICS AND AUTOMATION* vol. 12 (1996).

79. Walker, J. *et al.* Soft robotics: A review of recent developments of pneumatic soft actuators. *Actuators* **9**, (2020).

80. Mosadegh, B. *et al.* Pneumatic networks for soft robotics that actuate rapidly. *Adv Funct Mater* **24**, 2163–2170 (2014).

81. Aydin, Y. O., Molnar, J. L., Goldman, D. I. & Hammond, F. L. Design of a soft robophysical earthworm model. in *2018 IEEE International Conference on Soft Robotics, RoboSoft 2018* 83–87 (Institute of Electrical and Electronics Engineers Inc., 2018). doi:10.1109/ROBOSOFT.2018.8404901.

82. Takemura, K., Yokota, S. & Edamura, K. A micro artificial muscle actuator using electro-conjugate fluid. in *Proceedings - IEEE International Conference on Robotics and Automation* vol. 2005 532–537 (2005).

83. Zhao, Q. *et al.* An instant multi-responsive porous polymer actuator driven by solvent molecule sorption. *Nat Commun* **5**, (2014).

84. Bettinger, C. J. Biodegradable Elastomers for Tissue Engineering and Cell-Biomaterial Interactions. *Macromolecular Bioscience* vol. 11 467–482 Preprint at https://doi.org/10.1002/mabi.201000397 (2011).

85. Wang, Y., Sheppard, B. J. & Langer, R. Poly(glycerol sebacate) - A novel biodegradable elastomer for tissue engineering. in *Materials Research Society Symposium - Proceedings* vol. 724 223–227 (Materials Research Society, 2002).

86. Chen, S. *et al.* Biodegradable Elastomers and Gels for Elastic Electronics. *Advanced Science* vol. 9 Preprint at https://doi.org/10.1002/advs.202105146 (2022).

87. Ulery, B. D., Nair, L. S. & Laurencin, C. T. Biomedical applications of biodegradable polymers. *Journal of Polymer Science, Part B: Polymer Physics* vol. 49 832–864 Preprint at https://doi.org/10.1002/polb.22259 (2011).

88. Turner, B., Ramesh, S., Menegatti, S. & Daniele, M. Resorbable elastomers for implantable medical devices: highlights and applications. *Polymer International* vol. 71 552–561 Preprint at https://doi.org/10.1002/pi.6349 (2022).

89. Wang, Y., Ameer, G. A., Sheppard, B. J. & Langer, R. *A tough biodegradable elastomer*. http://biotech.nature.com (2002).

90. Ye, S. *et al.* In vivo non-contact measurement of human iris elasticity by optical coherence elastography. *J Biophotonics* **14**, (2021).

91. Goh, G. D. *et al.* 3D Printing of Robotic Soft Grippers: Toward Smart Actuation and Sensing. *Advanced Materials Technologies* Preprint at https://doi.org/10.1002/admt.202101672 (2022).

92. Zhalmuratova, D. & Chung, H. J. Reinforced Gels and Elastomers for Biomedical and Soft Robotics Applications. *ACS Applied Polymer Materials* vol. 2 1073–1091 Preprint at https://doi.org/10.1021/acsapm.9b01078 (2020).

93. Majidi, C. Soft-Matter Engineering for Soft Robotics. *Adv Mater Technol* **4**, (2019).

94. Chandan Kumar. Fitting Measured Data to Different Hyperelastic Material Models. *https://www.comsol.com/blogs/fitting-measured-data-to-different-hyperelastic-material-models/* (2015).

95. Shahzad, M., Kamran, A., Siddiqui, M. Z. & Farhan, M. Mechanical characterization and FE modelling of a hyperelastic material. *Materials Research* **18**, 918–924 (2015).

96. Vogt, L., Ruther, F., Salehi, S. & Boccaccini, A. R. Poly(Glycerol Sebacate) in Biomedical Applications—A Review of the Recent Literature. *Advanced Healthcare Materials* vol. 10 Preprint at https://doi.org/10.1002/adhm.202002026 (2021).

97. Zhang, Z., Ortiz, O., Goyal, R. & Kohn, J. Biodegradable Polymers. in *Handbook of Polymer Applications in Medicine and Medical Devices* 303–335 (Elsevier Inc., 2014). doi:10.1016/B978-0-323-22805-3.00013-X.

98. Held, M. *et al.* Soft Electronic Platforms Combining Elastomeric Stretchability and Biodegradability. *Adv Sustain Syst* **6**, (2022).

99. Ge, Q., Jian, B. & Li, H. Shaping soft materials via digital light processing-based 3D printing: A review. *Forces in Mechanics* vol. 6 Preprint at https://doi.org/10.1016/j.finmec.2022.100074 (2022).

100. Quan, H. *et al.* Photo-curing 3D printing technique and its challenges. *Bioactive Materials* vol. 5 110–115 Preprint at https://doi.org/10.1016/j.bioactmat.2019.12.003 (2020).

101. Ji, Z. *et al.* 3D Printing of Photocuring Elastomers with Excellent Mechanical Strength and Resilience. *Macromol Rapid Commun* **40**, (2019).

102. Bao, Y., Paunović, N. & Leroux, J. C. Challenges and Opportunities in 3D Printing of Biodegradable Medical Devices by Emerging Photopolymerization Techniques. *Adv Funct Mater* **32**, (2022).

103. Cai, W. & Liu, L. Shape-memory effect of poly (glycerol-sebacate) elastomer. *Mater Lett* **62**, 2171–2173 (2008).

104. Boutry, C. M. *et al.* A stretchable and biodegradable strain and pressure sensor for orthopaedic application. *Nat Electron* **1**, 314–321 (2018).

105. Yang, X., Li, L., Yang, D., Nie, J. & Ma, G. Electrospun Core–Shell Fibrous 2D Scaffold with Biocompatible Poly(Glycerol Sebacate) and Poly-l-Lactic Acid for Wound Healing. *Advanced Fiber Materials* **2**, 105–117 (2020).

106. Radisic, M. *et al.* Pre-treatment of synthetic elastomeric scaffolds by cardiac fibroblasts improves engineered heart tissue. *J Biomed Mater Res A* **86**, 713–724 (2008).

107. Rai, R., Tallawi, M., Grigore, A. & Boccaccini, A. R. Synthesis, properties and biomedical applications of poly(glycerol sebacate) (PGS): A review. *Progress in Polymer Science* vol. 37 1051–1078 Preprint at https://doi.org/10.1016/j.progpolymsci.2012.02.001 (2012).

108. Yeh, Y. C., Ouyang, L., Highley, C. B. & Burdick, J. A. Norbornene-modified poly(glycerol sebacate) as a photocurable and biodegradable elastomer. *Polym Chem* **8**, 5091–5099 (2017).

109. Nijst, C. L. E. *et al.* Synthesis and characterization of photocurable elastomers from poly(glycerol-co-sebacate). *Biomacromolecules* **8**, 3067–3073 (2007).

110. Chen, J. Y. *et al.* Study of physical and degradation properties of 3D-printed biodegradable, photocurable copolymers, PGSA-co-PEGDA and PGSA-co-PCLDA. *Polymers (Basel)* **10**, (2018).

111. Yeh, Y. C., Highley, C. B., Ouyang, L. & Burdick, J. A. 3D printing of photocurable poly(glycerol sebacate) elastomers. *Biofabrication* **8**, (2016).

112. Hartmann, F., Baumgartner, M. & Kaltenbrunner, M. Becoming Sustainable, The New Frontier in Soft Robotics. *Advanced Materials* vol. 33 Preprint at https://doi.org/10.1002/adma.202004413 (2021).

113. Rueben, J., Walker, S., Huhn, S., Simonsen, J. & Mengüç, Y. Developing a UV-Curable, Environmentally Benign and Degradable Elastomer for Soft Robotics. in *MRS Advances* vol. 3 1551–1556 (Materials Research Society, 2018).

114. Singh, D. *et al.* Additive manufactured biodegradable poly(glycerol sebacate methacrylate) nerve guidance conduits. *Acta Biomater* **78**, 48–63 (2018).

115. Rueben, J. *Synthesis and Characterization of Biodegradable, Photocuring Elastomers for Soft Robotics Applications*.

116. Wang, C. C., Chen, J. Y. & Wang, J. The selection of photoinitiators for photopolymerization of biodegradable polymers and its application in digital light processing additive manufacturing. *J Biomed Mater Res A* **110**, 204–216 (2022).

117. Teng, C. L. *et al.* Design of photocurable, biodegradable scaffolds for liver lobule regeneration via digital light process-additive manufacturing. *Biofabrication* **12**, (2020).

118. Wang, P. *et al.* 3D Printing of a Biocompatible Double Network Elastomer with Digital Control of Mechanical Properties. *Adv Funct Mater* **30**, (2020).

119. Chen, J. Y. *et al.* Study of physical and degradation properties of 3D-printed biodegradable, photocurable copolymers, PGSA-co-PEGDA and PGSA-co-PCLDA. *Polymers (Basel)* **10**, (2018).

120. Chang, C. T. *et al.* Dual-functional antibiofilm polymer composite for biodegradable medical devices. *Materials Science and Engineering C* **123**, (2021).

121. Wu, Y. L. *et al.* Three-Dimensional Printing of Poly(glycerol sebacate) Acrylate Scaffolds via Digital Light Processing. *ACS Appl Bio Mater* **3**, 7575–7588 (2020).

122. Ifkovits, J. L., Padera, R. F. & Burdick, J. A. Biodegradable and radically polymerized elastomers with enhanced processing capabilities. *Biomedical Materials* **3**, (2008).

123. Pawar, A. A. *et al.* High-performance 3D printing of hydrogels by water-dispersible photoinitiator nanoparticles. *Sci Adv* **2**, (2016).

124. Park, H. K., Shin, M., Kim, B., Park, J. W. & Lee, H. A visible light-curable yet visible wavelength-transparent resin for stereolithography 3D printing. *NPG Asia Mater* **10**, 82–89 (2018).

125. Singh, J., Kaur, T., Singh, N. & Pandey, P. M. Biological and mechanical characterization of biodegradable carbonyl iron powder/polycaprolactone composite material fabricated using three-dimensional printing for cardiovascular stent application. *Proc Inst Mech Eng H* **234**, 975–987 (2020).

126. Asiga. https://www.asiga.com/products/printers/max_series/max_x/. *Asiga Max X* (2022).

127. Wang, P. *et al.* 3D Printing of a Biocompatible Double Network Elastomer with Digital Control of Mechanical Properties. *Adv Funct Mater* **30**, (2020).

128. Yang, J., Webb, A. R., Pickerill, S. J., Hageman, G. & Ameer, G. A. Synthesis and evaluation of poly(diol citrate) biodegradable elastomers. *Biomaterials* **27**, 1889–1898 (2006).

129. Nagata, M., Machida, T., Sakai, W. & Tsutsumi, N. *Synthesis, Characterization, and Enzymatic Degradation Studies on Novel Network Aliphatic Polyesters*. https://pubs.acs.org/sharingguidelines (1998).

130. Perin, G. B. & Felisberti, M. I. Enzymatic Synthesis of Poly(glycerol sebacate): Kinetics, Chain Growth, and Branching Behavior. *Macromolecules* **53**, 7925–7935 (2020).

131. Comsol. *Optimization Module Application Library*. www.comsol.com/trademarks. (2021).

132. Narayanaswamy, A. *et al.* Young's modulus determination of normal and glaucomatous human Iris. *Invest Ophthalmol Vis Sci* **60**, 2690–2695 (2019).

133. Ferrara, M. *et al.* Biomechanical properties of retina and choroid: a comprehensive review of techniques and translational relevance. *Eye (Basingstoke)* vol. 35 1818–1832 Preprint at https://doi.org/10.1038/s41433-021-01437-w (2021).

134. Ye, S. *et al.* In vivo non-contact measurement of human iris elasticity by optical coherence elastography. *J Biophotonics* **14**, (2021).